Probing Large-Scale Structure with Radio Observations

A THESIS
SUBMITTED TO THE FACULTY OF THE GRADUATE SCHOOL
OF THE UNIVERSITY OF MINNESOTA
BY

Shea D. Brown

IN PARTIAL FULFILLMENT OF THE REQUIREMENTS
FOR THE DEGREE OF
Doctor Of Philosophy

June, 2009

Probing Large-Scale Structure with Radio Observations

by Shea D. Brown

ABSTRACT

This thesis focuses on detecting magnetized relativistic plasma in the intergalactic medium (IGM) of filamentary large-scale structure (LSS) by observing synchrotron emission emitted by structure formation shocks. Little is known about the IGM beyond the largest clusters of galaxies, and synchrotron emission holds enormous promise as a means of probing magnetic fields and relativistic particle populations in these low density regions.

I'll first report on observations taken at the Very Large Array and the Westerbork Synthesis Radio Telescope of the diffuse radio source 0809+39. I use these observations to demonstrate that 0809+39 is likely the first "radio relic" discovered that is not associated with a rich X-ray emitting cluster of galaxies.

I then demonstrate that an unconventional reprocessing of the NVSS polarization survey can reveal structures on scales from $15'$ to hundreds of degrees, far larger than the nominal shortest-baseline scale. This yields hundreds of new diffuse sources as well as the identification of a new nearby galactic loop.

These observations also highlight the major obstacle that diffuse galactic foreground emission poses for any search for large-scale, low surface-brightness extragalactic emission. I therefore explore the cross-correlation of diffuse radio emission with optical tracers of LSS as a means of statistically detecting the presence of magnetic fields in the low-density regions of the cosmic web. This initial study with the Bonn 1.4 GHz radio survey yields an upper limit of 0.2 μG for large-scale filament magnetic fields.

Finally, I report on new Green Bank Telescope and Westerbork Synthesis Radio Telescope observations of the famous Coma cluster of galaxies. Major findings include an extension to the Coma cluster radio relic source 1253+275 which makes its total extent $\sim$2 Mpc, as well as a sharp edge, or "front", on the Western side of the radio halo which shows a strong correlation with merger activity associated with an infalling

sub-cluster. This front is just interior to a temperature jump derived from XMM-Newton observations, and may be related to shocked infalling gas.

Acknowledgements

This thesis would not have been possible without the support of my family, friends and colleagues.

I'd first like to thank my advisor, Dr. Lawrence Rudnick, who constantly pushed me to be a better scientist. His wisdom helped me navigate the sometimes murky waters of scientific research, and I hope to continue to benefit from his guidance in the years to come. I would also like to thank my committee, Dr. Thomas Jones, Dr. Liliya Williams, and Dr. Yong-Zhong Qian, who provided both technical and scientific guidance on my thesis and research in general.

I'd like to thank my fellow graduate student Damon Farnsworth, for his much needed assistance on the cross-correlation work presented in Chapter 4.

My thanks to Professors Batuski, Comins, Roberts, and Wardle, who helped me get my start in the field of astrophysics, and inspired me to continue my education at the PhD level. I'd also like to thank Professor Donald Mountcastle, who taught me a good deal about thermodynamics, and even more about having a passion for science.

My thanks to Crystal Austin, Jessica Ennis, Andrew Helton, Martha Boyer, Kisha Delain, and all the other graduate students in the Department of Astronomy for showing me the ins-and-outs of graduate student life.

I owe the largest debt of gratitude to my wife Jovana and my daughter Siena, whose love and support saw me through all the chaos associated with getting a PhD. This thesis is dedicated to them.

Contents

Abstract i

Acknowledgements iii

List of Tables vii

List of Figures viii

1 Introduction 1

1.1 Background 1

1.2 Cluster Radio Emission 3

1.3 The WHIM 4

1.4 Radiative Theory 5

1.4.1 Shocks 5

1.4.2 Polarized emission 7

1.4.3 Faraday Rotation 7

1.5 The Chapters 9

2 Diffuse Cluster-Like Radio Emission in Poor Environments 11

2.1 Introduction 11

2.2 Observations & Data Reduction 12

2.2.1 Observations 12

2.2.2 Total Intensity Calibration 13

2.2.3 Polarization Calibration 13

2.3 Image Production & Analysis 14

2.3.1 Initial Spectral Cube . . . 14
2.3.2 Total Intensity . . . 14
2.3.3 Polarization . . . 15
2.4 X-ray & Optical Identification . . . 18
2.4.1 X-Ray . . . 19
2.4.2 Optical . . . 19
2.5 Physical Origin of the Radio Emission . . . 21
2.5.1 Northern Component . . . 22
2.5.2 Southern Component . . . 27
2.5.3 Implications . . . 28
2.6 Summary . . . 29

3 The Discovery of Diffuse Radio Polarization Structures in the NVSS 47
3.1 Introduction . . . 47
3.1.1 Polarization Image Preview . . . 49
3.2 Map Analysis . . . 51
3.3 Results . . . 54
3.3.1 Cygnus-Perseus region . . . 55
3.3.2 Galactic Center region . . . 55
3.3.3 The Extragalactic Sky . . . 57
3.3.4 Abell 3744 . . . 58
3.3.5 3C 31 . . . 59
3.3.6 CTA1 . . . 60
3.4 Discussion . . . 61
3.4.1 CMB polarized foregrounds . . . 62
3.5 Conclusions . . . 63

4 Cross-Correlation of Diffuse Synchrotron and Large-Scale Structures 79
4.1 Introduction . . . 79
4.2 Cross-Correlation . . . 81
4.2.1 Images . . . 81
4.2.2 Cross-Correlation . . . 82
4.2.3 Detection Thresholds . . . 83

4.3 Physical Expectations/Interpretations 83
4.4 Summary 85

5 Diffuse Radio Emission in/around the Coma Cluster: Beyond the Simple Accretion Scenario 90
5.1 Introduction 90
5.2 Observations & Data Reduction 92
5.3 Results 93
5.3.1 Extended Relic 93
5.3.2 Halo Profile 94
5.3.3 Other Diffuse Emission 94
5.4 Discussion 94
5.4.1 Relic 94
5.4.2 Halo 96
5.4.3 Global Radio vs. X-ray Correlation 97
5.5 Summary 99

6 Conclusion and Future Work 108
6.1 Key Messages 108
6.2 Future Work 109
6.2.1 Low Frequency Polarized Foregrounds 109
6.2.2 Detecting the WHIM with the SZE 110
6.2.3 ALFALFA & GALFACTS 111
6.2.4 ASKAP Telescope: POSSUM & EMU 112

References 113

List of Tables

2.1 *PROPERTIES OF THE DIFFUSE COMPONENTS OF 0809+39:* a: Errors taken from final maps σ_{rms} and does not include the uncertainty in the total intensity calibration; b: Typical local galactic value. 18
2.2 *DISTANCE DEPENDENT PROPERTIES OF 0809+39* 18
4.1 CROSS-CORRELATION DETECTION THRESHOLDS: a: Bracketed values are thresholds when adding filaments only (see text). b: The flux required per galaxy to reach the detection threshold. 84

List of Figures

1.1 Left: Smoothed distribution of galaxies from the 2MASS survey; Right: 326 MHz radio contours over X-ray brightness for the Coma cluster. . . 3

2.1 WSRT 351 MHz total intensity image with contour levels 8.254×10^{-3}(-0.4, 0.4, 0.5, 0.8, 1.2, 2, 3, 4, 6, 8, 16, 32, 64) Jy/($108''\times60''$ beam). S1 and S2 are "compact" sources at 351 MHz that show sub-structure at higher resolution (see Figure 2.2). 31

2.2 VLA I image (left) with contours 2.0×10^{-4}(-1, 1, 2, 3, 4, 5, 7, 9, 11, 13, 15) Jy/($40''\times40''$ beam). At right are close-ups views of S1 and S2 from the FIRST survey. Contours 4.0×10^{-4}(1.5, 2, 3, 4, 6, 8, 10, 20, 50, 100) Jy/($5''\times5''$ beam). 32

2.3 Spectral index map from 351 MHz to 1.4 GHz, with WSRT contours 8.25×10^{-3}(-0.5, 0.5, 0.8, 1, 2, 3, 6, 12, 24, 48) Jy/($108''\times60''$ beam). . . 33

2.4 Top: Our RMTF; Center: Faraday spectrum for N_{Diff}; Bottom: Faraday spectrum for a large area of the Galactic emission. Characteristic error bars are shown. 34

2.5 B field orientation obtained from derotating the NVSS to correct for a rotation measure of +12 rad m^{-2}. Contours are NVSS I at 4.9×10^{-3}(-0.3, 0.3, 0.4, 0.5, 0.8, 1.2, 2, 3, 4, 5, 6, 8, 16, 32, 64) Jy/($45''\times45''$ beam), and the magnetic field lines are $1''$=2.22×10^{-5} Jy/($45''\times45''$ beam). . . 35

2.6 WSRT 351 MHz contour image of 0809+39 I (same contours and resolution as Figure 2.1) with corrected magnetic field vectors for the RM-Cube at $\phi = +12\ rad\ m^{-2}$. $1'' = 1.85\times10^{-5}$ Jy/($108''\times60''$ beam). The apparent "noise" in the polarized emission is actually real emission from our own galaxy. 36

2.7 ROSAT broad (0.1-2.4 keV) continuum grayscale (convolved to 100″) with VLA L-band contours. To the right are ROSAT images of three X-ray selected clusters at the indicated redshifts, at the same grayscale and resolution as the 0809+39 ROSAT image. 37
2.8 Left: XMM Epic observation in counts (convolved to 20″) with VLA radio contours 6.5×10^{-3}(0.05, 0.1, 0.2, 0.4, 8) Jy/(49″×42″ beam). Note that a faint X-ray source is coincident with F2 (the WAT seen in Figure 2.2); Right: SDSS R image with XMM EPIC contours. Grayscale is in units of counts, and the contours are 4.08×(3.5, 4, 5, 6, 8) counts. X-ray source 2 is the WAT (F2) and the galaxy near source 3 is coincident with compact radio source F1. 38
2.9 SDSS R mosaic grayscale (in counts) with VLA 1.4 GHz contours at 2.0×10^{-4} (-1, 1, 2, 3) Jy/(40″×40″ beam). 39
2.10 Plot of known groups/clusters in the 0809+39 region. Boxes are z≈0.04 systems, triangles are z≈0.07 systems, and the cross is a z≈0.11 cluster. 40
2.11 Histograms of galaxy photometric redshifts from SDSS for 6′ around the WAT source F2 (Top, see Figure 2.2) and the X-ray selected clusters RXCJ1327.0+0211 (Center) and RXCJ2155.6+1231 (Bottom) (Popesso et al. 2004). Note that all the histograms have a narrow peak at z∼0.35. This is an artifact of the template fitting method for calculating the photometric redshifts (Csabai et al. 2003; see Figure 16 in that paper). . 41
2.12 Distribution of galaxies from the SDSS photometric database with redshifts between $0.15 < z < 0.25$, smoothed to 6′. Left: 0809+39; Using the same redshift limits we show two X-ray selected clusters for comparison: Middle: RXCJ1327.0+0211; Right: RXCJ2155.6+1231 42
2.13 Top: Distribution of $0.0366 < z < 0.0448$ galaxies with spectroscopic red-shifts in SDSS plotted as stars. Bottom: close-up view of the boxed region in the top panel. S_{Diff} is embedded in the filament of galaxies. . 43

2.14 Distribution of redshift vs. RA for galaxies with spectroscopic redshifts in SDSS in a roughly 4×4 degree field around 0809+39. The dashed lines enclose the range in z used to create Figure 2.13 ($0.0366 < z < 0.0448$), and show the clustering of the filament galaxies. There are other significant structures at higher redshifts, but the filament at z=0.04 was deemed significant based on its spatial correlation with S_{Diff}. 44

2.15 Plot of relic radio luminosity/Hz at 1.4 GHz vs. the 0.1-2.4 keV X-ray luminosity of the associated cluster. Compiled are 22 radio relics from Giovannini et al. (1991); Giovannini, Tordi, & Feretti (1999); Kempner & Sarazin (2001); Govoni et al. (2001); Slee et al. (2001); Govoni et al. (2005). They represent a complete list of radio relics that have reasonably reliable 1.4 GHz Flux density measurements. 45

2.16 1.4 GHz power vs. linear extent in kpc for a sample of WAT sources (Pinkney et al. 2000). S_{Diff}, if at redshift of z>0.5, is an extremely large radio galaxy. 46

3.1 All sky AITOFF projections in galactic coordinates of the NVSS, at a resolution of 800". The top image shows the total intensity, with polarized intensity on the bottom. The obvious striping in the polarized intensity, mostly along lines of declination, are due to variations in the residual instrumental polarization during the survey. Occasional small black regions is where the residual instrumental polarization was especially high, and the polarization data were flagged for that individual pointing. . . . 64

3.2 Total and polarized intensity around the Perseus-Cygnus region of the galactic plane. Galactic coordinates are indicated on the left image. "X" marks the position of the celestial pole; circles around the pole visible in the middle image show lines of constant declination. Left: 21 cm total intensity from Bonn 25m survey Reich & Reich (1986), 36' resolution. Center: Polarized intensity from NVSS at 800" resolution, with no filtering. Right: Filtered version of map on left, as described in text. The black circle marks the Cygnus arm at $l_{II}=90^o$; the arrow indicates the base of what is normally called "Loop III" and is discussed further in the text and in Figure 3.9. 65

3.3 Flow chart for construction of polarization images P_{800} and P_{800f}. . . . 66
3.4 Flow chart for construction of simulated images (signal+noise) for sensitivity experiments. The NVSS Q and U images were first clipped to remove the effects of strong, compact polarized sources. 67
3.5 Flow chart for two options of processing (Signal+Noise) images for sensitivity calculations. 68
3.6 Example of simulated polarization data used to calculate sensitivity. The central 1 square degree contains the simulated signal, a random pattern of polarized flux with a characteristic scale of 8'. In this particular example, the image was "pre-convolved" by 4' and "post-convolved" by 8'. 69
3.7 Left: Histograms of the rms noise in each 4^o field in the NVSS. Right: signal:noise from simulated polarization measurements, as described in the text. The black line indicates "pre-convolution" of the Q and U images; the grey (lower) line indicates "post-convolution" of the P image. 70
3.8 RMS scatter in P_{800} in strip from $53^o < b_{II} < 67^o$ as a function of galactic longitude. Inidividual spikes and the large scatter are due to variations in residual instrumental polarization. A region of low instrumental effects is indicated, along with the increased rms power due to the North Polar Spur. 71
3.9 DRAO Stokes Q image (Wolleben et al. , 2006) in celestial coordinates, centered at RA,, Dec. $\sim$ 15h, 30^o , and approximately $150\ ^o$ in RA by 110^o in Dec. "L" marks the base in the galactic plane of the suggested new loop, at l_{II}=82^o. while the arrow shows the position of the galactic center, just below the edge of the image, so the galactic plane runs between these two. X marks the galactic pole, and NPS denotes the North Polar Spur. A curved line is drawn outside of the possible new loop. 72
3.10 Left: Polarized intensity from DRAO survey (Wolleben et al. , 2006). Right: Polarized intensity from NVSS. Both images have a resolution of 36'. The field is centered at l,b = 26.5^o, -1.1^o and is 50 degrees in width. 73

3.11 Image of approximately $44^o \times 17^o$ strip in celestial coordinates, centered around 11.8h,34.2dm Red is P_{800f} , green shows the broadband X-ray emission from ROSAT, convolved to 800", and blue is the total intensity emission from NVSS, convolved to 800". 74
3.12 Abell 3744, contours and slice of NVSS polarized intensity at resolution of 800". The top image is overlaid by the NVSS total intensity at 45" resolution. Contour levels are at 0.01 × (4, 5, 6, 8, 10) Jy/beam. The total field is 95" in declination by 115" in right ascension. The slice is taken in right ascension through the peak and extends over 5^o to show the signal:noise of the detected features. 75
3.13 5.3^o field with 3C31 (upper left) and NGC 315 (lower right). P_{800f} is in red. The brightness of the southwest extension of 3C31, ignoring the region of the background double, is ∼12 mJy/800" beam. The vertical and horizontal lines indicate slight differences in background removal from the original 4^o NVSS fields. The green image is the full resolution WENSS survey image at 330 MHz. 76
3.14 Contours of polarized emission (P_{800f}) in a 2^o field around 3C31, at levels of (6, 13, 28, 38, 51, 76, 100, 126 and 140) mJy/800" beam. Small circles indicate the positions of galaxies at redshifts of 0.014 to 0.020 from the 2MASS survey (Huchra et al. , 2005). 77
3.15 CTA 1. Greyscale is P_{800f} , with a peak brightness of 45 mJy/800" beam. Contours are broadband X-rays from ROSAT, convolved to 800". The hatched circle represents the cloud described by Pineault et al. (1997), and the arrow indicates the new polarized patch not visible in the DRAO higher resolution image. 78
4.1 Center coordinates for each image are 16h00m00s +35d00m00s. Top-Left: Original $34^\circ \times 34^\circ$ 1.4 GHz, intensity Bonn image; Top-Right: Same field with Galactic gradients removed. The brighter point sources are 400-600 mK above the 3-3.5 K background in the unfiltered image. Bottom-Left: The distribution of galaxies from 2MASS with $0.03 < z < 0.04$, convolved to $36'$. Peak/mean=64; Bottom-Right: Same for $0.06 < z < 0.07$. Peak/mean=30. 86

4.2 CCF for the unfiltered and filtered 1.4 GHz total intensity Bonn images and the $0.03 < z < 0.04$/ $0.06 < z < 0.07$ 2MASS surface density of galaxies. The angular scale for each image is 11.3° on a side (total shift of 201 pixels), which is ∼19 independent beams across. The CCFs are normalized and values range from -0.2 (black) to 0.2 (white) for the unfiltered CCFs and -0.1 (black) to 0.1 (white) for the filtered. 87
4.3 Distribution of cross-correlation values for the Bonn images with the 2MASS galaxy distribution images. Red lines indicate the CC value of the target field centered on 16H35D. 88
4.4 Sparsely sampled CC functions. Red diamonds are the 2MASS images correlated with the 24 Bonn fields. The Green diamond is the target fields CC value, and the dashed line is the 3σ value of the distribution. . 89
5.1 Top: GBT total intensity image of the Coma cluster; $12' \times 12'$ resolution; Bottom: GBT total intensity contours with only constant DEC scans and NVSS point sources subtracted out ($14.25' \times 13'$ beam). Grayscale is ROSAT X-ray residual image after a beta-model has been subtracted. . 100
5.2 Top: WSRT total intensity image of the Coma Cluster. The image was made from a 4-pointing mosaic with a central frequency of 352 MHz (31 MHz bandwidth) and a resolution of $134' \times 68'$. Bottom: Same as above, but with point sources (UV data >700 λ) removed. The green circle indicates a region where the background radio source Coma A has left residual artifacts, and should be ignored. 101
5.3 Annular average of the point-source subtracted WSRT image showing the new "front" of synchrotron emission. The average was over a 90° wedge centered on 13h01m20s+27d57m. 102

5.4 Top: Plot of velocities in a 2deg high band through the Coma cluster and from 0.5 to 1.5 degrees from the Coma center, at an angle of 0.5 radians, which includes the infall cluster and the broader wall. shown is two component Gaussian fit to the velocity distribution. Infall: peak 27; center 7450 km/s; FWHM 700 km/s Residual: peak 30; center 7000 km/s; FWHM 2200 km/s; Bottom: Smoothed surface-density of optical galaxies from the SDSS spectroscopic database with $6600 < v < 8200$ (grayscale) with GBT contours from Fig 1. Note the "wall" of galaxies that ends on the inside edge of the radio relic. 103

5.5 Top: 1-D slice across the Coma halo and relic in radio and X-ray brightness; Bottom: Same slice except 1.0° wide through the optical surface density of SDSS galaxies in three velocity cuts. Note the drop in number of galaxies with $6600 < v < 8200$ as the relic radio emission increases. . 104

5.6 Grayscale is the point-source filtered "open" map (Fig. 2) with X-ray contours from Neumann et al. (2003). The contours are residual X-rays after a relaxed cluster beta-model has been subtracted out, and indicate regions of active infall. 105

5.7 Thermal X-ray temperature map (Wik et al. 2009) with diffuse radio contours overlaid. The color scale goes from purple/blue 1.5 keV to red/white 12 keV. Higher signal/noise fits were taken of the boxed regions (Alexis Finoguenov, private communication) which found $16.3^{+3.5}_{-2.3}$ keV on the right and $6.8^{+0.7}_{-0.5}$ keV on the left. 106

5.8 Data points are a pixel-to-pixel correlation between the diffuse radio surface-brightness at 352 MHz and the X-ray surface brightness from ROSAT. Also shown is the measured power-law correlation found by Govoni et al. 2001, as well as predicted correlations for primary and secondary models. 107

6.1 Image of the Galactic polarized foreground emission at a Faraday depth of zero in the region of the Coma cluster. The color bar is in units of Jy beam^{-1}, where the beam is $70' \times 70'$. 110

6.2 Left: continuum image from gridbf 2316+15c smoothed to 6′; Right: The same image with NVSS point sources partially subtracted out. There are many alignment and beam issues that still need to be addressed, and the systematic striping has not been taken out. 111

Chapter 1

Introduction

The broad goal of this dissertation is to use radio observations to probe the physical state and dynamics of relativistic and thermal plasma in large-scale structure (LSS). I will begin with a general background, introducing cosmology and the problem of detecting diffuse plasma in LSS with radio observations (§1.1). In §1.2 I will focus on the synchrotron features found in and around massive clusters of galaxies, namely radio relics and halos. Radio relics in particular, which are believed to be shocked gas infalling into massive clusters, serve as models for what we might expect to observe in the low-density regions of filaments of galaxies. I will then discuss the expected nature of the plasma within filaments in §1.3, called the Warm-Hot Intergalactic Medium (WHIM). Much of this dissertation focuses on detecting polarized shocks in LSS by observing synchrotron emission emitted by relativistic electrons. Therefore, I will describe in §1.4 possible ways in which the population of relativistic electrons is energized, focusing on relativistic shocks. I will also review the radiative physics including how the synchrotron emission is affected as it moves through the regions between the source and detector (Faraday rotation in particular).

1.1 Background

The field of cosmology is concerned with the origin, evolution, and fate of the universe as a whole. In the past decade a unified cosmological model has emerged where the universe was born in a powerful explosion 13.7 billion years ago. Shortly after this

explosion the universe, which was mostly ionized hydrogen, began to rapidly expand and cool. In this model, the wealth of structure that we see today, planets, stars, and galaxies condensed out of this cooling primordial gas.

This picture, however, is not yet complete. Galaxies are not distributed homogeneously throughout the universe, but reside in larger groupings collectively called "Large-Scale Structure" or the "Cosmic Web". Figure 1, which shows the distribution of galaxies in a region of the northern sky, illustrates three common features of the cosmic web; clusters, filaments, and voids. A forefront of cosmological research is to understand how these structures form, and what effect the formation process has on the galaxies that make them up. A fundamental feature of the current model of structure formation is that it is hierarchical; smaller structures merge to form larger structures. This process is governed mainly by the gravitational interaction of dark matter, the mysterious invisible substance that makes up most of the total mass in our universe. This means that the largest structures that we can see today, massive clusters of galaxies, are continuously accreting dark matter (along filaments that connect them). It is not the interaction with accreting dark matter, however, that has the largest impact on visible galaxies, but with the plasma that is accreted along with it.

The first evidence for the presence of plasma between the visible galaxies came from the cores of massive clusters where the temperatures and densities become so high that the plasma emits X-rays. Interaction with this ionized gas effects the physical properties of the galaxies within the cluster, such as the size of their disks and the speed in which they make new stars. Unfortunately, in galaxy filaments where the plasma-galaxy interaction is predicted to be quite strong, the temperatures and densities are too low to make X-ray observations useful. Because of this astronomers know very little about the properties, or even the existence, of plasma in these environments. A large part of my research focuses on using radio observations to probe the (thus far invisible) low density plasma of galaxy filaments, where the complicated and important process of accreting gas and dark matter is taking place.

Radio observations are uniquely suited to study the ionized gas within large-scale structure. The accretion of gas onto the filaments and clusters often happens faster than the local speed of sound. This will cause powerful shocks which accelerate protons and electron to relativistic energies. In the presence of magnetic fields, the electrons

(and protons to a much lesser degree) will emit synchrotron radiation, which is a unique signature of both relativistic electrons and magnetic fields. Therefore, simply the detection of synchrotron radiation within filaments would give us a handle on two important properties of the plasma that effects galaxy evolution.

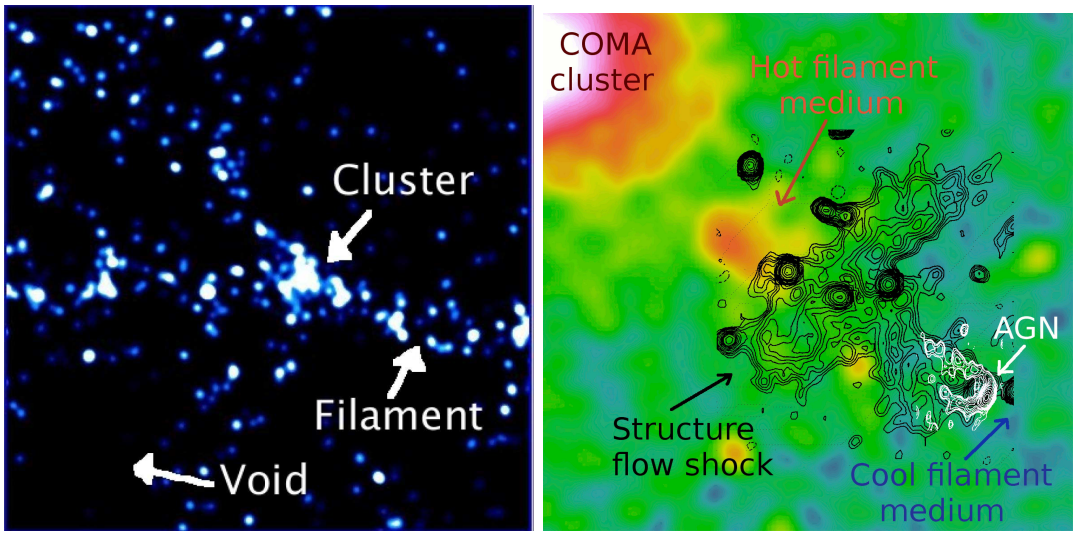

Figure 1.1: Left: Smoothed distribution of galaxies from the 2MASS survey; Right: 326 MHz radio contours over X-ray brightness for the Coma cluster.

1.2 Cluster Radio Emission

Groups and Clusters of galaxies reside in the deep potential wells formed by the clustering of dark matter. Due to the deepness of this potential well, the intracluster medium (ICM) is full of hot gas (T$\sim 10^8$ K) and relativistic particles unable to escape (e.g. Sarazin, 1999). The diffuse radio emission in clusters can be separated into two broad groups, radio halos and radio relics. Radio halos consist of diffuse emission found toward the central region of the cluster, and are in general not found to be polarized (see Govoni et al. 2004 for a notable exception). Radio relics occur on the periphery of clusters, and are suspected to be the results of large-scale structure formation (e.g. Enβlin et al. 1998). In contrast to radio halos, relics often show strong linear polarization. The

presence of non-thermal radio emission leads to the conclusion that the ICM and its periphery contains magnetic fields on the order of B $< \mu$G (e.g., Carilli & Taylor 2002, Feretti & Giovannini 1996, Govoni et al. 2001, Bacchi et al. 2003). Fig. 1.1 illustrates this paradigm with the Coma cluster of galaxies (see Chapter 5). The color is X-ray emission and the contours are radio observations (for the relic only). As cool gas flows along the filament, which runs from the bottom right to the Coma cluster, it passes through a shock which accelerates electrons and heats the plasma, emitting synchrotron radiation in the process. This dissertation is focused on detecting radio emission in the cooler filament medium (the WHIM), where little is known about the gas dynamics.

1.3 The WHIM

In the current cosmological paradigm, ≈95% of the mass/energy density of the universe is composed of dark energy and dark matter, both of which have yet to be directly detected. The remaining 5% are ordinary baryons, which at redshifts of z > 2 are fully accounted for based on Lyα forest observations of the photoionised intergalactic medium (IGM) and ordinary galaxies (e.g. Rauche et al. 1997; Weinberg et al. 1997; Schaye 2001). In the current epoch though, roughly half of these baryons are missing. Simulations suggest that the collapsing diffuse IGM was shock-heated and now resides in filaments as T$\sim 10^5$ - 10^7 K WHIM, where it is practically invisible at most wavelengths (Cen & Ostriker 1999, 2006; Davé et al. 2001). A few tentative absorption detections of the coolest WHIM components using OVII and OVIII have been reported, but they give no information on the spatial distribution. However, shocks from infall into and along the filamentary structures between clusters are now widely expected to generate relativistic plasmas which track the distribution of the WHIM (Keshet et al. 2004; Pfrommer et al. 2006; Ryu et al. 2008; Skillman et al. 2008); indeed, accretion shocks are seen as polarized radio sources (the "peripheral relics") at the edges of the dense X-ray gas in clusters. This radio emission also has the potential for probing into the lower density regions further from cluster cores. When such features are detected, they can be used to set limits on the (invisible) pressure of the thermal gas, delineate shock structures, and illuminate large scale magnetic fields.

1.4 Radiative Theory

Let us now examine the emission of synchrotron radiation from shocked plasma containing relativistic electrons and a magnetic field. I will in no way attempt a complete review, but will only highlight pertinent effects that illustrate the general method of extracting source parameters from the data.

1.4.1 Shocks

As I will describe below, the lifetimes of relativistic electrons are such that radio relics and halos can't simply be the "leftover" emission from radio galaxies after they have been turned off. What I mean here is that a radio relic can't be the lobe of an old radio jet that has drifted, undisturbed, to the cluster's edge. Similarly, halos are not simply old radio lobes that have yet to leave the center of a cluster's potential well. Whether the electrons are ordinary ICM electrons or true relic electrons from past AGN, there must be some mechanism for injecting energy into the particle population to observe the sources where we do. The method I will discuss here is first-order Fermi acceleration in shock waves, created during cluster mergers or the infall of material from cosmic filaments onto the boundaries of clusters (Quilis et al., 1998; Enβlin et al. 1998; Miniati et al., 2000). Let us parameterize a shockwave by a simple jump in the density from one side to the other, i.e., define $x \equiv \rho_2/\rho_1$. From Blandford & Eichler (1987), we see that the shock wave should generate electrons with an energy spectrum $dN/d\gamma = N_o\gamma^{-p}$, with p given by

$$p = \frac{x+2}{x-1}, \tag{1.1}$$

and γ is the Lorentz factor of the electrons. This is connected to the observed synchrotron intensity spectrum $I_\nu \propto \nu^{-\alpha}$ by $\alpha = (p-1)/2$ (Rybicki & Lightman 1979). This shock acceleration mechanism, however, is often not enough to explain some of the large emission regions seen (e.g., Markevitch et al. 2005, Govoni et al. 2004, Bruetti 2003). Basically, the inverse Compton (IC) and synchrotron losses cause the spectrum to steepen very quickly, so the electron lifetimes combined with the speed of the shock wave gives an estimate for the size of the emitting region. From Sarazin (1999), the electron lifetimes are given by

$$t_{IC} = 2.3 \times 10^{12} \gamma^{-1} (1+z)^{-4} \, yr \tag{1.2}$$

and

$$t_{syn} = 2.4 \times 10^{13} \gamma^{-1} B^{-2} yr, \tag{1.3}$$

where B is in μGauss and z is the redshift. The 1+z factor in the IC term reflects the fact that the energy density of the CMB photons goes as $u_\gamma \propto (1+z)^{-4}$. Pre-shock and post-shock gas velocities, as seen in the frame of the shock, can be calculated from the temperature jump and the Mach number. Values of the flow speeds are widely varying, but are on the order of $v \sim 10^2 - 10^3 kms^{-1}$ (e.g. Kang & Jones 2004). For a prominent bow shock in the galaxy cluster A520, Markevitch et al. (2005) computed that electrons generating the 1.4 GHz emission would only stream 100 kpc away from the shock front, an order of magnitude less than what was seen. Note that they assumed a $B \sim 1 \mu Gauss$.

Despite the fact that this mechanism alone often fails to explain many radio relics, we have not yet included several possible effects. The magnetic field energy density also increases in shocked regions, and we must include the possibility that the population of electrons is fossil radio plasma from an AGN (e.g. Enβlin & Gopal-Krishna, 2000). For a relic population with a spectral distribution of $dN/d\gamma = N_o \gamma^{-\delta}$, the increase in the normalization of the spectrum from magnetic field compression is

$$N_o \rightarrow N_o x^{(\delta+2)/3}, \tag{1.4}$$

and the increase due to re-acceleration of the fossil electrons is

$$N_o \rightarrow N_o \frac{3x}{x + 2 - \delta\,(x-1)}. \tag{1.5}$$

Note that I have left out many of the details, and that the re-acceleration equation works only for a $\delta < p$ (Blandford & Eichler 1987; Micono et al. 1999). Whether these two effects are additive probably depends on the details of the processes at the microscopic level (Markevitch et al. 2005), but the boost would allow the population to radiate at a given frequency longer as it streams away from the shock front.

1.4.2 Polarized emission

Let us now examine the effect a shock may have on the polarization of the synchrotron emission. Laing (1980) found that the degree of linear polarization, i.e. the fractional polarization, was increased in a compressed gas with a totally tangled magnetic field. This increase is greatest when the compression is viewed edge on. We can draw an analogy from a plate full of spaghetti; when viewed from the top, the spaghetti appears completely tangled, but when viewed from the side, it appears well ordered in horizontal stripes (from personal correspondences with John Wardle). It is this apparent ordering of the field that gives rise to the increased fractional polarization. The exact details of this effect depend on the geometry and the amount of order present in the field before the compression. To illustrate, let us examine the case for a simple slab geometry where the spectral index is $\alpha = 1$ and the field is totally tangled. The ratio of the fractional polarization p to the maximum polarization $p_{max} = (3\alpha + 3) / (3\alpha + 5)$, which is the intrinsic degree of polarization for a region of uniform field (Le Roux 1961, Pacholczyk 1970), is given by

$$p/p_{max} = cos^2\beta \left(1 + sin^2\beta\right) \tag{1.6}$$

Here, β is the angle of the plane of the shock to the line of sight. Clearly the fractional polarization reaches a maximum for $\beta = 0$. It should be noted that detection of polarized emission in these radio halos and relics does not mean that the gas is necessarily shocked. In fact, Govoni et al. (2004) detected filamentary polarized emission in the cluster A2255, and attributed it to large-scale magnetic field ordering that was not shock related. Even when a source has been clearly identified as a shock, observation of the polarized flux is confounded by internal Faraday rotation and beam depolarization (see the next section for details).

1.4.3 Faraday Rotation

Once the polarized radiation is produced, it encounters many obstacles on its journey to our telescope. Within the ICM itself, the light must travel through plasma that may contain magnetic fields. If we consider a magnetic field that is much stronger than the field of the propagating wave, the dielectric constant, which is different for left and right

handed polarizations, is given by (Rybicki & Lightman 1979)

$$\epsilon_{R,L} = 1 - \frac{\omega_p^2}{\omega\left(\omega \pm \omega_p\right)}. \tag{1.7}$$

Here, $\omega_p^2 \equiv 4\pi n e^2/m$ defines the plasma frequency, and $\omega_B \equiv eB_o/mc$ is the cyclotron frequency. The effect of this anisotropic dielectric constant is to rotate the position angle of linearly polarized waves, known as Faraday rotation. The amount of rotation is a function of wavelength, and is given by

$$\Delta\chi = \frac{2\pi e^3}{m^2c^2\omega^2}\int_{there}^{here} n_e B_\parallel ds. \tag{1.8}$$

The Faraday depth of a source can be defined as the above relation without the wavelength dependence (see, e.g., Burn 1966; Brentjens & de Bruyn 2005). Numerically it is expressed as

$$\phi(r) = 0.81\int_{there}^{here} n_e B_\parallel ds, \tag{1.9}$$

where n_e is the electron density in cm^{-3}, B is in μGauss and the path-length ds is in parsecs. Experimentally, what we measure is the slope of the position angle as a function of λ^2, known as the rotation measure (RM), which is equal to the Faraday depth only if there is a single source along the line of sight, no internal Faraday rotation, and insignificant beam depolarization (Brentjens & de Bruyn 2005). In which case,

$$\chi = \chi_o + \phi\lambda^2, \tag{1.10}$$

where χ and χ_o are the received and emitted polarization angles respectively. For a simple case such as this, measurement of the RM yields an equation for the magnetic field strength along the line of sight if the electron density is known.

Now that we have covered some basic physics of polarized emission, let us turn our attention to several effects that make polarization measurements difficult. Due to the fact that radio telescopes have finite resolution, there is a possibility that several sources with different polarization fall within the beam width. This leads to partial cancellation of the polarization, an effect know as beam depolarization. Another effect arises from Faraday rotation within the source. Basically, polarized emission from the back of the

source will Faraday rotate and interfere with the polarized emission emitted within the source along the line of sight (De Young 2002). Another problem lays in the ambiguity when plotting the position angle χ at different frequencies; you can freely add $n\pi$ to a given χ, where n is an integer, and still match the data. Recent authors have published novel attempts to overcome these problems.

Brentjens & de Bruyn (2005) presented a new technique to eliminate the confounding effects of intervening Faraday rotation by searching "rotation measure space" for polarized emission. In a way similar to aperture synthesis, they make use of discrete Fourier transformation properties of the rotation measure transfer function (RMTF) to solve for the polarized flux. This method has been successfully used to detect very diffuse polarized emission in the Perseus cluster (de Bruyn & Brentjens 2005), and could help characterize the low-density regions like cosmic sheets and filaments.

I have attempted to outline how synchrotron emission and its transport through astrophysical plasmas can be used as a tool for probing the ICM and cluster peripheries. The formalism I have discussed here is illustrative of the insights radio observations can give us into the physical processes taking place within filamentary large-scale structure.

1.5 The Chapters

The following chapters represent 4 attempts to probe the low-density, filamentary LSS with radio observations. In chapter 2, we present the detection and characterization of the *first* cosmological shock structure unassociated with a rich X-ray emitting cluster of galaxies. This shock or "relic" is connected to the dynamics of a low-density group of galaxies, and may be at the bright end of a much larger, unexplored population of sources. Chapter 3 outlines a new technique for using the polarized emission in the NVSS survey to detect large-scale synchrotron emitting regions such as cosmological shocks, as well as features in our own Galaxy. We were able to reveal complex structures spanning hundreds of degrees which remained invisible in total intensity, including a new Galacic loop. In chapter 4 we explore the promise of using cross-correlation to reveal filamentary synchrotron emission that is fainter than the noise level of the radio image. This statistical approach may be a necessity on angular scales where Galactic confusion dominates the radio sky. Finally, in chapter 5 we use deep 352 MHz

and 1.4 GHz observations of the well studied Coma cluster to reveal new synchrotron structures associated with infall onto the cluster. These structures occur in the low-density outskirts of the cluster, and represent the next level of sensitivity as we push the observational frontier into the unknown WHIM regions.

Chapter 2

Diffuse Cluster-Like Radio Emission in Poor Environments

A slightly modified version of the chapter appears in The Astronomical Journal: Brown, S., & Rudnick, L. 2009, AJ, 137, 3158

2.1 Introduction

In recent years, large-scale diffuse radio sources have been discovered to be associated with the intracluster medium (ICM) of over 50 clusters of galaxies. These features are unique probes of the non-thermal particle populations and magnetic fields within the cluster, and are believed to be important tracers of merger/formation dynamics. The majority of these sources were found by searching the environs of rich galaxy clusters for diffuse radio emission unassociated with active AGN (Giovannini et al., 1999; Kempner et al. , 2004). But is there also a magnetized, relativistic plasma associated with lower density regions of the cosmic web, such as groups and filaments of galaxies? Cosmological simulations predict complicated networks of accretion/merger shocks in these low density regions, which could accelerate particles, compress magnetic fields, and illuminate magnetized plasma if it exists (e.g., Miniati et al. , 2001; Ryu et al., 2003; Pfrommer, Enßlin & Springel , 2008). Unbiased searches for synchrotron signatures of these shocks are needed to confirm these predictions.

One such diffuse source, of ambiguous origin, is 0809+39 (Delain & Rudnick, 2006),

discovered through a blind search for diffuse radio emission in the WENSS survey (Rudnick, Delain & Lemmerman , 2006). The system showed no obvious associations with an active radio galaxy. Several poor clusters were found in the vicinity, which suggests a similar origin to radio relic and halo sources. However, lacking any evidence for cluster X-ray emission, its radio luminosity far exceeded the standard radio/x-ray ratios for these classes of sources (e.g., Giovannini & Feretti, 2004; Rudnick & Lemmerman , 2008).

We present a systematic study of the spectral, polarimetric, morphological and environmental properties of 0809+39 using observations taken with the Westerbork Synthesis Radio Telescope (WSRT) and the Very Large Array (VLA). We explore the origin of the diffuse radio emission and evaluate where 0809+39 falls in the parameter space of known extragalactic radio sources. We discuss observations and data reduction in §2, and in §3 we outline image production and analysis, including our application of Rotation Measure Synthesis (Brentjens & de Bruyn, 2005). In §4 we present archival optical and x-ray data, and in §5 we discuss the implications of our findings, followed by a summary of our key messages.

For calculations in this paper, we assume $H_o = 70$, $\Omega_\Lambda = 0.7$, $\Omega_M = 0.3$. We define the optically thin synchrotron spectrum as $F_\nu \propto \nu^\alpha$ throughout.

2.2 Observations & Data Reduction

2.2.1 Observations

The diffuse source 0809+39 was observed for 13 hours over two nights in P-band (350 MHz) with the Westerbork Synthesis Radio Telescope (WSRT) in January of 2006. The array was in the maxi-short configuration with the shortest baseline being 36 m. One primary flux and one polarized calibrator (as a pair) were observed at the beginning and end of each night. For the primary flux calibrators we observed 3C147 and 3C295, and for the polarized calibrators we observed DA240 and 3C303. We used the WSRT wide band correlator to cover a frequency range from 310-390 MHz with eight 10 MHz wide bands, each with 64 channels and full Stokes parameters. We applied a Hanning taper to the spectral data, and every other channel was selected for analysis yielding an effective spectral resolution of about 0.31 MHz. After removing the end channels in

each band and editing for strong RFI, 197 channels remained in the final analysis, for a total bandwidth of 61 MHz.

The VLA observations were taken for 2.8 hours in December of 2005 in the D configuration, and the flux calibrators 3C48 and 3C286 were used. The data were taken using the spectrometer with no cross-had polarizations. We analyzed only the pseudo-continuum data for this analysis, with a frequency of 1.4649 GHz, a bandwidth of 12.5 MHz, and no polarization information.

2.2.2 Total Intensity Calibration

The calibration and reduction of the WSRT and VLA data was performed using the NRAO's Astronomical Image Processing System (AIPS). For the WSRT data, the total intensity in each of the 8 bands was calibrated independently using standard procedures and the fluxes in the VLA calibrator manual for 3C147 and 3C295. The VLA pseudo-continuum data set was calibrated using standard procedures. We did several iterations of amplitude and phase self-calibration on each data set.

2.2.3 Polarization Calibration

Due to the fact that WSRT observes with orthogonal linear feeds (X and Y), the polarization calibration in classic AIPS involved several non-standard steps. WSRT polarization leakage terms are highly frequency dependent, so after the total intensity calibration, each channel was split into an independent uv-data set and the leakage terms were then solved for using the AIPS task LPCAL. Stokes Q values were calculated from (YY-XX)/2, while the Stokes U values are -(XY+YX)/2. An additional correction is needed for Stokes U, to remove the instrumental phase offset between the X and Y receivers using the polarized calibrators. Faraday rotation causes the Stokes Q and U amplitudes of the polarized calibrators to oscillate across the band. The X-Y phase offset was found for each channel by forcing the vector averaged Stokes $U = U\left(\lambda^2\right)$ visibilities for the polarized calibrators to match (offset by a quarter wavelength) the $Q\left(\lambda^2\right)$ sine wave formed by Faraday rotation. The observed sign of the Faraday rotation for 3C303 (+13 rad m^{-2}, Kronberg et al. 1977) forced Stokes U values to be a quarter wavelength *after* the Stokes Q values with increasing wavelength, breaking the

final sign ambiguity and finishing the polarization calibration. However, we note that the intrinsic position angle of the polarization is still highly uncertain due to errors in the rotation measure, as discussed in §3.3.

2.3 Image Production & Analysis

2.3.1 Initial Spectral Cube

After calibration, we created I, Q, and U images for each of the 197 WSRT channels. All images and self-calibrations were done in AIPS with the tasks IMAGR and CALIB respectively. Each channel image was cleaned with IMAGR with 70,000 clean components and a gain of 0.1. The synthesized beam varied from $89'' \times 52''$ to $108'' \times 60''$ across the band, so all of the images were uv-tapered and restored to a common resolution of $108'' \times 60''$. Typical rms noise levels for the single-channel {I,Q,U} maps were {1.0,0.5,0.5} mJy/beam, respectively.

2.3.2 Total Intensity

WSRT I-Map

The final WSRT I map is shown in Figure 2.1. This map is the simple average of all the individual channel I maps ($108'' \times 60''$ beam). The average frequency is 351 MHz and the observed noise is $\sigma \sim 188$ μJy/beam. The diffuse emission is seen to have two distinct components which we have labeled N_{Diff} and S_{Diff}. At this resolution, N_{Diff} partially blends into the compact sources S_1 and S_2. As shown in §3.2.2, some of these "compact" sources also have substructure. Flux and size properties for both diffuse sources are summarized in Table 2.1. We describe all the discrete radio sources in the next subsection.

VLA I-Map

Figure 2.2 shows our VLA I map, which has a noise level of 90 μJy/beam and a $40'' \times 40''$ restoring beam. We have labeled the discrete radio sources, and have shown VLA FIRST (Becker et al., 1995) images of some of the more interesting ones. The sources F1-F7 are adjacent to or embedded in the diffuse emission. F2 is a 66 mJy wide-angle tailed

(WAT: Owen & Rudnick 1977) radio galaxy at z=0.196 (from SDSS:[1] York et al. 2000; Stoughton et al. 2002), and F3 and F5 are identified with SDSS galaxies with photometric redshifts of z=0.249 and z=0.255, respectively. In S_{Diff}, the source F6 is marginally detected in FIRST (not shown), and is coincident with a z=0.04 galaxy in SDSS. F7 is a FIRST radio point source (not shown) with no optical identification in SDSS. The apparent bridge of emission between N_{Diff} and S_1 peaks on a spiral galaxy at z=0.041 (see Figure 2.9) and is most likely diffuse disk emission from that galaxy.

Spectral Index

For the spectral analysis we matched the uv-range of the VLA and WSRT data before comparison. The spectral index (α) map (Figure 2.3) was created in AIPS using the task COMB. Any pixel that was not at least 10σ above the noise in either map was blanked. Both sources are steep spectrum, and Table 2.1 lists the integrated α obtained from fitting the total flux of each component at 1.4 GHz and 351 MHz to a power law.

2.3.3 Polarization

Rotation Measure Synthesis

With the 197 channels and $\sim$ 61 MHz total bandwidth of our WSRT P-band data, it is possible to simultaneously determine the rotation measure distribution within each beam and remove the effects of bandwidth depolarization. When searching for polarized synchrotron emission, which is often at very low surface brightness levels, one would like to observe over a large bandwidth ($\Delta\nu$) to maximize the signal/noise ratio. However, this normally results in depolarization from the vectoral cancellation of the Stokes Q and U signals that have been Faraday rotated from one side of the band to the other. Some radio telescopes allow for a large observing bandwidth to be split into many narrow channels (Westerbork being one of them), so an obvious solution would be to make an image of the polarized amplitude in each channel and average them together. Unfortunately, polarized galactic foreground emission is ubiquitous (e.g., Reich 2006). This is actually above the surface brightness of some diffuse extragalactic regions of interest, so adding the scalar polarization intensity of each channel will cause the galactic

[1] http://www.sdss.org/

emission to add coherently as well. This increases the background and drowns out the desired diffuse extragalactic source.

Brentjens & de Bruyn (2005) presented a new technique to eliminate the confounding effects of intervening Faraday rotation (bandwidth depolarization and galactic foreground contamination) by searching "rotation measure space" for polarized emission. The technique proceeds as follows: assume a rotation measure for the source, then derotate the polarization vector in each individual channel (to a reference wavelength λ_o) to correct for this and make a polarization map from the average of the derotated channels. If the source in fact had the assumed rotation measure, the channels would add coherently, allowing for the full sensitivity of the entire bandwidth. The resulting map at a given Faraday depth, ϕ, is approximately given by

$$F(\phi) = \frac{1}{N} \sum_{j=1}^{N} P_j e^{-2i\phi\left(\lambda_j^2 - \lambda_o^2\right)} \tag{2.1}$$

where N is the number of maps (channels) used and $P_j = Q_j + iU_j$ is the complex polarization at channel j. The units of $F(\phi)$ are Jy/beam/rmtf, where rmtf stand for the Rotation Measure Transfer Function. The RMTF is the response of a source with emission at a single Faraday depth. If one were able to sample an infinite range of λ^2, the RMTF would be a delta function in RM space, but incomplete sampling induces side-lobe structures in a manner similar to side-lobes in the beam pattern of an interferometer due to incomplete sampling of the uv-plane.

The key step is to apply Eq. (1) for a wide range of rotation measures, creating a rotation measure cube (RM-Cube), and search for coherent structures within this cube. We processed the 197 Q and U maps in IDL utilizing Eq. (1) to create the final RM-Cube, with Faraday depths running from -200 rad m^{-2} to +200 rad m^{-2} in steps of 1 rad m^{-2}. This method has been successfully used to detect very diffuse polarized emission in the region of the Perseus cluster (de Bruyn & Brentjens, 2005).

Near values of $\phi = 0$, polarized emission from our own galaxy fills the field of view. This emission has a typical surface brightness of $\sim$1 mJy/beam/rtmf, and in the vicinity of 0809+39 it peaks at ϕ_{Gal} $\sim$+6 rad m^{-2}. The polarized emission in N_{Diff} peaks near +12 rad m^{-2}, though there is still a significant amount of galactic emission present at this Faraday depth. At values of $|\phi| > 30$ rad m^{-2}, very little of the galactic emission

remains. As a result, the rms noise of the images decreases with increasing $|\phi|$, to $\sim$30 μJy/beam/rmtf for $|\phi|$ >100 rad m^{-2}.

Some of the emission that de Bruyn & Brentjens (2005) detected in the field of the Perseus cluster with RM-Synthesis was later found to likely be Galactic in origin (Brentjens, 2007). In the case of 0809+39, N_{Diff}, while not segregated significantly from the Galactic emission in Faraday depth, is an order of magnitude stronger in surface brightness, making a Galactic origin unlikely.

We can also use this RM-Cube to find Faraday spectra, which is just $F(\phi)$ from Equation 1 for a single pixel or region in the sky. Figure 2.4 shows the average spectrum of a $1.8' \times 1.8'$ region centered on N_{Diff}, along with the RMTF for our frequency sampling. The Faraday spectrum of N_{Diff} is very close to a "point source" in Faraday space, especially when compared to a typical Galactic spectrum also shown in Figure 2.4. The diffuse galactic radiation along the line of sight to 0809+39 has emission at multiple Faraday depths. This galactic signal must also be present in our spectrum of N_{Diff}, but is lower than the side-lobe level of N_{Diff} itself.

Position Angle

We used the NRAO VLA Sky Survey (NVSS: Condon et al. 1998) polarization image of 0809+39, along with our measured RM, to find the absolute position angle χ of N_{Diff}. Figure 2.5 shows NVSS total intensity contours and magnetic field orientation (which is $\chi \pm 90^o$), corrected for the average ϕ of N_{Diff}. Due to the difference in resolution between the RM-Cube and the NVSS, and the fact that the gradient in ϕ across the source translates into only a $\delta\chi \sim 7^o$, we did not do a pixel-by-pixel de-rotation. The magnetic field runs along the long axis of N_{Diff}, and shows evidence of following the curvature in the southern end.

Our Faraday corrected WSRT magnetic field vectors are plotted in Figure 2.6. We obtained the polarization from the complex RM-Cube at $\phi = +12$ rad m^{-2}, where N_{Diff} peaks. Given the uncertainties in absolute position angle when derotating from λ=90 cm to λ=0 (e.g., $\sigma_\chi \approx 140^o$ when $\sigma_\phi = 3$ rad m^{-2}), we globally rotated the vectors so that the magnetic field orientation of N_{Diff} matches that seen in Figure 2.5. We placed the polarized intensity cut-off such that some of the diffuse Galactic emission can be seen. One can see the discontinuity in angle between the galactic polarization

and the brighter N_{Diff} emission.

Fractional Polarization

The detection of N_{Diff} in the NVSS survey allows for examination of the degree of de-polarization. The fractional polarization, m, decreases from $m \sim 45-55\%$ at 21cm (matched to the WSRT resolution) to $m \sim 20\%$ at 92 cm. Assuming for a moment that this depolarization is due only to internal Faraday de-polarization (Burn, 1966; Cioffi & Jones, 1980), we calculate the necessary internal Faraday rotation to be $\phi_{in} \approx 2$ rad m^{-2}. The upper limit intrinsic width of N_{Diff} is $\approx 7-9$ rad m^{-2}, so the depolarization could be due to internal Faraday de-polarization. At 351 MHz, S_{Diff} is not polarized at a 3σ level of 9%.

Source	P-band flux[a] (mJy)	L-band flux[a] (mJy)	FWHM Size $''$	Frac. Pol. % (351 MHz)	Mean α	ϕ *rad m*$^{-2}$
N_{Diff}	178±0.7	37.8±0.7	200	19	-1.12	+12
S_{Diff}	136±1.1	24.8±1.0	490	< 9 (3σ)	-1.23	$\sim +6$[b]

Table 2.1: *PROPERTIES OF THE DIFFUSE COMPONENTS OF 0809+39:* a: Errors taken from final maps σ_{rms} and does not include the uncertainty in the total intensity calibration; b: Typical local galactic value.

Region	z	$P_{0.32}$ 10^{23} W Hz^{-1}	$P_{1.4}$ 10^{23} W Hz^{-1}	L_X (0.1-2.4 keV) log(erg s^{-1})	Physical Size Mpc	B_{min} μG
N_{Diff}	0.20	205	43.4	<43.0 (3σ)	0.66	0.64
S_{Diff}	0.04	5.07	0.99	<41.5 (3σ)	0.39	0.57

Table 2.2: *DISTANCE DEPENDENT PROPERTIES OF 0809+39*

2.4 X-ray & Optical Identification

We now turn our attention to the optical and X-ray environment of 0809+39. Since all radio halo and relic sources found thus far exist in or adjacent to the hot gas of galaxy

clusters, we searched for thermal emission from X-ray clusters in the vicinity of 0809+39 and investigated the surrounding optical field.

2.4.1 X-Ray

Figure 2.7 shows the ROSAT broad (0.1-2.4 keV) continuum emission in the region of 0809+39 with VLA L-band radio contours overlayed. To put the low observed brightness of the X-ray field of 0809+39 in context, we have also plotted three X-ray selected clusters at three different redshifts. The clusters are {RXCJ2324.3+1439, RXCJ1353.0+0509, RXCJ2155.6+1231} with redshifts of {0.042, 0.079, 0.192 } and X-ray luminosities of L_X={0.97, 1.97, 5.51}$\times 10^{44}$ h_{70}^{-2} erg s^{-1}, respectively (Popesso et al., 2004). The cluster redshifts were selected to mimic the relevant systems we have identified in §4.2. It is clear that no diffuse X-ray emission like that present in the X-ray selected clusters is present in the ROSAT 0809+39 field.

Figure 2.8 shows VLA contours over XMM EPIC grayscale as well as XMM contours over SDSS R grayscale from an XMM observation of the nearby galaxy UGC 4229 (P.I. Matteo Guainazzi) where 0809+39 was toward the edge of the field. There is clear emission from the WAT, but there are also several peaks in the region of N_{Diff}. Peak 2 is located on the WAT. Peak 1 is coincident with an SDSS photometric object at $z = 0.313 \pm 0.1$, and peak 4 is coincident with an SDSS photometric object at $z = 0.272 \pm 0.06$. Peak 3 is offset $\sim 10''$ from a 2MASS galaxy at $z = 0.02$, which is also the FIRST source F1 in Figure 2.2.

After subtracting out the four point sources, we found no evidence of excess diffuse emission. Using webPIMMS[2] we calculate a 3σ upper limit X-ray luminosity of L_X(0.1-2.4 keV)=1×10^{43} erg s^{-1} at an assumed redshift of z=0.2.

2.4.2 Optical

As one would expect from a region that spans more than $400''$ on the sky, the optical field of 0809+39 contains multiple, overlapping redshift systems. This is illustrated by Figure 2.9, which shows an SDSS mosaic R image with VLA contours. To set the scale, the large spiral galaxies in this image are at a redshift of roughly z = 0.04. We begin

[2] http://heasarc.nasa.gov/Tools/w3pimms.html

by outlining the known and cataloged optical systems in this region, then focus our attention on the systems we believe are most likely associated with N_{Diff} and S_{Diff}.

Delain & Rudnick (2006) suggested an association of both N_{Diff} and S_{Diff} with a grouping of galaxies at z$\sim$0.04. A $z = 0.04063$ group (16 members) is reported by Miller et al. (2005) from the SDSS cluster catalog C4, and Merchán & Zandivarez (2005) find a group at z=0.040346 (19 members) from DR3. Gal et al. (2003) also detected z$\sim$0.073 and z$\sim$0.11 clusters in this region. These are plotted in Figure 2.10. From Figures 2.7 and 2.8 one can see that none of these have associated X-ray emission.

Due to the presence of the WAT at z=0.2, we consider this redshift system as likely associated with N_{Diff} (see arguments in §5.1). To assess the significance of the clustering at this redshift, we used the SDSS photometric galaxy database (Adelman-McCarthy et al., 2007) and made a histogram in redshift of all the galaxies within a radius of $6'$ ($\sim$1 Mpc at z=0.2) from the WAT. We then subtracted a histogram (normalized to the same number of total counts) of a roughly 2×2 degree field around the WAT, in order to subtract out any systematics in SDSS's photometric redshifts. The results are displayed in Figure 2.11. Figure 2.12 shows the spatial distribution of galaxies (number of galaxies/pixel at the redshift of the WAT z=0.2±0.05) from the SDSS photometric data. A weak clustering of galaxies is seen around the WAT. We also show in Figures 2.11 and 2.12, for comparison, the results from two X-ray selected clusters at similar redshifts (discussed in §5.1). To assess the relative richness of this group/cluster, we followed the analysis used in Gal et al. (2003) for estimating the richness of clusters found in the POSS-II survey. We took the number of galaxies (above a background value determined from the surrounding 2x2 degree field) within $\sim$1 Mpc with an absolute R magnitude of $-22.53 < M_R < -19.53$ taken from the SDSS photometric data. The grouping of galaxies associated with the WAT has a richness of 16, which is on the poorer end of the overall distribution of richnesses in DPOSS (Gal et al., 2003). We should note that the cluster at z=0.073 detected by Gal et al. (2003) is also very close to N_{Diff}, and is just as likely to be associated with the diffuse emission as the WAT grouping of galaxies, but the issues discussed in §5 apply to either case. The cluster at z=0.073 had a richness of 24.9, also significantly poor, and roughly corresponding to an Abell richness class of R<0 (Abell et al., 1989; Gal et al., 2003).

If we allow for the proximity of S_{Diff} with N_{Diff} to be coincidental, then identifying

the optical system that is physically connected with S_{Diff} is not straightforward. The three likely possibilities are the z$\sim$0.04, 0.073, and 0.2 groupings of galaxies. We visually searched the spatial distribution of galaxies from the SDSS photometric catalog to find a redshift where there was significant clumping in or near S_{Diff}, without success. The spectroscopic database of galaxies in SDSS, while much sparser, does reveal a $\sim$5 Mpc filament of galaxies surrounding S_{Diff} at redshifts of $0.0352 < z < 0.0441$ (Figure 2.13). Many of these galaxies are those that make up the two groups previously detected in this region (Miller et al., 2005; Merchán & Zandivarez, 2005), but looking at a wider field reveals the larger filament. We performed the same richness analysis on the filament (centered on RA=122.224, DEC=38.883, 1 Mpc radius) as we did with the WAT group, and found a richness of 13. Figure 2.14 shows a wedge diagram of redshift vs. RA for SDSS galaxies with spectra in a roughly 4×4 degree field around 0809+39. We have indicated the range of galaxy redshifts that are plotted in Figure 2.13. Groupings of galaxies at higher redshift were not correlated spatially with S_{Diff}.

2.5 Physical Origin of the Radio Emission

We now turn our attention to the physical origin of the diffuse emission. Though we cannot strictly rule out a Galactic origin for either source, the emission is not morphologically similar and is far brighter than typical diffuse galactic emission in this region. We hereafter assume that both components are of extragalactic origin. There are many different types of extragalactic large-scale diffuse radio emission (e.g., Kempner et al. , 2004), but they in general fall within one of two basic classes: 1) Those directly powered by current AGN activity; 2) Those associated with processes in the intracluster medium (ICM). We include in the second class emission related to processes in the intergalactic plasma of galaxy filaments (Kim et al., 1989; Giovannini et al., 1990; Bagchi et al., 2002; Kronberg et al., 2007). In the vast majority of cases, determining the identification is straightforward. Either the diffuse region is directly connected (via jets or filamentary bridges) to an active radio galaxy, or there is a rich cluster of galaxies nearby whose potential well (highlighted by $\sim 10^8$ K, X-ray emitting gas) provides an obvious energy source for particle acceleration (via gravitational collapse/accretion –> shocks/turbulence etc).

Both sources in 0809+39 are unique in that neither of these conditions apply (see Delain & Rudnick 2006 for two similar sources). There are no cataloged X-ray emitting clusters nearby, only groups and poor clusters of galaxies. An AGN origin for these sources is also not obvious. In this paper we narrow our analysis to the two most likely (or least improbable) sources for the radio emission.

2.5.1 Northern Component

In this section, we: 1) Rule out N_{Diff} being an extended radio lobe directly powered by the WAT; 2) Give evidence that N_{Diff} is a classical "radio relic"; 3) Compare N_{Diff} with other relics and conclude that it has an anomalously high radio/X-ray luminosity ratio; 4) Determine that the X-ray luminosity is appropriate for this optical richness, and is thus not to blame for the abnormal luminosity ratio; 5) Examine possible sources of the relativistic electrons such as direct acceleration from the thermal plasma, adiabatic compression (only) of fossil WAT plasma, and reacceleration of fossil WAT plasma. We conclude that the most likely source is reacceleration of fossil plasma from past WAT activity.

We first consider whether N_{Diff} could be lobe emission from an AGN. The nearby WAT (F2) is the only reasonable candidate as an AGN source. However, they are spatially well separated, with a peak to peak distance >500 kpc at z=0.2. While the FWHM of the long axis of N_{Diff} is $200''$, there are faint wings that extend out to $600''$. This corresponds to ∼2 Mpc at z=0.2, which is a size comparable to that of a giant radio galaxy (GRG). However, its morphology is unlike any other GRG known (e.g., Machalski et al., 2001). We can also consider the lifetime of particles emitting at 1.4 GHz. The minimum energy magnetic field for N_{Diff} is $B_{min} \sim 0.6$ μG, which fixes the Lorentz factor at $\gamma \sim 2 \times 10^4$ and results in inverse Compton losses dominating the lifetime. From Sarazin (1999)

$$t_{IC} = 2.3 \times 10^{12} \gamma^{-1} (1+z)^{-4} \ yr, \tag{2.2}$$

which for N_{Diff} is $t_{IC} \sim 10^{7.7}$ yr. Relaxing the minimum energy requirement for magnetic field strength, we can calculate the maximum lifetime for any electron radiating at 1.4 GHz following the prescription of Sarazin (1999). Assuming a redshift of z=0.2

yields a maximum lifetime of $t_{max} \sim 10^8$ yr, similar to that calculated above using B_{min}.

If we assume a 1 keV gas temperature and only hydrogen gas the sound crossing time is $t_{sc} \sim 10^{9.1}$ yr. Therefore the timescale for 1.4 GHz IC losses will be much shorter than the diffusion/sound-crossing time (from the WAT to N_{Diff}). If the WAT was the original source for the N_{Diff} plasma, e.g. from an earlier outburst, then there must have been some re-acceleration or adiabatic enhancement. This is no surprise because this has been a longstanding result for radio halos and relics.

There are several lines of evidence that point toward N_{Diff} being a radio "relic" source associated with a poor cluster at z$\sim$0.2: 1) Both the clumping in redshift and the existence of the WAT (Owen & Rudnick , 1977) indicate the presence of a cluster; 2) WATs are also known to be associated with merger dynamics (Pinkney, 1993; Gomez et al., 1997; Roettiger et al., 1996; Loken et al., 1995; Pinkney et al., 2000; Blanton et al., 2003). Additional supporting evidence for merger activity near N_{Diff} comes from the multiple X-ray peaks seen in Figure 2.8, one of which is coincident with a z=0.27 SDSS galaxy. Currently all known radio relic or halo sources have been found in/near clusters in a disturbed dynamical state (Feretti, 2006); 3) The long axis of the diffuse emission is perpendicular to the line connecting N_{Diff} and the WAT, typical of relic sources; 4) The diffuse emission is highly polarized, also typical of radio relic sources (e.g. Giovannini & Feretti 2004); 5) The magnetic fields are parallel to the long axis of the emission, suggesting shock compression.

All of these point toward N_{Diff} being either a Radio Phoenix or Radio Gischt (Kempner et al. , 2004), depending on whether the "seed" plasma came from an extinct radio galaxy lobe or was initially accelerated at a cluster accretion shock, respectively. The curvature of the WAT (from Figure 2.2) is toward the North, suggesting infall from the South. With a longest linear extent of $\sim$2 Mpc, N_{Diff} is comparable to larger relic sources around rich clusters of galaxies (Giovannini et al., 1999). For radio relics where the spectral index distribution is known, the edge farthest from the cluster is always sharper and has a flatter spectrum (Giovannini & Feretti, 2004). Though N_{Diff} does not exhibit this behavior (see Figure 2.3), we should note that the source is only a little more than a single WSRT beam thick in the transverse direction. Therefore a higher resolution spectral index map is needed to confirm this.

We can now ask how N_{Diff} compares to other observed radio relics. Radio halos,

diffuse radio emission centered on some clusters of galaxies, are known to exhibit a good correlation between their radio luminosity and the X-ray luminosity of their associated cluster (e.g., Feretti, 2003, 2006). A similar but weaker correlation for radio relics has been claimed by Giovannini & Feretti (2004), who quoted $P_{1.4GHz} \propto 10^{K} L_x$, where K ranged from 0.8 to 2.2. We have compiled a relatively complete list of known relics with available 1.4 GHz flux measurements and plotted their radio luminosities vs. X-ray luminosities in Figure 2.15 (compiled from Giovannini, Feretti & Stanghellini , 1991; Giovannini et al., 1999; Kempner & Sarazin, 2001; Govoni et al., 2001; Slee et al., 2001; Govoni et al., 2005). N_{Diff} is at least an order of magnitude too luminous (underluminous) in the radio (X-ray). We examine several possible explanations as to why the radio or X-ray emission from the relic source N_{Diff} is not what we would expect from the radio/X-ray luminosity relation for rich galaxy clusters. From the observed correlation, N_{Diff} should have an $L_x \sim 10^{44-45}\ erg\ s^{-1}$ from 0.1-2.4 keV, but from XMM observations we measure a 3σ upper limit of $L_x \approx 1 \times 10^{43}$ erg s^{-1}. We examine the two quantities in this relation separately, starting with the X-ray luminosity.

It is possible that the grouping of galaxies that N_{Diff} is associated with is massive enough to emit the expected amount of X-rays (i.e. $\sim 10^{44-45}$ erg s^{-1} at 0.1-2.4 keV), but for some reason they are not observed. Perhaps the grouping will have the "correct" X-ray luminosity eventually, but we have caught it in a very early evolutionary state where the thermal gas has not reached the needed density or temperature to emit sufficiently in the X-rays. The optical properties of the WAT group (§4.2), however, are not representative of massive X-ray emitting clusters (see, e.g., Ledlow et al. 2003 for optical vs. X-ray properties of Abell clusters). To further show this, we examined the optical properties of the X-ray selected[3] clusters RXCJ1327.0+0211 and RXCJ2155.6+1231, both of which have a similar redshift {0.259, 0.192} to the WAT and a L_x ={1.67, 1.12}$\times 10^{45}$ erg s^{-1}, respectively (Popesso et al., 2004). For the optical data we again used the SDSS photometric galaxy database and performed the same analysis as with the WAT system (§4.2). Figure 2.11 shows the histograms and Figure 2.12 the distribution of galaxies with the same contour levels as the WAT system. The X-ray clusters show much stronger clustering than the WAT system, both spatially and in redshift. Using the same richness analysis that we used for the WAT group, RXCJ2155.6+1231

[3] We used X-ray selected clusters to avoid pre-selecting optically rich clusters.

and RXCJ1327.0+0211 have richnesses of 42 and 53, respectively, consistent with large X-ray luminous clusters (e.g. Ledlow et al. 2003). The lack of X-ray emission in the WAT group, therefore, is consistent with its poor optical properties, and cannot explain the discrepant radio/X-ray luminosity ratio seen in Figure 2.15.

We now examine the radio luminosity, which is apparently two orders of magnitude too luminous given the observed correlation for radio relics. We proceed under the assumption that N_{Diff} is related to the presence of a shock, as we argued earlier, and attempt to understand the source of the relativistic electrons that are causing the synchrotron emission. The two likely possibilities are that the electrons were accelerated directly out of the thermal plasma by diffusive shock acceleration (DSA), or the seed electrons came from fossil plasma from past AGN activity and were re-accelerated and/or adiabatically enhanced by the shock.

Miniati et al. (2001) performed a cosmological simulation that included only DSA of cosmic rays from the thermal environment and did not include fossil AGN plasma. They report a correlation between 1.4 GHz radio luminosity from primary electrons (those accelerated at shocks) and cluster temperature (see Figure 6 of that paper) that is roughly consistent with the observed correlation for radio relics shown in Figure 2.15. The radio/X-ray luminosity ratio of N_{Diff} is therefore inconsistent with the results of Miniati et al. (2001). We can examine the conditions under which their simulations would have produce the observed P_ν/L_X ratio of N_{Diff}. Using observed L_X vs. $T_{cluster}$ relations (Hartley et al., 2008) and theoretical expectations for low-density environments (Ryu et al., 2003), we assume a $T_{cluster} < 1$ keV. Miniati et al. (2001) would then predict $P_\nu(1.4\ \mathrm{GHz}) \approx 1 \times 10^{22}$ W Hz^{-1}, assuming an acceleration efficiency of 10^{-4} and an electron to proton injection ratio of $R_{e/p}$=0.01. Therefore, either the acceleration efficiency needs to be ~ 0.01 or $R_{e/p} \sim 1$ in order for Miniati et al. (2001) to reproduce the P_ν/L_X ratio of N_{Diff}. It is thus physically possible to use DSA out of the thermal gas to create N_{Diff}, but it is not clear why the efficiency or $R_{e/p}$ should be so anomalous in this region.

The other possible source of seed electrons is fossil or "relic" plasma from past AGN activity, presumably from the nearby WAT. There are two possible mechanisms for reviving old plasma. The shock can either adiabatically enhance the relativistic particles and magnetic fields of the relic plasma *only* (e.g., Enßlin & Gopal-Krishna,

2001), or the shock can reaccelerate the particles as well.

In the case of pure adiabatic compression, let us compare the energy content of the current WAT radio lobes and N_{Diff}. From the FIRST data, the eastern lobe of the WAT has a minimum energy magnetic field of $B_{min} \approx 2.7$ μG and a total energy of E $\approx 6 \times 10^{57}$ erg. N_{Diff} has $B_{min} \approx 0.6$ μG and E $\approx 3.4 \times 10^{59}$ erg. It appears that the energy contained in N_{Diff} cannot be explained by adiabatically compressing an extinct radio lobe similar to the current lobes of the WAT. This does not rule out this scenario however, since the current activity of the WAT may not be indicative of past activity, and WATs in general are known to have energies of the same order as N_{Diff} (e.g., De Young, 1984).

The reacceleration of the fossil electrons can further increase the emissivity of the relic plasma (Blandford & Eichler, 1987; Micono et al., 1999; Markevitch et al., 2005), potentially by an order of magnitude, depending on the pre-shock spectral index and the shock compression ratio R. From the spectral index of N_{Diff}, $\alpha = -1.12$, we can find the shock compression ratio $R = \frac{\alpha-1}{\alpha+1/2} = 3.4$ (Bell, 1978; Drury, 1983) and Mach number M ≈ 2.1. The Mach number is a reasonable one for this environment (e.g., Ryu et al., 2003). In short, energetically it is not out of the question that the radio emission N_{Diff} was created by shock compressed fossil plasma from the WAT, assuming that the WAT's past activity was stronger than it is currently.

Given that DSA of electrons from the thermal plasma reproduces the observed radio vs. X-ray luminosity correlation for radio relics, from which N_{Diff} is a clear outlier, we conclude that reacceleration and/or adiabatic compression of fossil plasma from the WAT source is a more likely origin for the radio emission in N_{Diff}. Due to the fact that current activity of the WAT is not energetically comparable to N_{Diff}, we must invoke more powerful activity in the past in order to make the adiabatic compression/reacceleration hypothesis work. Had we associated N_{Diff} with the z$\sim$0.07 group of galaxies (§4.2, Figure 2.10), the P_ν/L_X ratio would still have been two orders of magnitude too large for the observed correlation for radio relics. Our arguments would have proceeded the same way, except we would have needed to invoke past activity from an *undetected* AGN to explain the discrepant radio luminosity.

2.5.2 Southern Component

Many of the same issues that we found with N_{Diff} arise when we consider possible origins for S_{Diff}. If we consider an AGN origin, the morphology of S_{Diff} (Figure 2.2) is reminiscent of a WAT source centered on the FIRST radio source F7. F7, however, does not have an optical counterpart in SDSS. If it is an unidentified WAT, its redshift is likely to be $z > 0.5$ (Schmidt et al., 2006), making its total linear extent >3 Mpc. Figure 2.16 shows a plot of 1.4 GHz radio power vs. linear extent for a sample of WAT sources from Pinkney et al. (2000). If S_{Diff} were indeed at a redshift of $z > 0.5$, it would have a linear size that far exceeds typical WATs in this sample. It is also possible that one of the z=0.04 galaxies that makes up the filament (Figure 2.13) hosts an AGN that created the extended emission, but none of the galaxies at this redshift (with spectra in SDSS) show signs of AGN activity. However, the AGN could have been disrupted and disappeared leaving the lobe emission behind (e.g., Parma et al., 2007), as long as this happens on a timescale less than the 1.4 GHz electron maximum lifetime of 10^8 yr (see discussion in §5.1). Assuming S_{Diff} is at a redshift of z=0.04, its total energy would be $E \approx 7.9 \times 10^{57}$ erg and the minimum energy magnetic field would be $B_{min} \approx 0.6$ μG, not atypical for WAT lobe emission (see §5.1).

S_{Diff} could be caused by ICM or IGM processes, similar to our claim for N_{Diff}. From Figure 2.7 we can see that, like N_{Diff}, there is no cluster X-ray emission detected in either ROSAT or XMM. The apparent filament in which S_{Diff} is embedded offers an intriguing origin for the diffuse emission. Unlike other diffuse radio sources that have claimed to be part of filamentary large-scale structure (Kim et al., 1989; Giovannini et al., 1990; Kronberg et al., 2007), S_{Diff} is not near *any* massive clusters. At 390 kpc long, S_{Diff} is smaller than the ∼1.5 Mpc emission in the Coma-Abell 1367 supercluster (Kim et al., 1989; Giovannini et al., 1990) or the $4 - 5$ Mpc radio regions found by Bagchi et al. (2002) and Kronberg et al. (2007). Bagchi et al. (2002) detected radio emission coincident with a relatively isolated filament of galaxies (in the region of the cluster ZwCl2341.1+0000), similar to S_{Diff}. Unlike S_{Diff}, however, the filament was also detected in X-rays with a L_X(0.1-2.4 keV)$\approx 10^{44}$ erg s^{-1}. Though the linear extent of S_{Diff} is small compared to the overall size of the filament, it is in the densest region. The radio luminosity of S_{Diff} (Table 2), assuming it is embedded in the z∼0.04 filament, is also several orders of magnitude above the radio vs. X-ray luminosity correlation for

known relics (Figure 2.15). Therefore, if S_{Diff} is indeed caused by processes in the ICM or IGM, the lack of X-ray emission poses the same problem as it does for N_{Diff}. We do not have an active radio galaxy nearby, however, to offer an explanation for S_{Diff}'s increased radio luminosity.

2.5.3 Implications

A consequence of attributing N_{Diff}'s abnormally high radio luminosity to the presence of relic radio plasma is that *any* relic that forms in the presence of preexisting magnetized plasma will show an increased luminosity. A signature of this scenario might be in the scatter of the currently observed relics, which could be correlated with the availability of relic plasma from current/past AGN activity. However, the Coma relic 1253+275, which is a relic that is seemingly being fed magnetized plasma from the NAT source NGC 4789 (Enßlin & Gopal-Krishna, 2001), is less radio luminous than other relics with similar X-ray luminosity (Figure 2.15). This is contrary to our hypothesis that fossil AGN plasma increases the radio luminosity of relic sources. There are, however, many factors that contribute to the presence and strength of synchrotron emission at a structure formation shock. Miniati et al. (2001) found scatter of the same order as Figure 2.15 for the 1.4 GHz emission of primary electrons in their simulations. This is after integrating the radio luminosity over a spherical volume with a radius of 1.3 h^{-1} Mpc, and without including relic plasma from past AGN activity. Since Miniati et al. (2001) used a fixed radius for all the clusters, the radio luminosities they found depend on the details of the current dynamical state and the location of shocks within (or just outside) each cluster. In practice, radio relics represent only a single (perhaps partially) illuminated shock front associated with a cluster. It is thus no surprise that there is such a large scatter in the observational correlation.

What then makes these two sources, N_{Diff} and S_{Diff}, special? Why have radio relics only been found around rich X-ray clusters up until now? Part of the observational problem is most certainly selection and bias effects. Thus far most searches for relics have focused on rich X-ray emitting clusters, an exception being Rudnick, Delain & Lemmerman (2006), from which 0809+39 was found. Even Delain & Rudnick (2006) found only a handful of new candidates, but this could be the tip of a larger distribution

that is currently below the NVSS and WENSS surface-brightness limits. On the theoretical side, most simulations that include synthetic radio observations, e.g., Miniati et al. (2001) and Pfrommer, Enßlin & Springel (2008), do not include pre-existing relativistic plasma from past/current AGN. Hoeft et al. (2004) simulated the merger of two M $\approx 1.6 \times 10^{13}$ $M_{\odot}$ clusters of galaxies in order to track the revival of relic radio plasma. They found that efficient re-acceleration only occurred in regions where the ratio of magnetic pressure to gas pressure is $P_B/P_{gas} < 0.01$, which explains why this process is inefficient in the inner regions of clusters where $P_B \approx P_{gas}$. One property that distinguishes N_{Diff} and S_{Diff} from other known relics is that they reside in poor environments. Perhaps poor clusters and groups do not confine relativistic plasma as well, so that radio lobe plasma from AGN can be driven farther (and faster) into the low density regions than they would in rich clusters (we are speaking here about driven jets, not buoyant forces). For adiabatic compression to be most effective, one wants "younger" electrons, higher compression factors (steeper shocks in cooler gas), and lower magnetic fields (i.e., less radiative losses; Enßlin & Gopal-Krishna 2001). The first two of these conditions can be effectively achieved in the above scenario. Simulations focusing on the evolution of relic AGN plasma in low-density environments are needed in order to fully assess the plausibility of this idea.

2.6 Summary

We have presented detailed radio observations of the diffuse source 0809+39 in an attempt to discover the origin of the synchrotron emission. To summarize the key messages:

• Evidence points toward N_{Diff} being a radio relic, i.e. shock excited synchrotron emission, related to a poor z$\sim$0.2 group of galaxies.

• S_{Diff}'s origin is ambiguous, though its coincidence with a filament of galaxies at z$\sim$0.04 makes it possible that it could be synchrotron emission from filamentary large-scale structure or relic emission from an extinct radio galaxy within the filament.

• Both N_{Diff} and S_{Diff} are more radio luminous than their X-ray properties would suggest, given the apparent $P_\nu$vs.L_X correlation of known radio relics.

• Total energies in N_{Diff} and S_{Diff} are comparable to luminous, diffuse radio galaxies,

and could be the result of adiabatic compression/reacceleration of past AGN activity.
• When analyzing diffuse radio emission beyond the environments of rich galaxy clusters, determining the true physical origin of these structures is non-trivial, especially at very low surface-brightness levels where emission related to large-scale structure is expected.

The issues presented here highlight the difficulty in finding a unified physical model for radio relics. Detailed observations of the radio spectrum, coupled with deep X-ray observations, are needed for a large sample of radio relics in both poor and rich environments in order to determine such a model.

We gratefully acknowledge help and advice from G. de Bruyn and M. Brentjens during our RM-Synthesis analysis of the WSRT data. We thank K. Delain for help in setting up the VLA and WSRT observations. Partial support for this work at the University of Minnesota comes from the U.S. National Science Foundation grants AST 0307600 and AST 0607674.

The Very Large Array is a facility of the National Science Foundation, operated by NRAO under contract with AUI, Inc. We also acknowledge the use of NASA's SkyView facility[4] located at NASA Goddard Space Flight Center. The Westerbork Synthesis Radio Telescope is operated by the ASTRON (Netherlands Foundation for Research in Astronomy) with support from the Netherlands Foundation for Scientific Research (NWO). The Digitized Sky Surveys were produced at the Space Telescope Science Institute under U.S. Government grant NAG W-2166. Archival observations obtained from XMM-Newton, an ESA science mission with instruments and contributions directly funded by ESA Member States and NASA, and ROSAT archives from HEASARC. Funding for the SDSS and SDSS-II has been provided by the Alfred P. Sloan Foundation, the Participating Institutions, the National Science Foundation, the U.S. Department of Energy, the National Aeronautics and Space Administration, the Japanese Monbukagakusho, the Max Planck Society, and the Higher Education Funding Council for England. The SDSS Web Site is http://www.sdss.org/. The SDSS is managed by the Astrophysical Research Consortium for the Participating Institutions.

[4] (http://skyview.gsfc.nasa.gov)

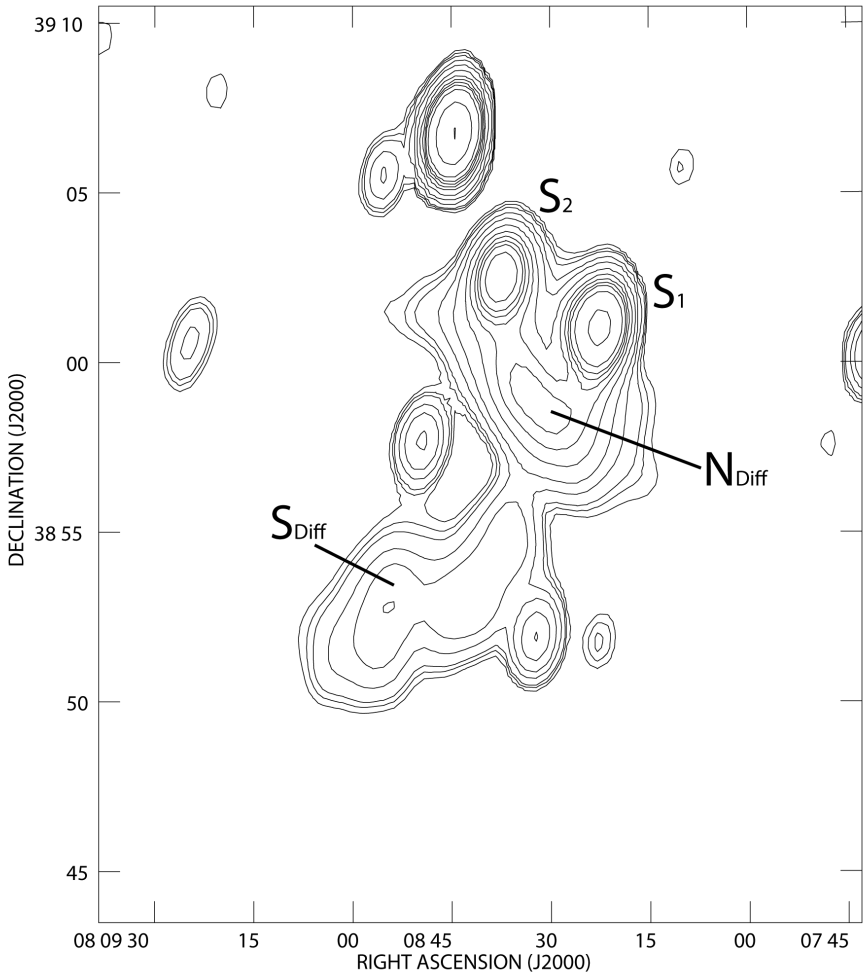

Figure 2.1: WSRT 351 MHz total intensity image with contour levels 8.254×10^{-3}(-0.4, 0.4, 0.5, 0.8, 1.2, 2, 3, 4, 6, 8, 16, 32, 64) Jy/(108″×60″ beam). S1 and S2 are "compact" sources at 351 MHz that show sub-structure at higher resolution (see Figure 2.2).

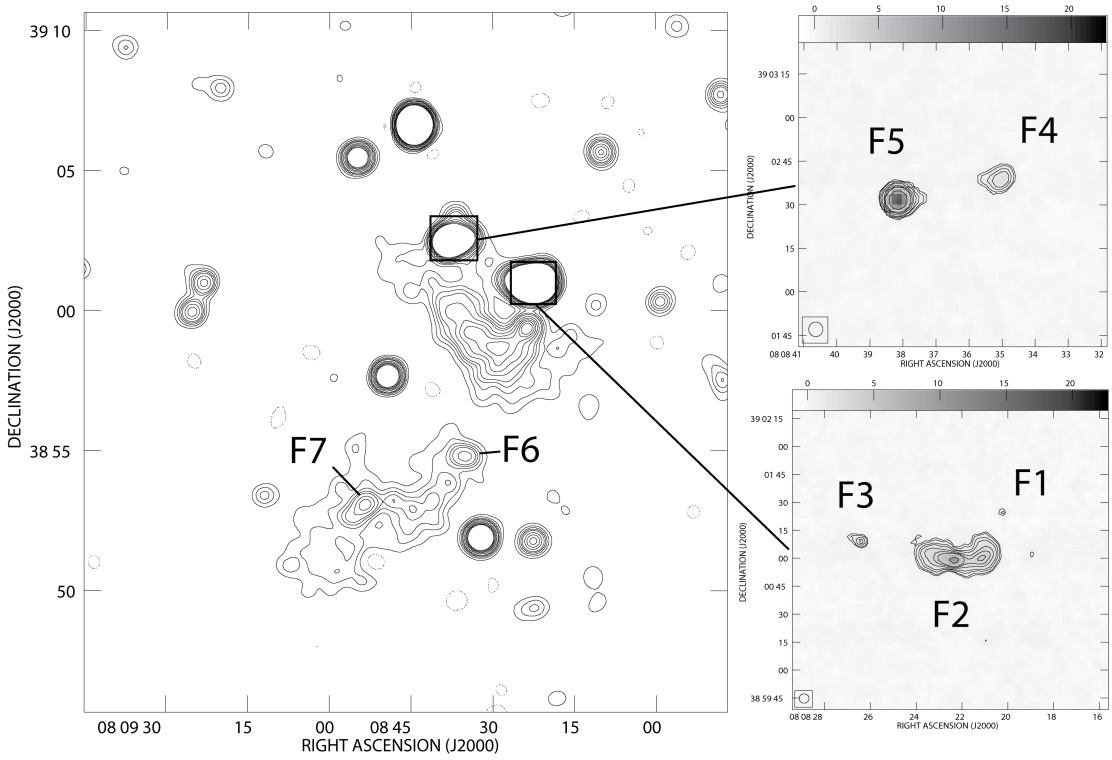

Figure 2.2: VLA I image (left) with contours 2.0×10^{-4}(-1, 1, 2, 3, 4, 5, 7, 9, 11, 13, 15) Jy/($40''\times40''$ beam). At right are close-ups views of S1 and S2 from the FIRST survey. Contours 4.0×10^{-4}(1.5, 2, 3, 4, 6, 8, 10, 20, 50, 100) Jy/($5''\times5''$ beam).

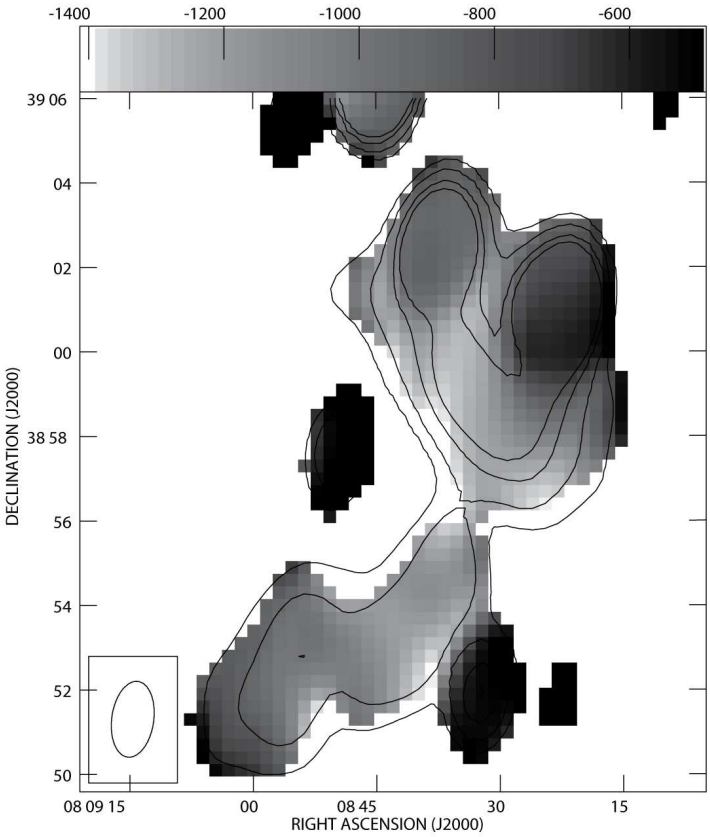

Figure 2.3: Spectral index map from 351 MHz to 1.4 GHz, with WSRT contours 8.25×10^{-3}(-0.5, 0.5, 0.8, 1, 2, 3, 6, 12, 24, 48) Jy/($108''\times60''$ beam).

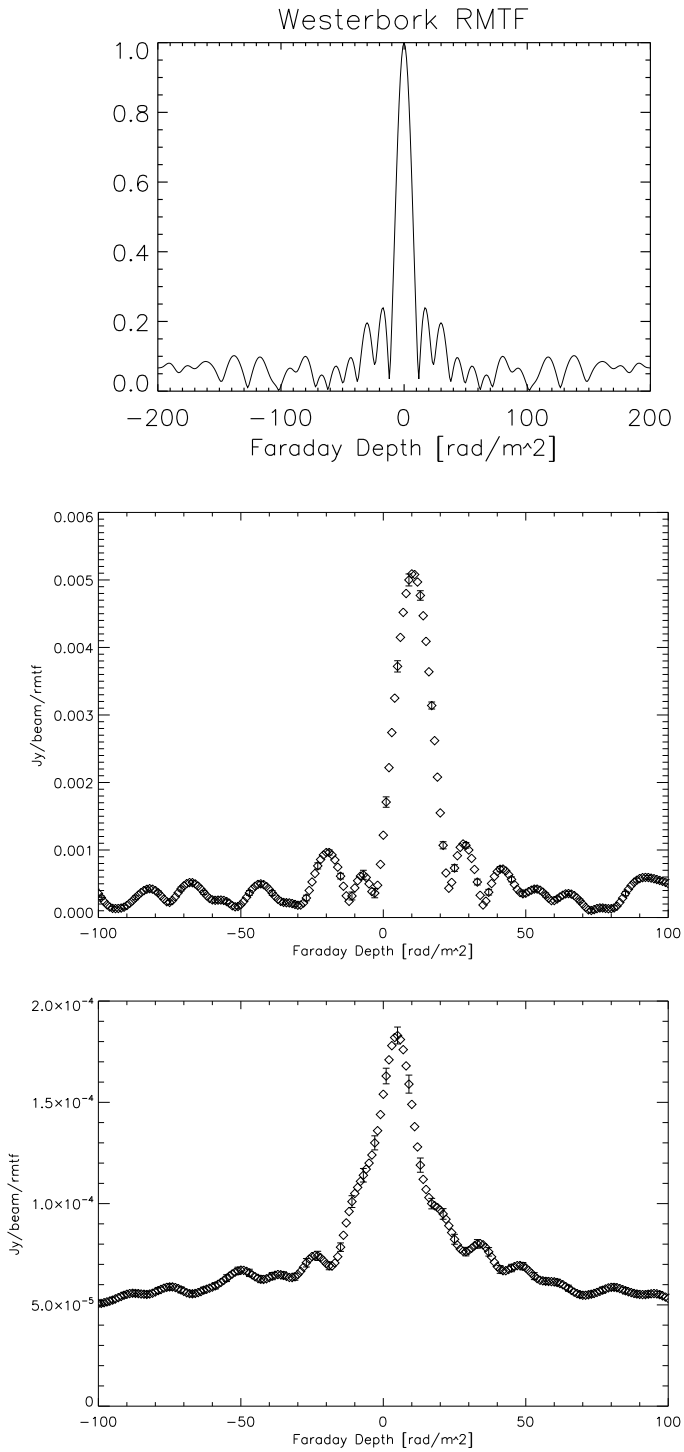

Figure 2.4: Top: Our RMTF; Center: Faraday spectrum for N_{Diff}; Bottom: Faraday spectrum for a large area of the Galactic emission. Characteristic error bars are shown.

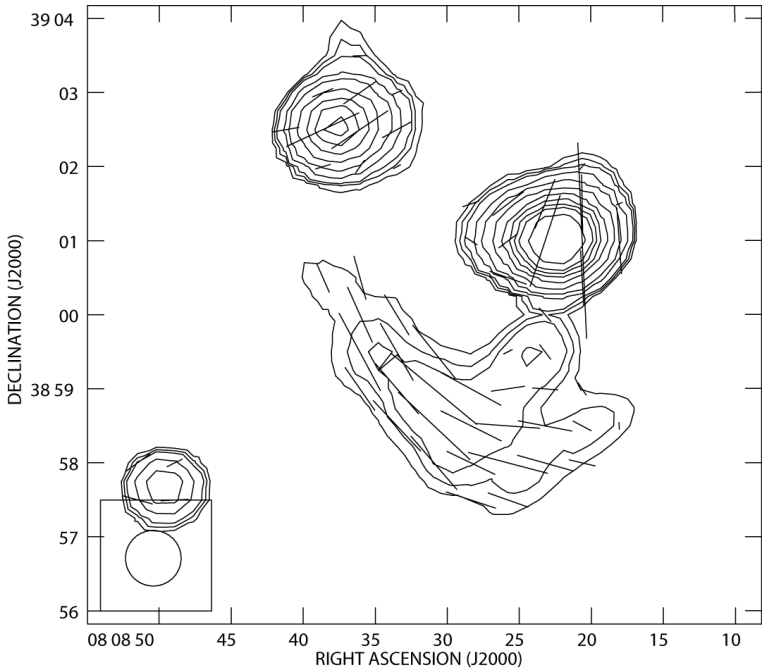

Figure 2.5: B field orientation obtained from derotating the NVSS to correct for a rotation measure of +12 rad m^{-2}. Contours are NVSS I at 4.9×10^{-3}(-0.3, 0.3, 0.4, 0.5, 0.8, 1.2, 2, 3, 4, 5, 6, 8, 16, 32, 64) Jy/($45''\times45''$ beam), and the magnetic field lines are $1''$=2.22×10^{-5} Jy/($45''\times45''$ beam).

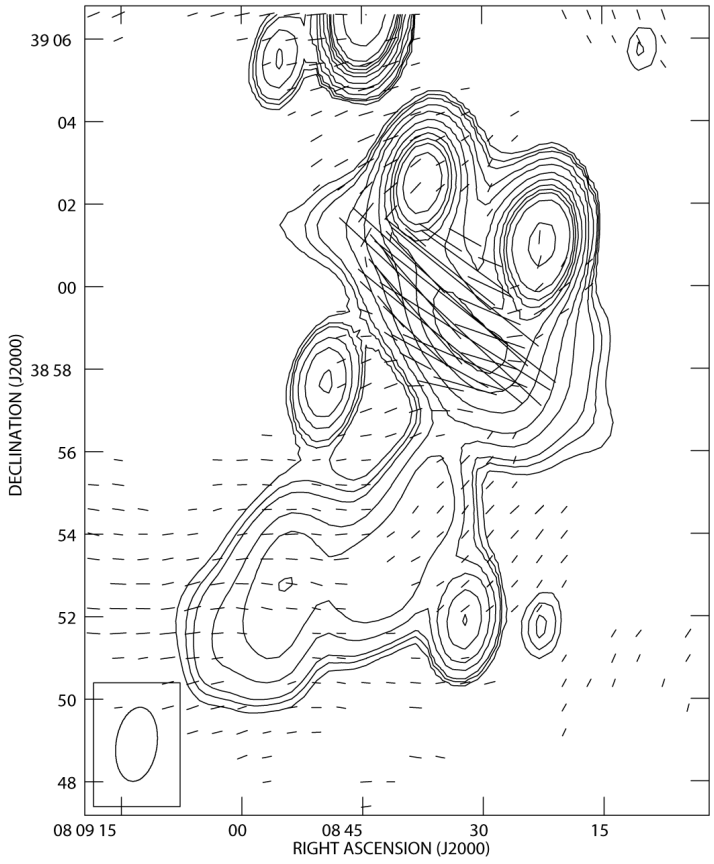

Figure 2.6: WSRT 351 MHz contour image of 0809+39 I (same contours and resolution as Figure 2.1) with corrected magnetic field vectors for the RM-Cube at $\phi = +12\ rad\ m^{-2}$. $1'' = 1.85{\times}10^{-5}$ Jy/($108''{\times}60''$ beam). The apparent "noise" in the polarized emission is actually real emission from our own galaxy.

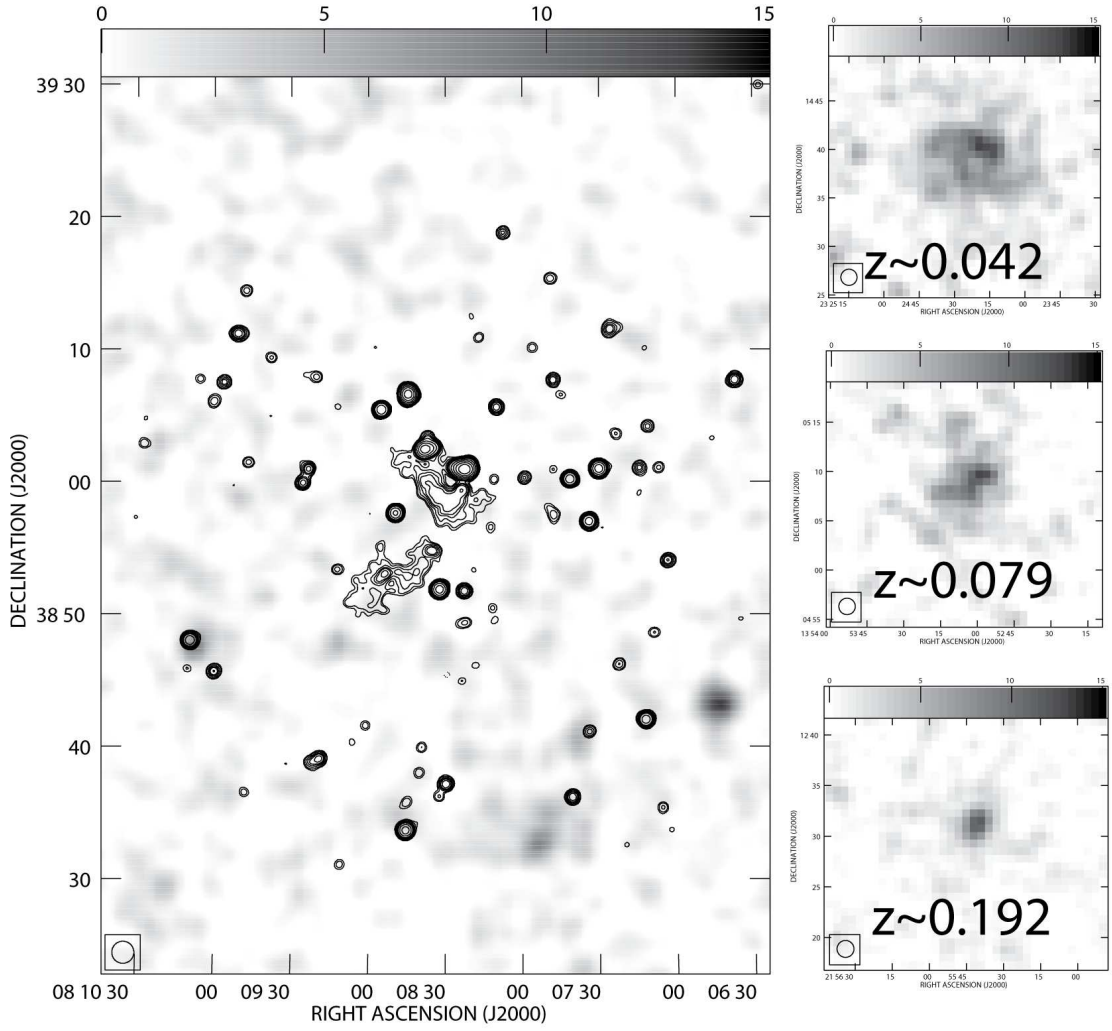

Figure 2.7: ROSAT broad (0.1-2.4 keV) continuum grayscale (convolved to 100″) with VLA L-band contours. To the right are ROSAT images of three X-ray selected clusters at the indicated redshifts, at the same grayscale and resolution as the 0809+39 ROSAT image.

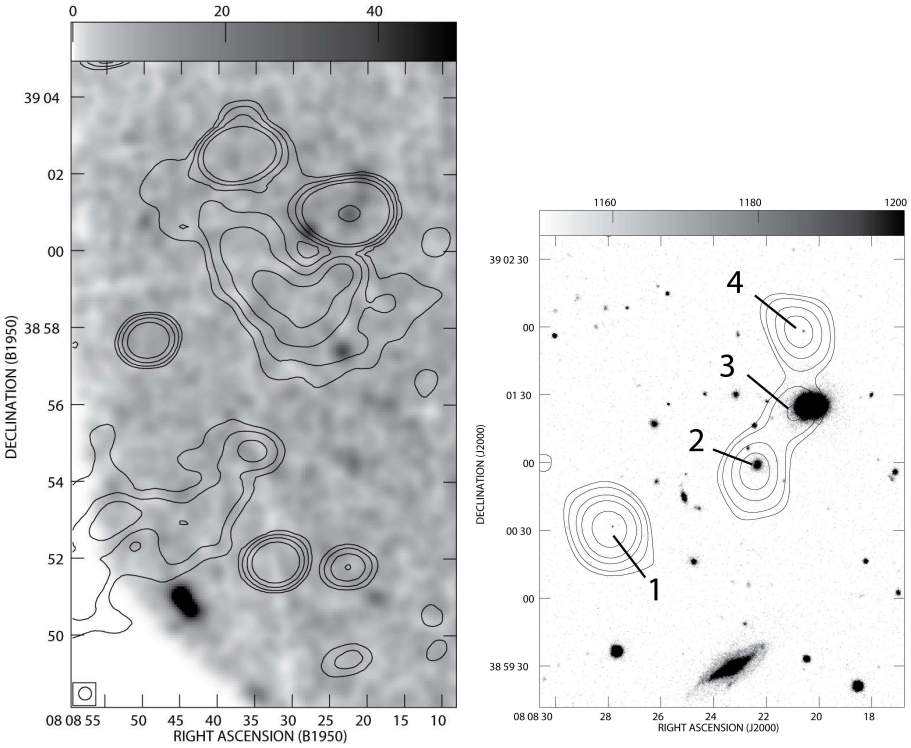

Figure 2.8: Left: XMM Epic observation in counts (convolved to 20″) with VLA radio contours 6.5×10^{-3}(0.05, 0.1, 0.2, 0.4, 8) Jy/(49″×42″ beam). Note that a faint X-ray source is coincident with F2 (the WAT seen in Figure 2.2); Right: SDSS R image with XMM EPIC contours. Grayscale is in units of counts, and the contours are 4.08×(3.5, 4, 5, 6, 8) counts. X-ray source 2 is the WAT (F2) and the galaxy near source 3 is coincident with compact radio source F1.

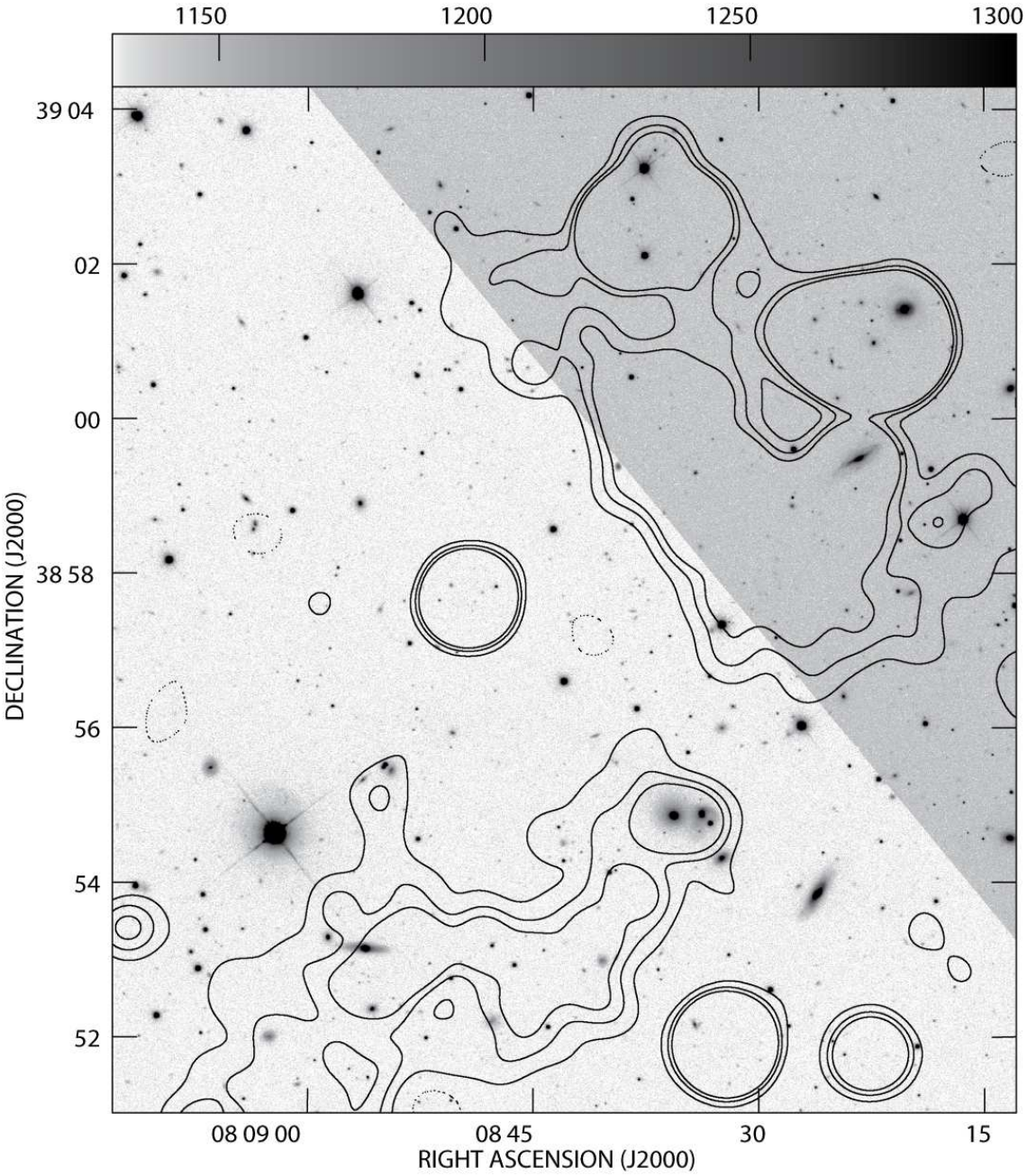

Figure 2.9: SDSS R mosaic grayscale (in counts) with VLA 1.4 GHz contours at 2.0×10^{-4} (-1, 1, 2, 3) Jy/($40''\times40''$ beam).

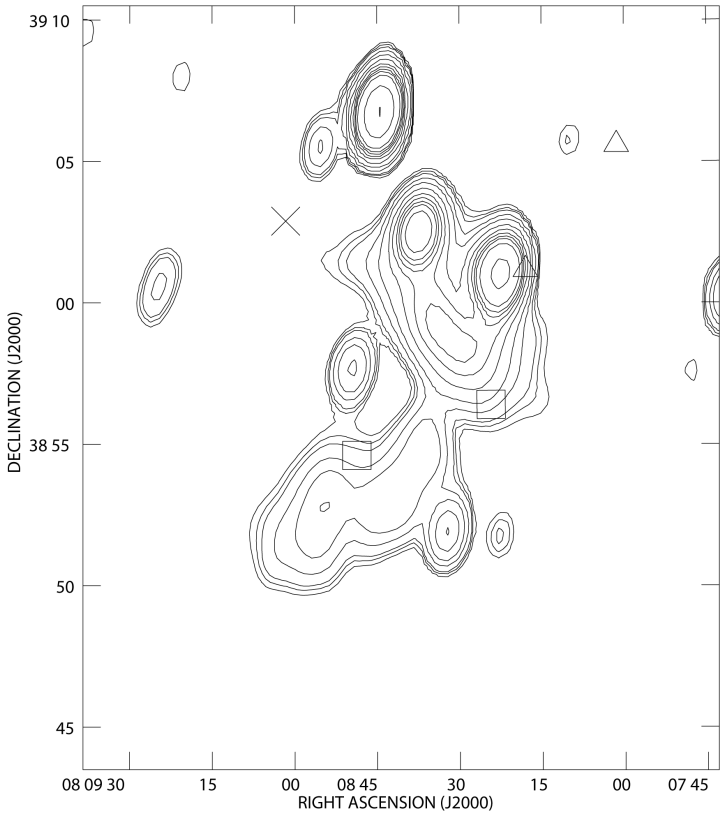

Figure 2.10: Plot of known groups/clusters in the 0809+39 region. Boxes are z≈0.04 systems, triangles are z≈0.07 systems, and the cross is a z≈0.11 cluster.

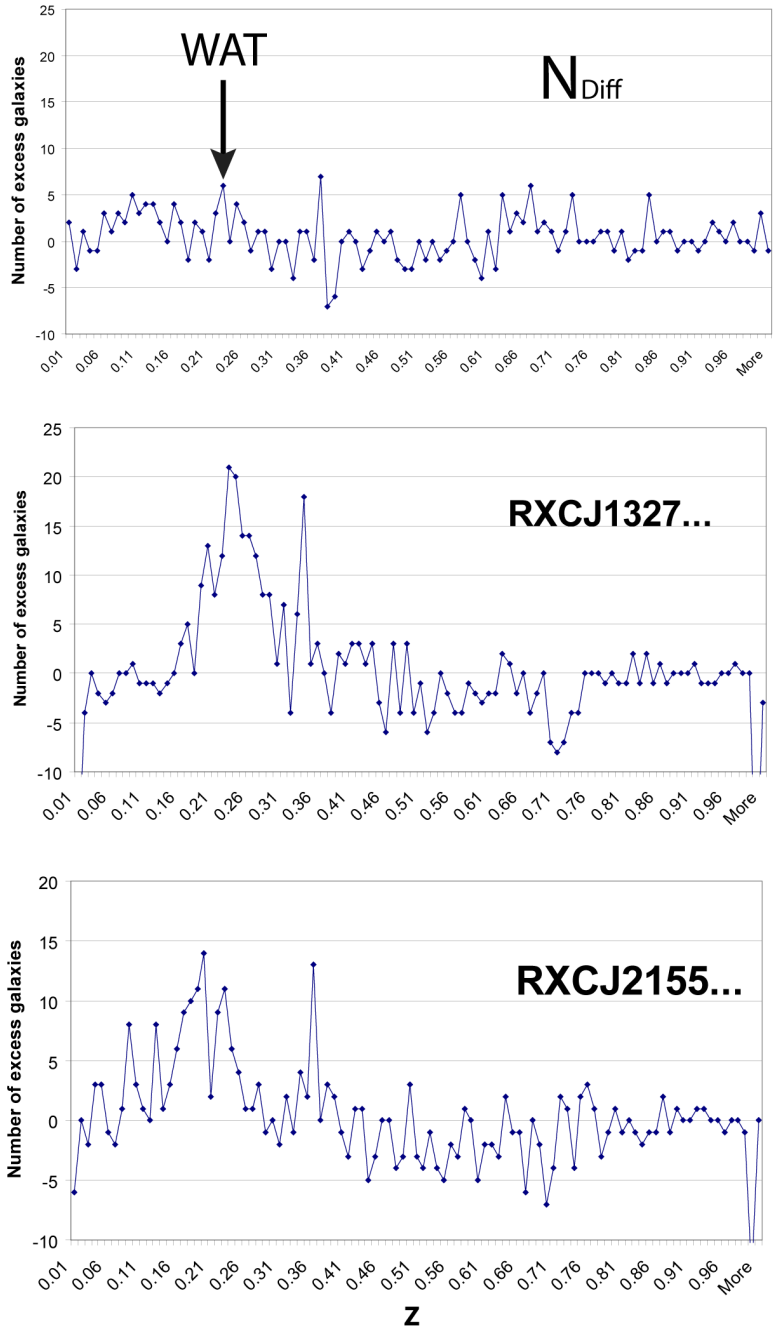

Figure 2.11: Histograms of galaxy photometric redshifts from SDSS for 6′ around the WAT source F2 (Top, see Figure 2.2) and the X-ray selected clusters RXCJ1327.0+0211 (Center) and RXCJ2155.6+1231 (Bottom) (Popesso et al. 2004). Note that all the histograms have a narrow peak at z∼0.35. This is an artifact of the template fitting method for calculating the photometric redshifts (Csabai et al. 2003; see Figure 16 in that paper).

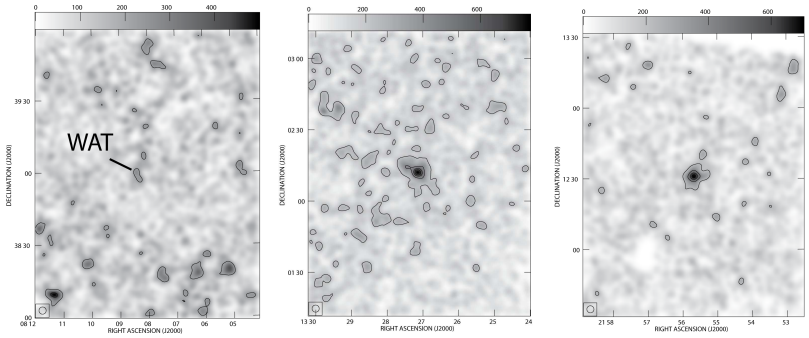

Figure 2.12: Distribution of galaxies from the SDSS photometric database with redshifts between $0.15 < z < 0.25$, smoothed to $6'$. Left: 0809+39; Using the same redshift limits we show two X-ray selected clusters for comparison: Middle: RXCJ1327.0+0211; Right: RXCJ2155.6+1231

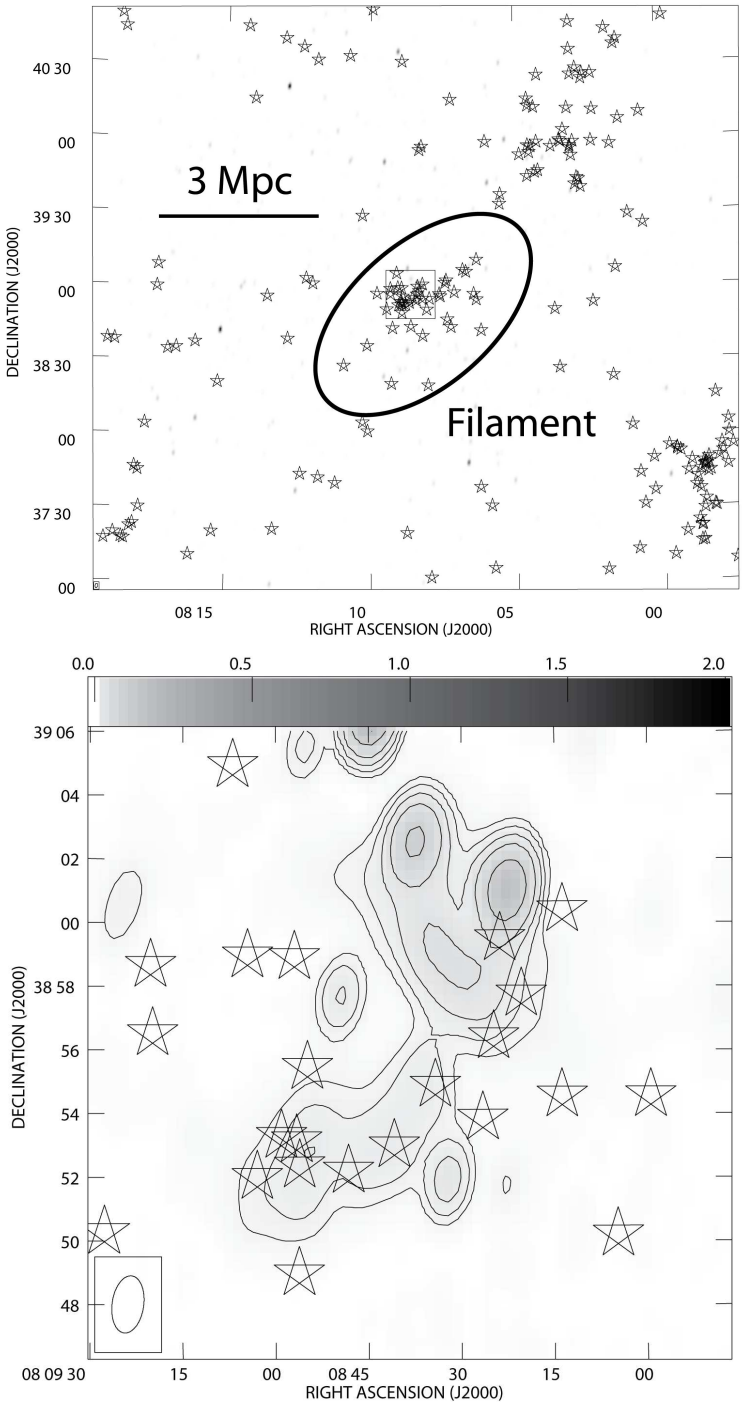

Figure 2.13: Top: Distribution of $0.0366 < z < 0.0448$ galaxies with spectroscopic redshifts in SDSS plotted as stars. Bottom: close-up view of the boxed region in the top panel. S_{Diff} is embedded in the filament of galaxies.

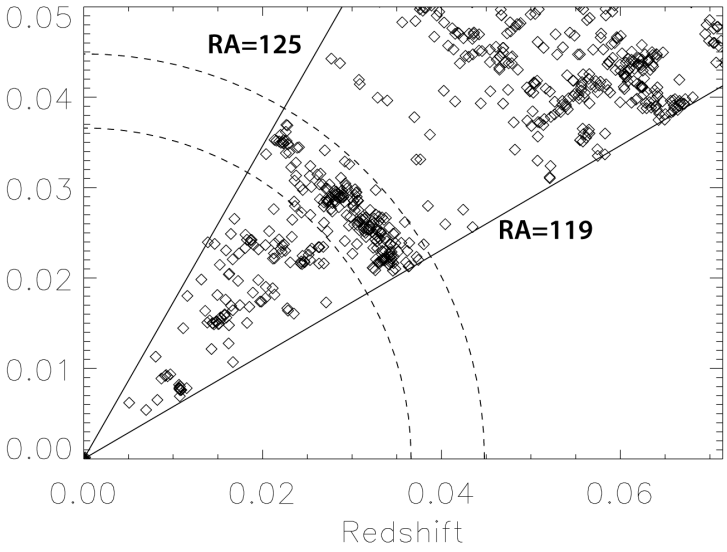

Figure 2.14: Distribution of redshift vs. RA for galaxies with spectroscopic redshifts in SDSS in a roughly 4×4 degree field around 0809+39. The dashed lines enclose the range in z used to create Figure 2.13 ($0.0366 < z < 0.0448$), and show the clustering of the filament galaxies. There are other significant structures at higher redshifts, but the filament at z=0.04 was deemed significant based on its spatial correlation with S_{Diff}.

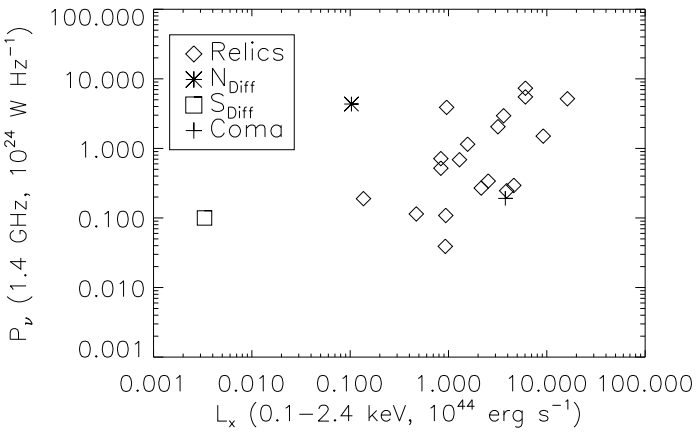

Figure 2.15: Plot of relic radio luminosity/Hz at 1.4 GHz vs. the 0.1-2.4 keV X-ray luminosity of the associated cluster. Compiled are 22 radio relics from Giovannini et al. (1991); Giovannini, Tordi, & Feretti (1999); Kempner & Sarazin (2001); Govoni et al. (2001); Slee et al. (2001); Govoni et al. (2005). They represent a complete list of radio relics that have reasonably reliable 1.4 GHz Flux density measurements.

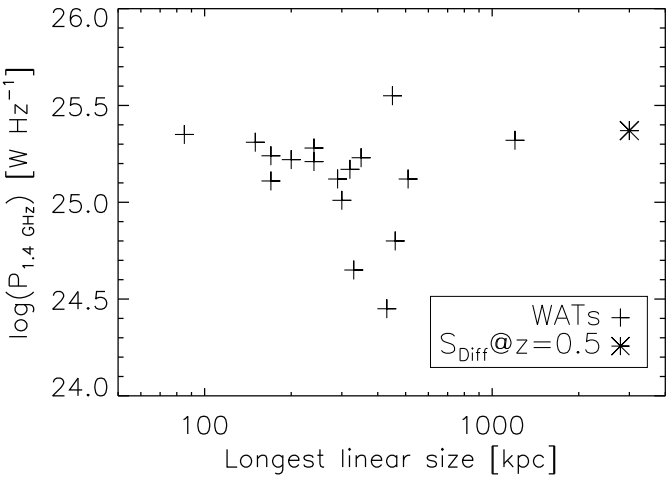

Figure 2.16: 1.4 GHz power vs. linear extent in kpc for a sample of WAT sources (Pinkney et al. 2000). S_{Diff}, if at redshift of z>0.5, is an extremely large radio galaxy.

Chapter 3

The Discovery of Diffuse Radio Polarization Structures in the NVSS

A slightly modified version of the chapter appears in The Astronomical Journal: Rudnick, L., & Brown, S. 2009, AJ, 137, 145

3.1 Introduction

Polarized synchrotron radiation is a powerful diagnostic tool for astrophysical relativistic plasmas. It provides information on the field direction, degree of order, and in some special situations, the actual field strength. Polarization's diagnostic power (and its sometimes ambiguous interpretation) for optically thin sources arise from the combination of two factors – its vector nature, allowing for constructive/destructive interference, and the effects of radiative transfer, primarily Faraday rotation, along the line of sight.

There is a long history to the use of radio polarizations for structural studies. In our Galaxy, polarized emission allowed the mapping of the large scale structure of the magnetic field including very large angle structures such as Loop 1 (Berkhuijsen , 1971). More recently, higher resolution images have uncovered structures on a wide range of scales, including the influence of Faraday screens (Taylor et al. , 2003; Wieringa et al. ,

1993; Gaensler et al. , 2001). In addition, discrete objects such as supernova remnants and supershells are highly polarized, allowing study of their magnetic field structures and dynamics (Kundu , 1970; Milne & Dickel , 1975; Jones et al. , 2003; West et al. , 2007). Many extragalactic radio sources were found to be significantly polarized, from the pc-scale relativistic jets of blazars and other AGN (Wardle , 1971; Rudnick et al. , 1985) to the diffuse lobes of radio galaxies on scales of 100s of kpc (Stull et al. , 1975). In addition to its propitious qualities, polarized synchrotron emission is also important as a foreground for CMB polarization studies (Tegmark et al. , 2000).

Polarized objects like the Mpc-scale peripheral relics or gischt (e.g., Hanisch, Strom & Jaffe , 1985; Kempner et al. , 2004) around clusters of galaxies, presumably due to accretion shocks (Ensslin et al. , 1998) were the initial motivation for the current study. The current work was motivated by a desire to use polarization as a probe to push below the limits of confusion (Rudnick , 2004) to search for signatures of infall into and along the large scale filaments that are part of cosmic structure formation (Miniati et al. , 2001).

Although the Stokes parameters Q, U, and I for linearly polarized emission contain a great deal of information, the way in which they are processed and communicated necessarily destroys some of that information. In particular, whether or not a vector background subtraction (in Q and U) or spatial smoothing is done before calculation of the polarized intensity $P = [Q^2 + U^2]^{0.5}$ can cause features to appear or disappear in an image. Thus, it is often possible to re-process Stokes images and derive further information than emerged from their initial analysis. It was this type of thinking that led us to reconsider the polarization information present in the NRAO VLA Sky Survey (NVSS, Condon et al. , 1998). We note that the proper way to recover diffuse polarization information unconfused by smaller sources is to combine single dish and interferometer data. However, since there are angular scales and rotation measure ranges now reachable by the "allsky" NVSS that are unlikely to be duplicated in the near future, it is worth examining what information can be derived from this survey.

The NVSS is a 1.4 GHz survey (combining data from 1364.9 and 1435.1 MHz) conducted from 1993-1997 in the D and DnC configurations (lowest angular resolution) of the VLA, covering the 82% of the sky which is visible from its latitude. It is reproduced as 2326 $4^o \times 4^o$ images in Stokes parameters I, Q, and U at a resolution of 45". The

rms brightness is ∼0.45 mJy/beam (0.14 K), in I, with typical rms values of ∼0.29 mJy/beam (0.09 K) in Q and U at high galactic latitudes. Faraday rotation between the two NVSS bands eliminates any polarized emission in the images with $|\mathrm{RM}| \geq 340$ rad/m^2.

The information on large scale structures in the NVSS is limited by two effects. First, the snapshot observations and smallest projected spacings of ∼37 m produce grating lobes at ∼18', effectively eliminating the sensitivity to sources larger than that scale. In addition, the short spacings were further weighted down in the mapping procedure, to remove the large scale "pedestal" in the synthesized beam. Although no detailed study has been done, the NVSS is generally recognized to have little sensitivity to structures >15'. For most extragalactic studies, this provides a great benefit both in total intensity and polarization because it removes the effects of the strong large-scale galactic emission. However, there are many interesting galactic and extragalactic structures on intermediate scales that do not appear in the original survey.

It is possible to recover some of this intermediate scale structure from the NVSS linear polarization images. If a source has structure in Q and U on angular scales to which the interferometer is sensitive, then it will be detected even if the underlying total intensity (I) is much smoother and undetectable by the interferometer. Q and U often have smaller-scale fluctuations than total intensity because they are sensitive to field disorder, magnetic field direction, and Faraday rotation, none of which affects the total intensity. The recovery of such polarized features is the purpose of our reanalysis; the NVSS "all sky" images in total intensity and polarization at 800" resolution are shown in Figure 3.1, dramatically illustrating the larger scale information present in the latter. The processing scheme for these images is discussed in detail below.

3.1.1 Polarization Image Preview

We briefly look at what types of features and artifacts are visible in Figure 3.1 and the additional closer look in Figure 3.2 (center image) at a $\sim 100^o$ region centered around the Perseus arm. First, we see that the polarization images trace the large scale emission of the Galaxy, as seen, e.g., in Reich & Reich (1986) or Haslam et al. (1999). Superposed on the galactic structure are a network of stripes following lines of constant right ascension. These lines represent series of scans from the NVSS survey where the residual

instrumental polarization was slightly higher than average. There are also lines of black 'dots', each of them one approximately one primary beam (34') across, where the residual instrumental polarizations were high enough to require flagging in the NVSS survey (W. Cotton, private communication, 2008). At the highest declinations, the residual instrumental polarization is high at all right ascensions, creating a series of rings around the north celestial pole.

A large number of small sources (at 800" resolution) are also seen in these images. These represent both real polarized sources and those caused by residual instrumental polarizations from the very brightest objects in total intensity. To illustrate the instrumental issues from strong point sources, we consider the case of 3C84; it has an NVSS flux of 22.15 Jy, and an observed polarized flux of 1.9 mJy (0.08%), showing that the residual instrumental polarization is quite low at full resolution. However, larger sources such as Cassiopeia A (∼5' diameter) seen in the center of Figure 3.2 are incompletely sampled in the NVSS, producing sidelobe structure that puts power into the polarization images. Out of Cas A's total flux of ∼2500 Jy, the total polarized flux in Figure 3.2 is ∼45 Jy, or ∼2%, spread over $\sim 1^o$. Although there may be some small real integrated polarization at 1.4 GHz (see Anderson, Keohane & Rudnick , 1995), the 1^o extent shows that the bulk of the contribution here is instrumental. Thus, very strong, extended sources cannot be reliably studied through this NVSS reprocessing. We consider this effect further below in our discussion of emission around 3C31.

By contrast with Cas A, there appears to be little or no effect due to the strong total intensity emission from the Galaxy, e.g., on scales of degrees or larger. This potentially could have been a problem, as Stil et al. (2006) show that the noise in VLA visibility data is related to the value of T_{sys}, which includes contributions both from the sky brightness and spillover radiation from the ground. However, even in the brightest regions of the galactic plane, we do not appear to have preferentially high polarization; the brightest region in Figure 3.2, for example, is in the direction of the Cygnus Arm, and is indicated by a black circle. Within that region, the peak (mean) brightness is ∼35 K (∼7 K) from the Reich & Reich (1986) map, while we observe a mean polarized brightness of ∼20 mK above the background. Instead of being higher in this bright region, the NVSS polarized flux is strongly *anti-correlated* with the total intensity emission, likely due to depolarization from the extensive ionized gas seen over

this same area (Haffner et al. , 2003). Stil & Taylor (2007) also find a major drop in the number of polarized NVSS sources in this area, likely due to depolarization between the two NVSS bands.

A subtle problem with NVSS polarizations has been described by Batttye, Browne & Jackson (2008), largely resulting from clean biases and small (μJy) offsets in Q and U. Both of these create problems far below the noise in the NVSS polarization images, and even further below the residual instrumental polarization artifacts that are prominent in Figures 3.1 and 3.2, and do not affect the current work.

3.2 Map Analysis

The key element of our processing is the convolution to larger angular scales of the *polarized intensity* maps, instead of the typical procedure of pre-convolving Q and U, and then calculating P. Such *pre-convolution* is generally preferred due to its better noise properties, as well as its preservation of the polarization angle ($\chi = 0.5 \times tan^{-1}(Q/U)$) on the convolved scales. Pre-convolution is also equivalent to observations made with a large synthesized beam or single-dish observation. However, since there is a maximum angular scale to which interferometers are sensitive, pre-convolution at that maximum scale or beyond would contain no real signal, only noise.

Once P is calculated from Q and U images at some resolution, further smoothing (which we term *post-convolution* here) can be performed and arbitrarily large structures can be detected. Similarly, if a large total intensity structure were not smooth, but made up of a collection of small-scale features, it would also be detectable beyond the nominal maximum angular scale. This process is diagrammed in Figure 3.3. It shows the production of two maps, P_{800} and P_{800f} , constructed as described above by pre-convolution followed by post-convolution at a resolution of 800".

The rms scatter in P_{800} and P_{800f} varies widely across the sky, and contains contributions from three factors - the random noise from the receivers, the actual polarized signal in each region, and the residual instrumental polarization which is most easily evident in the strong declination stripes visible in Figure 3.1. During the NVSS observations, the focus was on the reliability of the total intensities, and changes in the

instrumental polarization were not closely monitored (B. Cotton, private communication). At times when certain declination strips were being observed, larger than normal instrumental effects would arise, e.g., from phase jumps between the right and left hand receivers on the reference antenna used for polarization calibration. We illustrate more quantitatively in Figure 3.8 how the rms fluctuations in P_{800} vary across the sky at high galactic latitudes. We identify the high rms scatter region associated with the actual signal related to the North Polar Spur, and an adjacent region where the residual instrumental polarization contributions were small. These can also be seen visually in Figure 3.1. In the presence of random noise alone, we could have corrected for the bias in polarized intensity (Wardle & Kronberg , 1974; Simmons & Stewart , 1985). Given the dominance of variable residual instrumental polarization contributions, however, it is not possible to conduct an automated processing scheme for separating the signal/noise/instrumental contributions to the power.Therefore, we look at the noise characteristics for each individual sources of interest, and describe the observed value in P_{800} above the local background and rms to estimate its significance.

To remove some instrumental artifacts (and a first order subtraction of the polarization bias) we will also be making use of a high-pass filtered version of P_{800} , which we label P_{800f} . The high-pass filter consisted of subtracting from each pixel the median of P_{800} over a box 4^o in declination (the size of an individual NVSS image field) by 6' in right ascension.

We estimated the sensitivity to diffuse polarized structures after pre- and post-convolution using a series of simulated polarized signals. The initial construction of the simulated images (Signal+Noise) is shown in Figure 3.4; the processing of these images to measure sensitivities is shown in Figure 3.5. One of the processed (Signal+Noise) images is shown in Figure 3.6. In order to capture all the spatial characteristics of the NVSS images, we used actual images from high galactic latitude fields for both the simulated "signal" and "noise". We constructed the *background "noise"* image by first taking a single pair of $8.5^o \times 8.5^o$ Q and U images from the survey, and at all locations where |Q| and |U| were greater than 2 mJy/beam, replaced these values with zero. This effectively eliminated almost all signals from compact sources in the Q and U images. The remaining large-scale real and instrumental fluctuations in these images thus simulate the actual background against which we are trying to detect signals. The rms

"noise" distribution, which includes point source, galactic and instrumental fluctuations, is shown in Figure 3.7, for all 4^o fields in the NVSS. It can be very roughly described as a Rayleigh distribution with an rms value of ∼6.5 mJy/(800" beam), slightly larger than the expected system noise value of 5.2 mJy/(800" beam) = 0.29 mJy/(45" beam) $\times([800"/45"]^{0.5})$. At the full resolution of the NVSS, the systematic real and instrumental effects contribute little power to the Q and U maps. The systematic contributions become much more important as the images are convolved to lower resolution.

To create our simulated *s*ignal, we took a separate NVSS 1^o field and convolved the Q and U images with an 8' Gaussian, multiplied these images by a constant and added them respectively to the background noise Q and U images. The simulated signal thus consists of a 1^o patch with structures in Q and U on the scale of 8', added to the 8.5^o background (noise) field at the full NVSS resolution of 45".

We then pre-convolved these images to various scales, converted to P (first option in Figure 3.5) and measured the means in the central 1^o region (P_{sig}, including the local noise) and outside the central 1^o (P_{noise}). We also measured the rms fluctuations, P_{rms} in the noise regions. Finally, we calculate

$$Signal : Noise \equiv [P_{sig} - P_{noise}]/P_{rms}.$$

The resulting signal:noise as a function of pre-convolution size is shown in Figure 3.7. The detectability rises dramatically with convolution, as expected, since the "signal" was forced to have a scale of 8'. At larger pre-convolution values, the signal:noise falls as the signal itself starts to be vector-averaged away and diluted.

We also show the behavior of the signal:noise using *post-convolution*. For these experiments, we added the "signal" image (with its 8' scale) to the full resolution Q and U "noise" images, formed P, and then post-convolved the result to various scales (second option in Figure 3.5). Looking again at the signal:noise for various convolutions, we see that the detectability of the signal is less than in the vector-averaged (pre-convolution) case because the signals are not being averaged coherently. At the larger convolution sizes, the signal:noise drops even further, mostly due to the increased noise power on large scales in the NVSS, from both galactic polarization structure and residual instrumental polarization. We note that the above signal detectability experiment is a

single case using an arbitrarily constructed source. The detectability of sources with specific polarization structures would have to be investigated on an individual basis.

It is also possible adopt a hybrid approach and pre-convolve an image to some scale (θ_{pre}), and then post-convolve it to larger scales (θ_{post}). The advantage to this approach is that if an astronomical source has structure in Q and U on scales $\sim \theta_{source}$, then the signal:noise will be enhanced by using $\theta_{pre} \sim \theta_{source}$. This pre-convolution has a second advantage for our survey – it enhances our search for new larger-scale features by enhancing them relative to smaller sources that are more likely to be already known. We therefore adopt, for this initial presentation $\theta_{pre} = 240$" and $\theta_{post} = 800$", and call the polarized intensity P_{800f} . It is important to note that while our P_{800f} maps with $\theta_{post} = 800$" have a resolution very similar to those of single-dish surveys, sources with $\theta_{source} \sim 240$" will be detected by us, but *not* with the single dish. The results presented here are almost entirely qualitative, for a number of reasons. First, they measure only the polarized "power"in Q and U from the poorly sampled low spatial frequencies in the survey up to the pre-convolution scale size. Thus, a source one degree across with uniform Q,U would be invisible, while another source with variations on, e.g., 4 arcminute scales would appear strongly, even if they had the same mean $sqrt(Q^2+U^2)$. The spatially dependent power in Q and U may also depend on the foreground rotation measure, independent of the intrinsic strength of the source. Quantitative information could be derived only by constructing a detailed polarization model of a source and its foreground rotation measure structure, and then propogating that model through simulated observations and processing. We do not attempt this here.

3.3 Results

We begin with a discussion of two large fields in the galactic plane, to illustrate the differences between structures seen in total intensity and/or single-dish polarization maps. We also look at several new diffuse polarized structures, galactic and extragalactic, found through our new processing. A paper identifying a large number of new and often unidentified sources is in preparation.

3.3.1 Cygnus-Perseus region

This region is shown in Figure 3.2 and we have previously discussed some of its instrumental and other features. Here, we point out the filamentary feature extending north for about 40^o from the galactic plane in the Cygnus region ($l_{II}=90^o$) with a less-well defined counterpart to the south. The filament is also present in the total intensity Bonn image at 36' resolution Reich & Reich (1986), especially when filtered to remove the smooth background (using the multi-resolution filtering technique of Rudnick (2002) with a box size of 7^o in longitude by 1^o in latitude). This feature is usually identified as the western portion of *Loop III* (Spoelstra , 1972), but another possibility is suggested in Figure 3.9. The 36' resolution Stokes Q image from Wolleben et al. (2006) is shown here, with the suggestion of a new loop that extends from the Cygnus region, curves up and over the galactic pole, and returns back towards the galactic plane approximately 180^o away. With a nominal center at $l_{II}=0^o$, $b_{II}=20^o$, and a radius of 75^o (M. Wolleben, private communication), it is approximately concentric with Loop I, which Wolleben (2007) has recently modeled in terms of two ∼100 pc radius synchrotron emitting shells in which we are embedded. This new suggested loop needs further study through other ISM tracers, and could potentially revise our understanding of our local environment.

3.3.2 Galactic Center region

A 50^o field near the galactic center (Figure 3.10) further illustrates the similarities and differences between single dish polarization measurements and the NVSS polarization reprocessing at the same wavelength and angular resolution. We pre-convolved the NVSS Q, U images with 240" and post-convolved the P images with 36'. In the NVSS image, the vertical striping are artifacts due to slight differences between residual instrumental polarizations in declination stripes observed at different times. This is also likely responsible for some of the fine-scale mottling apparent along lines, but it is not possible for us to separate these from fine scale polarization structures. We believe that the rest of the structures visible in this NVSS image are "real" in the sense that they reflect the actual signals from the sky. Their interpretation, however, is quite different from those of single dish images, as described below.

As is well known, polarization and total intensity structures are very different, even when they are both from single-dish measurements. The image from the DRAO polarization survey (Wolleben et al. , 2006) shows a bright patch in the upper right, with a smoothly varying position angle (not shown) over scales of degrees. The NVSS is not sensitive to Q and U variations on such large angular scales, and the feature is not visible in our images. High rotation measures (>340 rad/m^2) would also cause a degradation of the NVSS signal compared to the DRAO image. Along the galactic plane, running from upper left to lower right, the DRAO image shows an unresolved narrow bright band bordered by two dark stripes. The dark stripes are beam-depolarized due to a rapid switch in polarization angle across these lines. In the NVSS data, these same patterns in the sky create a different response; a broken thin strip of polarized emission along the plane is seen from the regions where the angle is changing rapidly, creating a detectable interferometer signal in Q and U. However, farther from the plane, the relatively constant polarization angles from the DRAO position angle image (not shown here) lead to a broad dark region in the NVSS image. The numerous depolarization filaments seen elsewhere in the DRAO image are again not seen in the NVSS; rapid changes in polarization angle provide an NVSS signal at high resolution, and there is no depolarization introduced by the post-convolution. An alternative probe of depolarizing regions is presented by Stil & Taylor (2007), who study the polarization of compact sources in the NVSS. They find regions $\sim 10^o$ across that cause a reduction in the number of polarized NVSS sources, due to both intervening H II regions and diffuse galactic structures.

In Figure 3.10, we also point out the bright emission from 3C353 in the NVSS image. This radio galaxy has very strong polarized (Q and U) emission when convolved to the 240" scale, which is then carried forward through the post-convolution to 36'. However, the averaging of Q and U themselves over 36' in the DRAO image makes 3C353 undetectable against the galactic background.

The very luminous HII region M17 is bright in both the DRAO and NVSS images. The NVSS apparent extended polarized flux comes from strong sidelobes, as can be seen in the full resolution images; it is likely that the DRAO polarization is also due to instrumental polarization. W44 is detected strongly in DRAO and weakly in NVSS. The full resolution NVSS polarization image (not shown here) shows a structure which

is largely unrelated to the total intensity structure of W44, so the physical origin of the polarization seen at 36' resolution is unclear.

3.3.3 The Extragalactic Sky

Away from the galactic plane, we get a better view of more compact polarization features in the NVSS, as seen in Figure 3.11. This is an $\sim 44^o \times 17^o$ strip of the sky centered around RA, Dec 11.8h, 34.2^o, with P_{800f} in red. The green image shows the ROSAT All-Sky Survey (RASS , 2000) convolved to 800". The blue image is the total intensity NVSS image, also convolved to 800". Note that at this high galactic latitude ($35^o < b_{II} < 90^o$), and with the additional filtering, very little galactic structure is visible in P_{800f} . A large number of bright compact features are visible, appearing in red (blue) for high (low) fractional polarization. Most of these are also seen in the full resolution NVSS images.

A number of more extended polarization features are also visible in Figure 3.11, many of which are well-known sources. In the southeast, the bright green structure is the X-ray emission from the Coma cluster of galaxies, with an extension to the southwest from an infalling subcluster (Feretti & Newmann , 2006). At the southwest X-ray terminus is a transverse polarized radio structure with brightness ∼20 mJy/800" beam (20 mK) above the background. This is the well-studied "relic" first detected by Jaffe & Rudnick (1979), and then studied in total intensity and polarization, e.g., by Hanisch, Strom & Jaffe (1985); Giovannini, Feretti & Stanghellini (1991). Note the absence of blue, total intensity, emission from this polarized structure; with an angular extent of $\sim 1^o$, the total intensity is not detected in the NVSS survey. Similarly, the diffuse polarized emission from the giant radio galaxies 3C236 and B2 1321+31 is easily visible, while only their more compact features are seen in total intensity in the NVSS.

Among the bright extended polarization structures are several that were previously unknown. Feature A is one of the brightest structures in the high latitude sky (25 - 35 mK); follow-up observations with the Westerbork Synthesis Radio Telescope (**?**) suggest that it is a galactic Faraday system. Such structures have no intrinsic synchrotron emissivity, but appear bright to the interferometer because they produce small-scale variations in Q and U from the galactic background (Wolleben & Reich , 2004). Feature B, and others like it in the image, are examples of single NVSS pointings with high

residual instrumental polarization; they are recognizable by their circular shape and sizes comparable to the primary beam (∼30'). We have not yet found a reliable way to eliminate instrumental problems at the lowest levels seen in Figure 3.11, especially when they span several pointings. In the following, we therefore present examples of new extended polarization features only with high signal:noise, to illustrate the potential power of this NVSS reprocessing technique.

3.3.4 Abell 3744

A network of tailed radio sources is seen in this cluster (Marvel, Shukla & Rhee , 1999), which might be responsible for the bright polarized emission centered on the cluster seen in Figure 3.12. At a redshift of 0.0381, Abell 3744 is listed as a member of supercluster number 180 by Einasto et al. (2001), who group it with Abell 3733, (z=0.0382), and, apparently mistakenly, with the background cluster Abell 3706 at a redshift of ∼0.1 . Abell 3744 is a member of the REFLEX sample (Böhringer et al. , 2004) with a relatively low X-ray luminosity of 1.6×10^{43} erg/s, integrated over 0.1 - 2.4 keV. The X-ray emission is seen only in the region of the cluster center.

To the east, a polarized structure is seen 37' (1.8 Mpc) from the cluster center, with an extent of ∼1.4 Mpc. A slice at constant declination through the peak of polarized emission and through the eastern structure is also shown in Figure 3.12, to demonstrate the signal:noise of these features. The eastern structure has a peak polarized flux 40 mJy/beam above the background, with a background rms of 6 mJy/beam. It has a total polarized flux (P_{800f}) of ∼90 mJy, and no obvious total intensity counterpart. It is important to note that our polarized fluxes are the result of our non-standard processing procedure, and that the true signals measured with an interferometer plus single-dish system could be considerably higher, assuming no additional contributions from a nearby Faraday screen. Assuming our nominal fluxes and a 33% fractional polarization would yield a monochromatic radio luminosity of 10^{24} W/Hz at 1.4 GHz. If this is a peripheral relic, or gischt (Kempner et al. , 2004), both its radio and associated X-ray cluster luminosities are significantly lower than those of most relic systems (e.g., Giovannini et al., 1999). Only one other cluster, Abell 548b, which is part of a very complex optical and X-ray system (Davis et al. , 1995), has similarly low luminosities. The Abell 3744 relic would also be considerably further from the cluster core than is

typically seen. Confirming and more detailed polarization observations of this system would also be most useful.

3.3.5 3C 31

3C31 is a very well-studied wide-angle tailed radio galaxy (Fanaroff & Riley , 1974) with a total extent of >40' (∼850 kpc at z=0.0169 with H_o= 70 km/s/Mpc, Klein & Wielebinski , 1979). In our polarization image, Figure 3.13, we find emission extending $\sim 1.2^o$ to the southwest, where it partially merges with polarized emission from an unrelated background source. To the southeast, there is polarized emission bridging to 3C34, an unrelated source in a z=0.69 cluster (McCarthy , 1998). Formally, the statistical signifance of the polarized emission is high. Towards the southwest (southeast), the polarized brightness is ∼15 (25) mJy/800" beam above the background, with a background rms of 4 mJy/800" beam. However, there is an additional source of contaminating polarized emission in the neighborhood of strong, very extended polarized sources such as 3C31. These are sidelobe structures from the poorly sampled short baselines, but would appear as true positive-definite signals in our processing. To assess the importance of this effect near 3C31, we constructed an equivalent 'I_{800}" image by processing the total intensity image in an identical way to P_{800} , substituting I for both Q and U. This created excess power in the vicinity of 3C31, as expected. However, the ratio of the brightness in the southwest (southeast) polarized feature to the peak brightness of 3C31 itself is 0.1 (0.17) in P_{800} , whereas the brightness ratios for the same locations in I_{800} are ≤0.01. We therefore conclude that poorly sampled sidelobes from the polarized emission in 3C31 is not responsible for the newly detected features.

It is not clear whether this diffuse emission is associated with 3C31 or 3C34. The host galaxy of 3C31 is NGC 383, the brightest of a rich group of galaxies (Burbidge & Burbidge , 1961), many of which are seen in the area of the polarized emission to the SE of the source (Figure 3.5). These are all part of a filament of galaxies at this redshift (Miller et al. , 2002), which extends through the SW polarized extension over 9^o to the NE to cluster Abell 262 (Moss & Dickens , 1977). In the λ11.1 cm single-dish images of Klein & Wielebinski (1979), a 10' extension is seen to the southwest. The low resolution 102 MHz images of Artyukh, Ogannisyan & Tyul'bashev (1994) also show extended emission to the southwest, with a size ≤50', the extent of their primary beam.

There is possible contamination from the southwest background source. Note that in their Figure 1, 3C31 is the northern component of the apparent double structure; the southern component is 3C34.

Assuming that the southwest extension is associated with 3C31, it would have an extent of ∼1.5 Mpc. There is some possibility that the observed polarization structure results from distant sidelobes of 3C31, although processing the total intensity NVSS images in the same way as Q and U (i.e., forcing them to be positive and then post-convolving), did not show significant sidelobe contributions. Assuming the polarization structure is real, the λ11.1 cm results cited above also suggest that there has been an outflow to the southwest from 3C 31. Lacking bright jet features, this structure would likely be a remnant of past activity, perhaps now being energized by large scale group processes. Indications of the dynamical state of the group include the offset of NGC 383 from the centroid of the X-ray emission and significant X-ray structure towards the southwest (Kormossa & Böhringer , 1999), which is detected out to the virial radius at ∼700 kpc.

3.3.6 CTA1

This well-known supernova remnant has a filled X-ray structure and a radio shell which is not visible in the NVSS total intensity images. It has been mapped at 1' in polarization at 1.4 GHz using the DRAO telescope (Pineault et al. , 1997). All of the major features seen in the DRAO image are reproduced in our NVSS reconstruction at 800" resolution (Figure 3.15). In addition, we find one diffuse bright patch at 00h10m, 72^o that is not seen in the DRAO map. The diffuse nature of this patch is established by the lack of smaller-scaled polarized features in the full resolution Q, U images (at a level of Q, U $<$ 3 mJy/45" beam). Its peak brightness is 30 mJy/800" beam above the local mean, with a background rms of ∼5 mJy/800" beam. If it were completely smooth, the polarized brightness would be only 0.2 mJy/1' beam, compared to the DRAO rms value of 0.3 mJy/1' beam, so it is reasonable that it had not been previously detected.

The bright patch is on the border of what Pineault et al. (1997) call the "reverse shell" region, where the curvature of the radio structure is inverted. Their explanation for the shape of this region is that the shock has encountered and encircled a dense cloud. The new polarized patch may help define the borders of this cloud encounter,

but the lack of bright, narrow polarized or total intensity emission, as pointed out by Pineault et al. (1997), is still a problem for this explanation.

3.4 Discussion

Polarized intensity is not a well-defined quantity when there is more than one polarized component along the same line of sight, creating both challenges and opportunities. Although there are heroic attempts to separate multiple components if they are separated in rotation measure space (Brentjens & de Bruyn , 2005; Schnitzeler, Katgert & de Bruyn , 2007), in general, observed polarized intensities depend on a complicated combination of observing frequency, resolution, and the spatial frequencies represented in the image. This complication also allows a variety of processing schemes to be carried out on Stokes parameter images, which can result in new structures being identified.

Our reprocessing of the NVSS survey in Stokes Q and U explores a region of observing frequency/resolution/spatial frequency that has not been previously studied. We therefore have been able to identify many new features, as well as recover structures that are invisible in the total intensity NVSS but seen at other telescopes. One common feature of the extended emission features we detect is that they are of low surface brightness. P_{800f} images free of galactic emission have rms fluctuations $\sim$2 mJy/800" beam (2 mK). A 5σ detection would therefore correspond to $\sim$10 mJy/800" beam or $\sim$30 mJy/800" beam in total intensity, assuming a fractional polarization of $\frac{1}{3}$. By contrast, a single dish working at the same frequency and angular resolution, would have a 5σ confusion limit of $\sim$125 mJy (e.g., Condon & Broderick , 1985). Under favorable conditions of high fractional polarization and Q,U variations on scales <15', the reprocessed NVSS can then be much more sensitive to diffuse structures than any single-dish survey.

All-sky surveys of diffuse polarization could thus be a powerful way to probe low density extragalactic regions. Assuming an optimum sensitivity of 30mJy/800" beam (total intensity), the equivalent minimum energy magnetic field for a detected synchrotron structure will have values $\sim 0.2\mu$G. This corresponds to pressures of $\sim 10^{-14.5}\ \frac{erg}{cm^3}$, in the regime of the WHIM (Kang et al. , 2005). Radio observations at these low brightness levels could then serve to illuminate the diffuse baryon component of large scale

structure, where 30-50% of the baryons are likely located, but are exceedingly difficult to detect through their thermal emission. Simulations by Miniati (2004) and Pfrommer et al. (2006), e. g., show that such radio emission is expected, driven by the magnetic field amplification and relativistic particle acceleration at shocks on the borders and in the interior of filaments.

Much more sensitive polarization measurements, with significantly reduced instrumental problems, will soon be available on the EVLA [1], and a new generation of wide-field, low frequency instruments such as LOFAR [2] and the MWA [3] will allow us to probe much deeper into the WHIM regime over large areas of the sky. Combinations of single dish and interferometer observations may also allow such features to be seen in total intensity for individual regions where the large investment of observation and analysis time can be justified.

3.4.1 CMB polarized foregrounds

It is unlikely that features found through our NVSS reprocessing will affect upcoming CMB polarization experiments. We have identified new features on scales down to θ_{pre} = 240". For the new synchrotron sources, forthcoming CMB polarization experiments that work at these resolutions or smaller, such as Planck or EBEX (Oxley et al., 2004), [4] will have sufficient frequency coverage to model the foreground contamination from galactic or extra-galactic synchrotron sources internally. We also detect "pseudo-sources" due to Faraday screens in our galaxy. However, direct Faraday rotation of the CMB signal from these regions is negligible at $\nu > 100$GHz ($\Delta\theta \approx 0.5\,$deg for a rotation measure of RM=1000 rad/m^2). At the same time, the Faraday screen features could indicate the presence of undetected HII regions (Sun et al., 2007). The bremsstrahlung emission from HII regions can be polarized at the 10% level due to Thomson scattering at the edges of the clouds Keating et al. (1998), but the polarized brightness should be at least an order of magnitude less than that of synchrotron emission at frequencies above 10 GHz Bennett et al. (1992). Such signals are typically not modeled as a polarized foreground component in the WMAP analysis (Page et al., 2007; Gold et al.

[1] http://www.aoc.nrao.edu/evla
[2] http://www.lofar.org
[3] http://www.haystack.mit.edu/ast/arrays/mwa
[4] See http://lambda.gsfc.nasa.gov for a complete list of CMB polarization experiments.

, 2008).

3.5 Conclusions

A reprocessing of the NVSS polarization images has allowed the recovery of diffuse structures on large angular scales. The details of the processing allow one to tailor the sensitivity to particular angular scales of interest. At present, residual instrumental polarization variations across the sky are a key limiting factor. A variety of new galactic and extragalactic sources have already been identified, with a more comprehensive census underway. While a better recovery of diffuse polarization structures is possible, e.g., by combining single dish and interferometer measurements, the next generation of radio telescopes such as LOFAR, the MWA and EVLA will also be able to exploit the processing technique introduced here to provide probes, e.g., of the relativistic plasmas associated with the elusive WHIM.

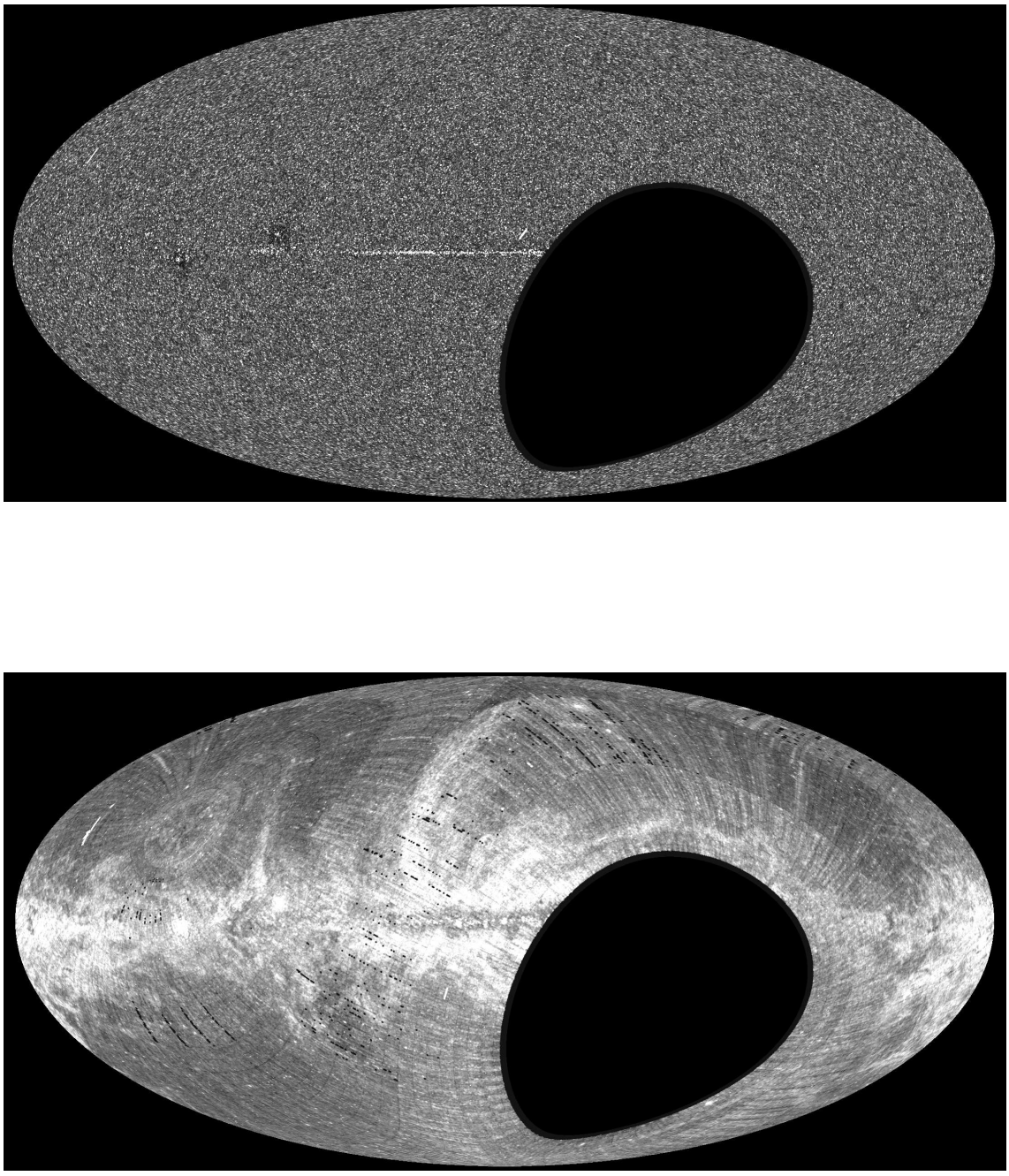

Figure 3.1: All sky AITOFF projections in galactic coordinates of the NVSS, at a resolution of 800". The top image shows the total intensity, with polarized intensity on the bottom. The obvious striping in the polarized intensity, mostly along lines of declination, are due to variations in the residual instrumental polarization during the survey. Occasional small black regions is where the residual instrumental polarization was especially high, and the polarization data were flagged for that individual pointing.

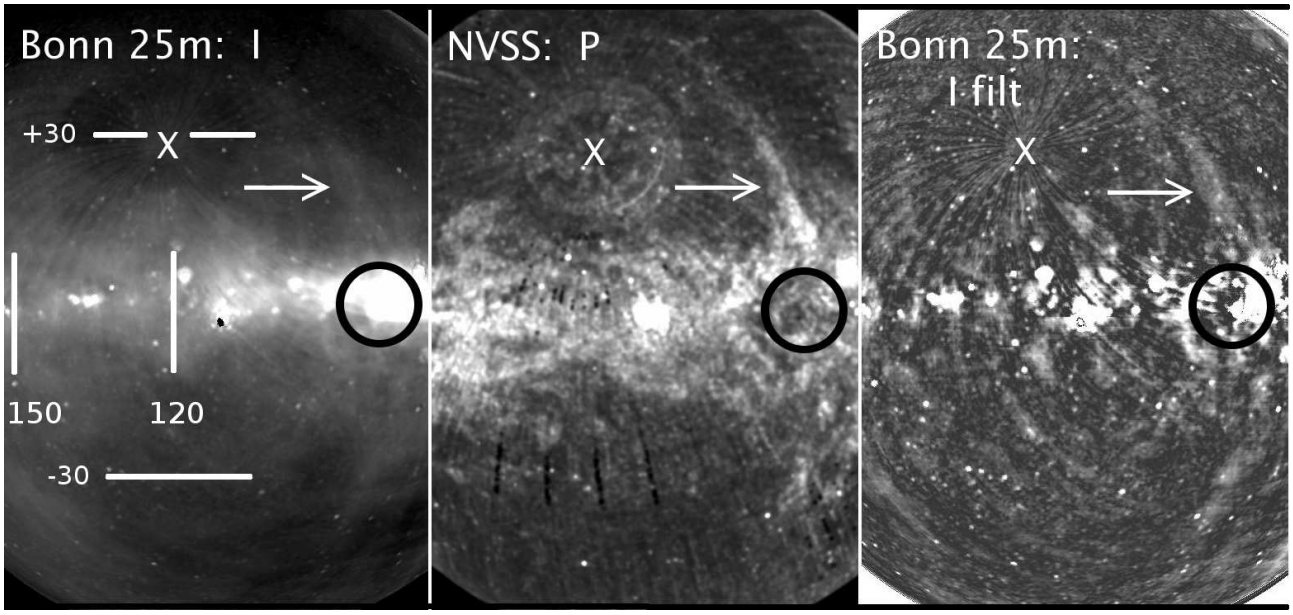

Figure 3.2: Total and polarized intensity around the Perseus-Cygnus region of the galactic plane. Galactic coordinates are indicated on the left image. "X" marks the position of the celestial pole; circles around the pole visible in the middle image show lines of constant declination. Left: 21 cm total intensity from Bonn 25m survey Reich & Reich (1986), 36' resolution. Center: Polarized intensity from NVSS at 800" resolution, with no filtering. Right: Filtered version of map on left, as described in text. The black circle marks the Cygnus arm at l_{II}=90^o; the arrow indicates the base of what is normally called "Loop III" and is discussed further in the text and in Figure 3.9.

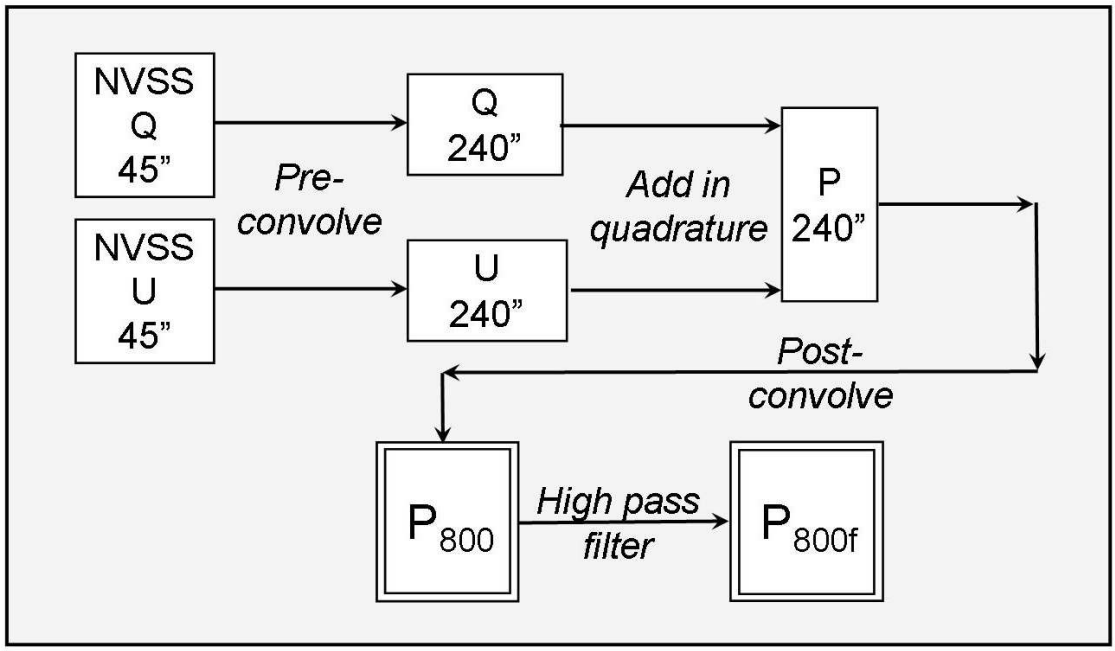

Figure 3.3: Flow chart for construction of polarization images P_{800} and P_{800f}.

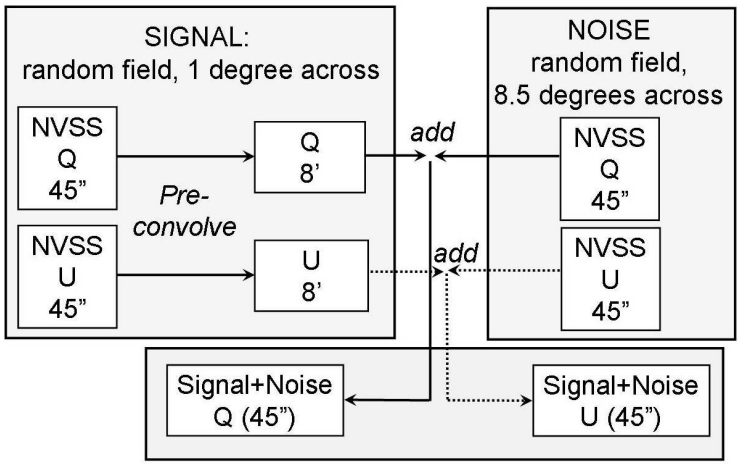

Figure 3.4: Flow chart for construction of simulated images (signal+noise) for sensitivity experiments. The NVSS Q and U images were first clipped to remove the effects of strong, compact polarized sources.

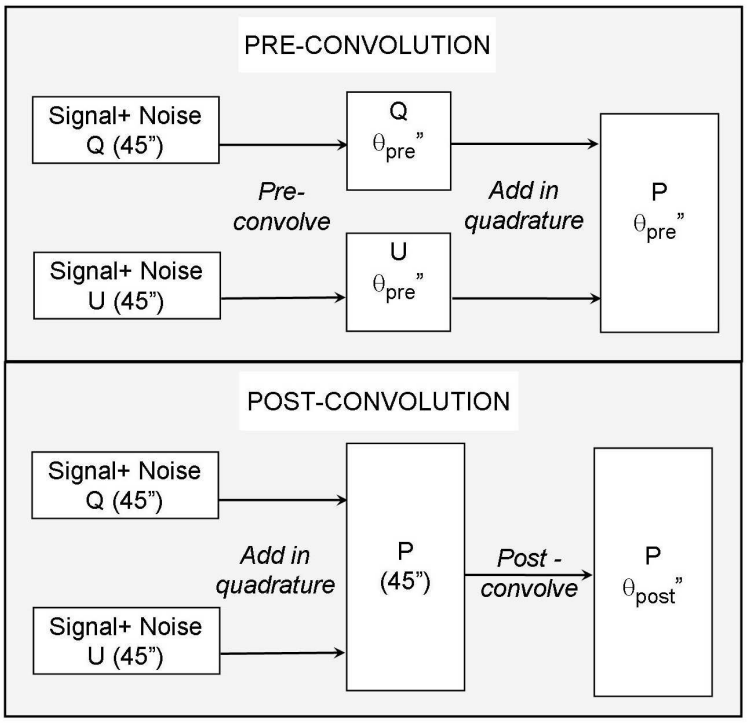

Figure 3.5: Flow chart for two options of processing (Signal+Noise) images for sensitivity calculations.

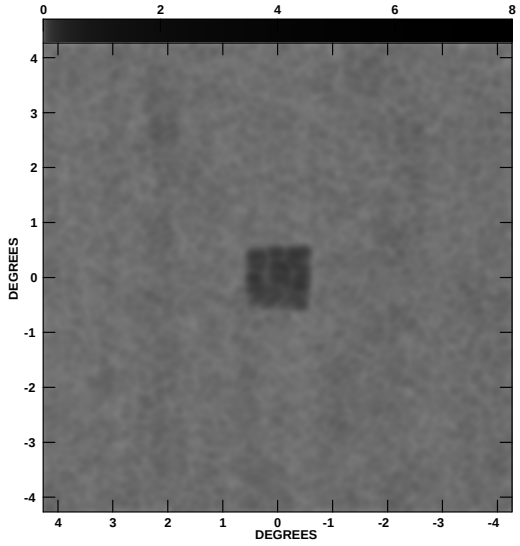

Figure 3.6: Example of simulated polarization data used to calculate sensitivity. The central 1 square degree contains the simulated signal, a random pattern of polarized flux with a characteristic scale of 8'. In this particular example, the image was "pre-convolved" by 4' and "post-convolved" by 8'.

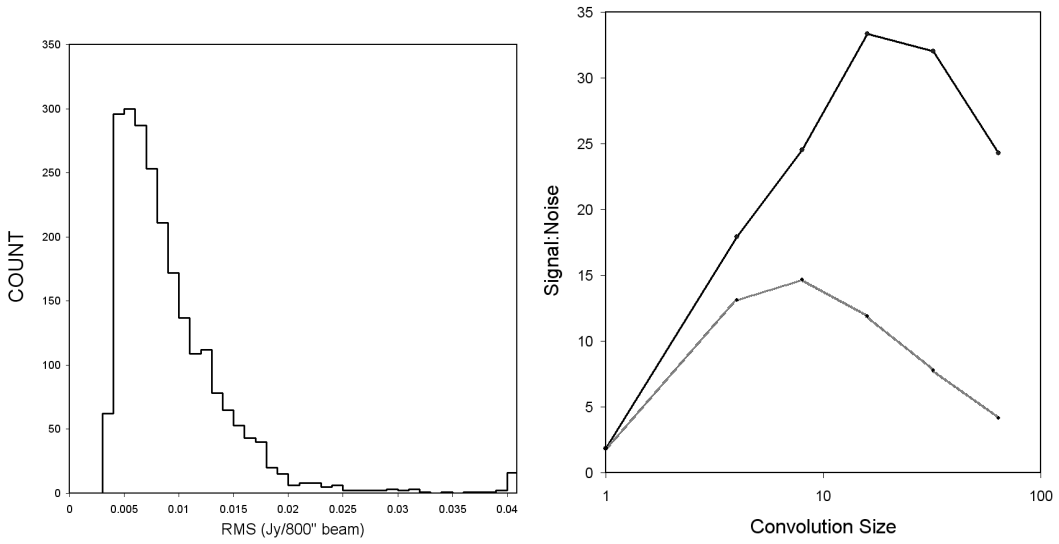

Figure 3.7: Left: Histograms of the rms noise in each 4^o field in the NVSS. Right: signal:noise from simulated polarization measurements, as described in the text. The black line indicates "pre-convolution" of the Q and U images; the grey (lower) line indicates "post-convolution" of the P image.

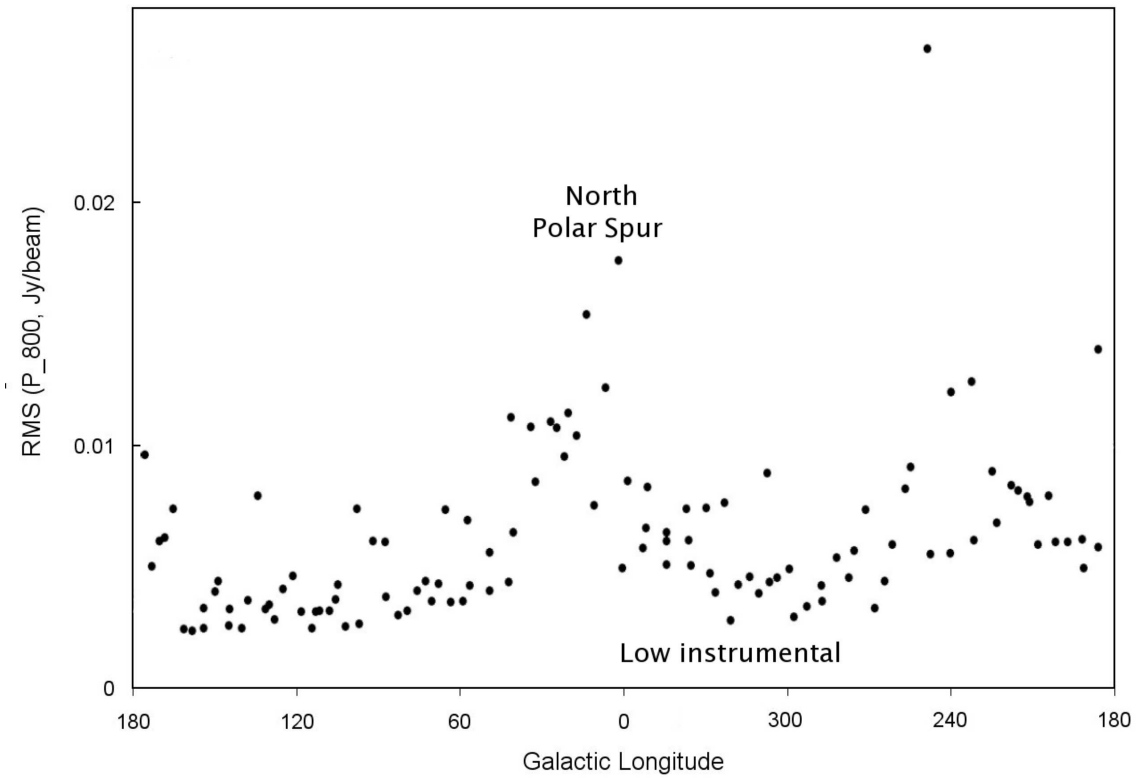

Figure 3.8: RMS scatter in P_{800} in strip from $53^o < \mathrm{b}_{II} < 67^o$ as a function of galactic longitude. Inidividual spikes and the large scatter are due to variations in residual instrumental polarization. A region of low instrumental effects is indicated, along with the increased rms power due to the North Polar Spur.

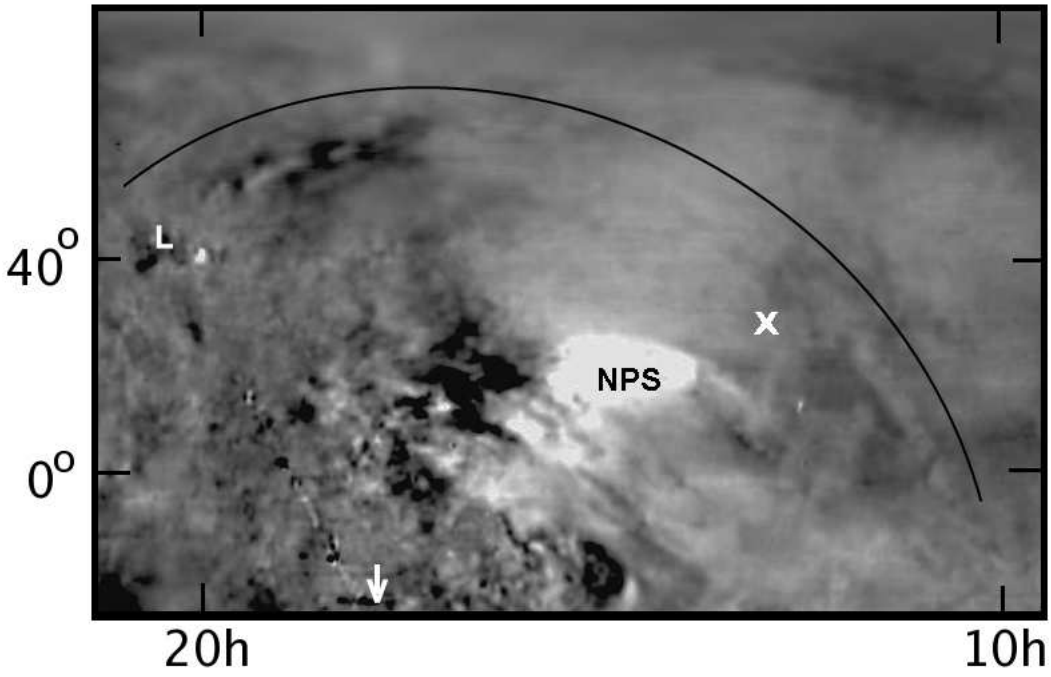

Figure 3.9: DRAO Stokes Q image (Wolleben et al. , 2006) in celestial coordinates, centered at RA,, Dec. $\sim$ 15h, 30^o , and approximately 150 ^{o} in RA by 110^o in Dec. "L" marks the base in the galactic plane of the suggested new loop, at l_{II}=82^o. while the arrow shows the position of the galactic center, just below the edge of the image, so the galactic plane runs between these two. X marks the galactic pole, and NPS denotes the North Polar Spur. A curved line is drawn outside of the possible new loop.

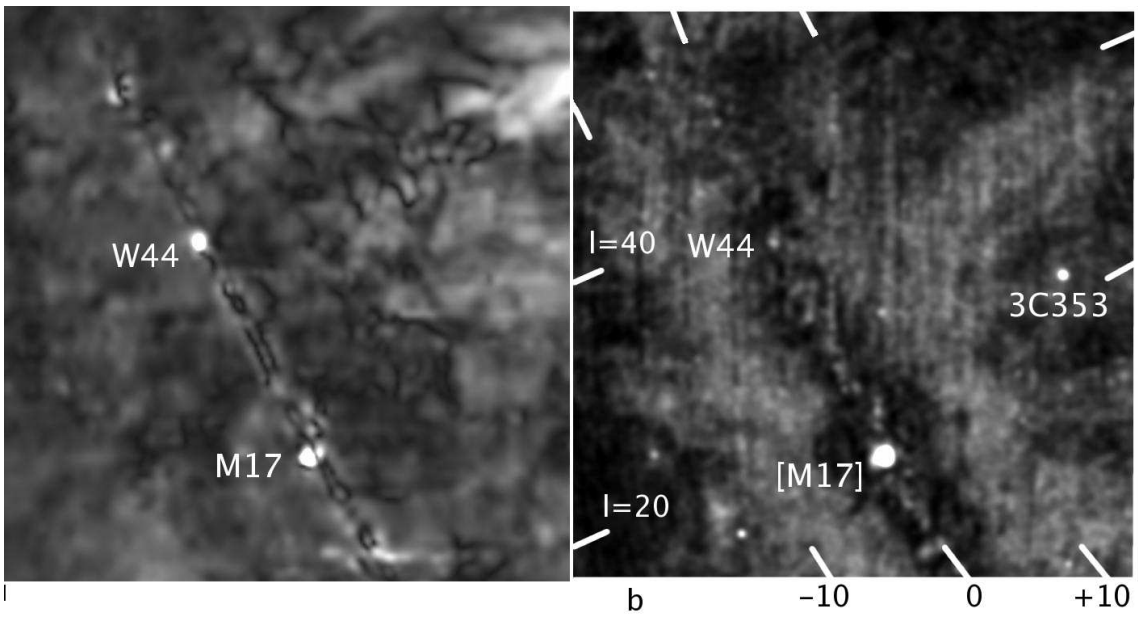

Figure 3.10: Left: Polarized intensity from DRAO survey (Wolleben et al. , 2006). Right: Polarized intensity from NVSS. Both images have a resolution of 36'. The field is centered at l,b = 26.5^o, -1.1^o and is 50 degrees in width.

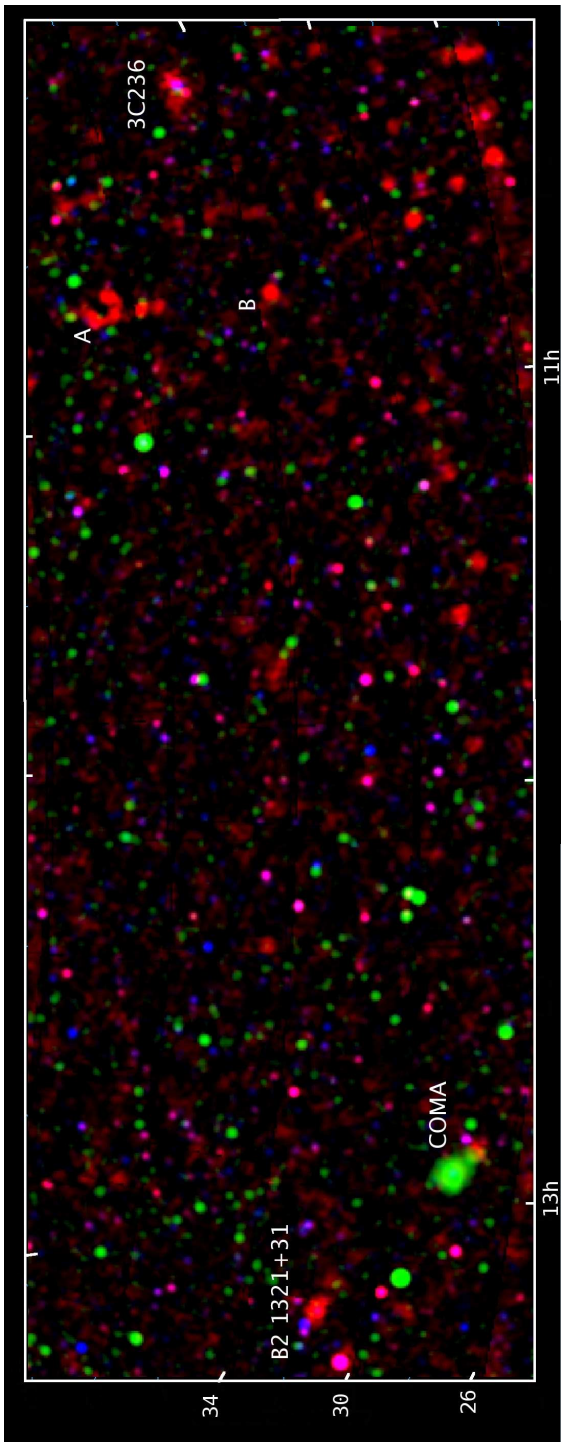

Figure 3.11: Image of approximately $44^o \times 17^o$ strip in celestial coordinates, centered around 11.8h,34.2dm Red is P_{800f} , green shows the broadband X-ray emission from ROSAT, convolved to 800", and blue is the total intensity emission from NVSS, convolved to 800".

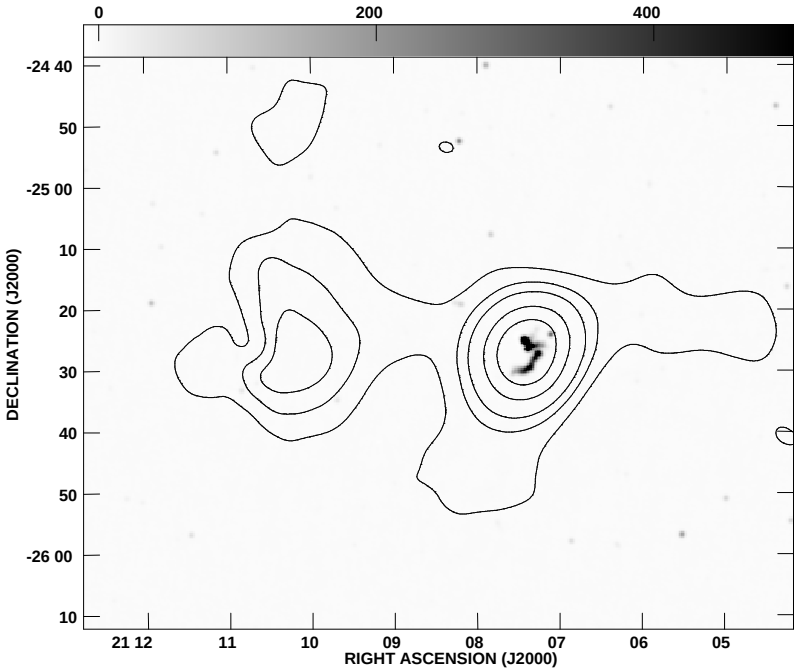

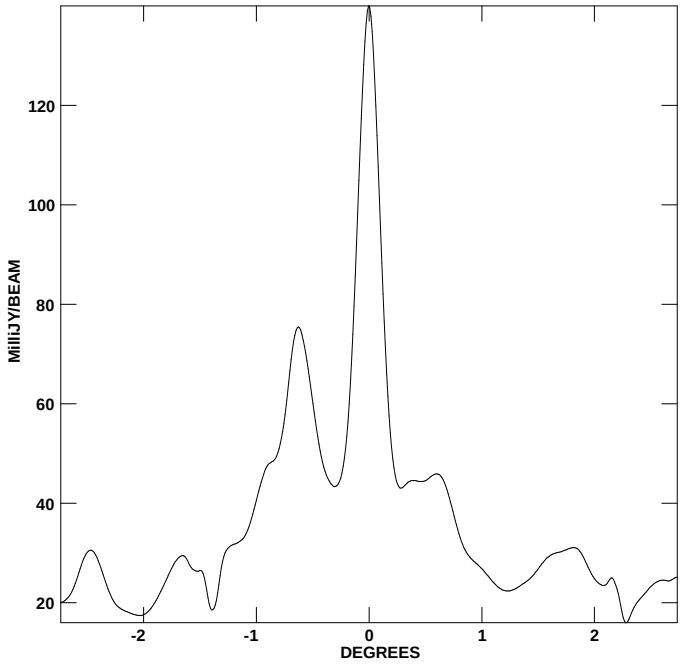

Figure 3.12: Abell 3744, contours and slice of NVSS polarized intensity at resolution of 800". The top image is overlaid by the NVSS total intensity at 45" resolution. Contour levels are at 0.01 × (4, 5, 6, 8, 10) Jy/beam. The total field is 95" in declination by 115" in right ascension. The slice is taken in right ascension through the peak and extends over 5^o to show the signal:noise of the detected features.

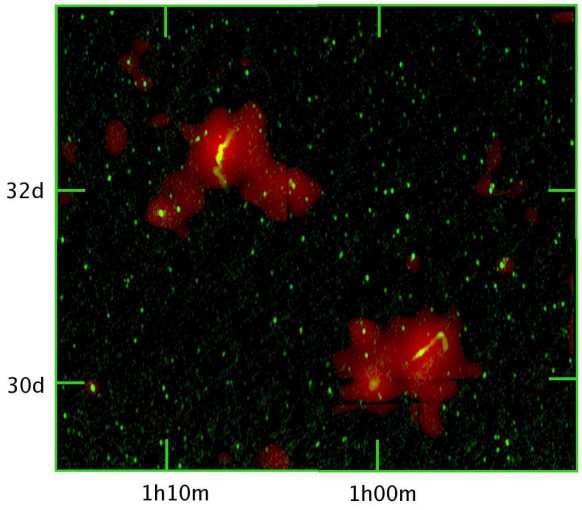

Figure 3.13: 5.3^o field with 3C31 (upper left) and NGC 315 (lower right). P_{800f} is in red. The brightness of the southwest extension of 3C31, ignoring the region of the background double, is ∼12 mJy/800" beam. The vertical and horizontal lines indicate slight differences in background removal from the original 4^o NVSS fields. The green image is the full resolution WENSS survey image at 330 MHz.

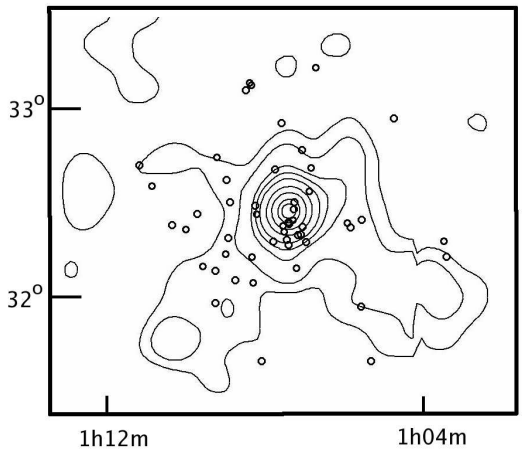

Figure 3.14: Contours of polarized emission (P_{800f}) in a 2^o field around 3C31, at levels of (6, 13, 28, 38, 51, 76, 100, 126 and 140) mJy/800" beam. Small circles indicate the positions of galaxies at redshifts of 0.014 to 0.020 from the 2MASS survey (Huchra et al. , 2005).

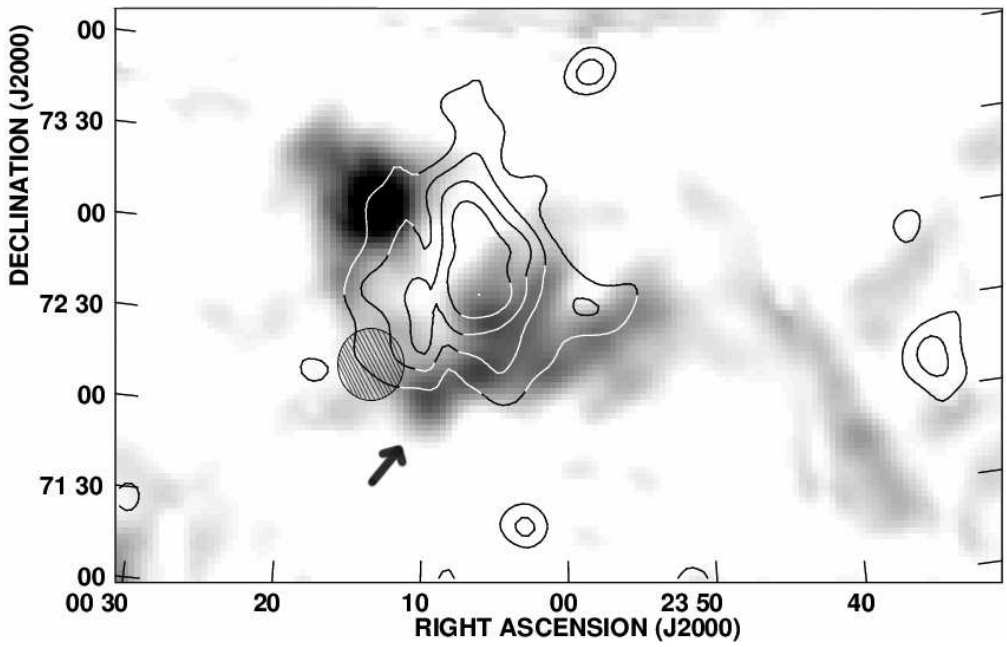

Figure 3.15: CTA 1. Greyscale is P_{800f} , with a peak brightness of 45 mJy/800" beam. Contours are broadband X-rays from ROSAT, convolved to 800". The hatched circle represents the cloud described by Pineault et al. (1997), and the arrow indicates the new polarized patch not visible in the DRAO higher resolution image.

Chapter 4

Cross-Correlation of Diffuse Synchrotron and Large-Scale Structures

A slightly modified version of the chapter has been submitted to the Monthly Notices of the Royal Astronomical Society: Brown, S., Farnsworth, D., & Rudnick, L. 2009

4.1 Introduction

In the current cosmological paradigm, ≈95% of the mass/energy density of the universe is composed of dark energy and dark matter, both of which have yet to be directly detected. The remaining 5% are ordinary baryons, which at redshifts of z > 2 are fully accounted for based on Lyα forest observations of the photoionised intergalactic medium (IGM) and ordinary galaxies (e.g. Rauche et al. 1997; Weinberg et al. 1997; Schaye 2001). In the current epoch though, roughly half of these baryons are missing. Simulations suggest that the collapsing diffuse IGM was shock-heated and now resides in filaments as T$\sim 10^5$ - 10^7 K WHIM, where it is practically invisible at most wavelengths (Cen & Ostriker 1999, 2006; Davé et al. 2001). A few tentative absorption detections of the coolest WHIM components using OVII and OVIII have been reported, but they give no information on the spatial distribution. However, shocks from infall into and along the filamentary structures between clusters are now widely expected to generate

relativistic plasmas which track the distribution of the WHIM (Keshet et al. 2004; Pfrommer et al. 2006; Ryu et al. 2008; Skillman et al. 2008); indeed, accretion shocks are seen as polarized radio sources (the "peripheral relics") at the edges of the dense X-ray gas in clusters. This radio emission also has the potential for probing into the lower density regions further from cluster cores. When such features are detected, they can be used to set limits on the (invisible) pressure of the thermal gas, delineate shock structures, and illuminate large scale magnetic fields. The next generation of low frequency radio telescopes (e.g., LOFAR, MWA, LWA, and eventually SKA), as well as current deep continuum surveys (e.g., GALFACTS[1] at Arecibo), have the potential to map this steep-spectrum, "cosmic-web" of synchrotron emission (Battaglia et al. 2009).

However, there are two major problems that will challenge future radio surveys in their efforts to detect this emission. 1) Disentangling the extragalactic signal from diffuse Galactic emission that has a similar surface brightness and angular scale; 2) Determining the redshift of the diffuse extragalactic signal (e.g., Brown & Rudnick 2009).

One possible solution is to cross-correlate large field-of-view synchrotron maps with optical/IR tracers of large-scale structure (LSS; Keshet et al. 2004). The cross-correlation function (CCF) has long been used as means of detecting faint, often below the image sensitivity, emission in CMB maps such as the SZ and late ISW effects (e.g., Boughn & Crittenden 2004) Attempts to detect the WHIM with cross-correlation using the SZ effect has been tried with WMAP and 2MASS data (e.g., Hernandez-Monteagudo et al. 2004; Hansen et al. 2005; Cao et al. 2006), without success. In this paper we outline the first attempt to detect a correlation between synchrotron radio emission and large-scale structure, and demonstrate the power of cross-correlation by detecting simulated emission added into the synchrotron images. In this paper, we assume $H_o = 70$, $\Omega_\Lambda = 0.7$, $\Omega_M = 0.3$.

[1] http://www.ucalgary.ca/ras/GALFACTS/

4.2 Cross-Correlation

4.2.1 Images

Synchrotron emission in filamentary large-scale structure (LSS) is predicted to be on the order of 1-2 Mpc, similar to some observed radio relics around rich X-ray clusters (see Giovannini & Feretti 2004 for a review). Therefore we used the Stockert 25m Bonn survey (Reich, 1982; Reich & Reich, 1986) as a synchrotron tracer. Bonn is a 1.4 GHz survey with $\sim 36'$ resolution and an effective sensitivity of 50 mK (3×rms noise); the fact that it is a low-resolution, single dish survey means that it is more sensitive to large-scale diffuse emission, and the relative contribution from point-sources is reduced significantly. We chose a target field, $34^\circ \times 34^\circ$ centered on 16h00m00s +35d00m00s, where the diffuse Galactic emission was smooth and relatively well behaved. Figure 4.1 shows the 1.4 GHz radio map, with 600 pixels of $3.4'$ each. Most of the signal in the image is diffuse Galactic emission, and the rest is dominated by systematic striping and unresolved radio galaxies.

We filtered out the diffuse Galactic synchrotron emission using the multi-scale filtering technique of Rudnick (2002). The choice of filtering size is a compromise between the need to remove as much as possible of the Galactic emission while preserving the filamentary component. For this initial experiment, we filtered out all emission larger than $180'$, or 5 times the size of the Bonn beam. Further experimentation to optimize this will be important for future studies. Figure 4.1 shows the target field after filtering.

For a tracer of LSS in our target field, we used the 2MASS survey (Skrutskie et al. 2006) to create maps of the surface density of galaxies (number of galaxies/pixel) for 2 redshift slices ($0.03 < z < 0.04$ and $0.06 < z < 0.07$). We then convolved the 2MASS maps to $36'$, the resolution of the Bonn survey. Figure 4.1 shows the 2MASS images. The large concentration of galaxies in the $0.03 < z < 0.04$ image corresponds to the two clusters Abell 2199 and 2197 at redshifts of 0.0301 0.0308, respectively. The $0.06 < z < 0.07$ image contains Abell clusters 2122, 2124, 2079, and 2065 at redshifts of 0.0661, 0.0656, 0.0670, and 0.0726, respectively.

4.2.2 Cross-Correlation

We computed the cross-correlation function (CCF) for the filtered and unfiltered radio images with both redshift slices. The CCF is defined by $CCF\,(xshift, yshift) = \frac{1}{n}\sum(R_{i,j}-\bar{R})(G_{i,j}-\bar{G})$, where n is a normalization given by $\sqrt{\sum(R_{i,j}-\bar{R})^2\sum(G_{i,j}-\bar{G})^2}$, R is the radio map, and G is the convolved 2MASS surface density of galaxies shifted in relation to R by $xshift$ and $yshift$ pixels. Figure 4.2 shows the CCF, with the shift in units of Mpc at the redshift of the 2MASS images, for both redshift slices cross-correlated with the Bonn images. It is obvious that the large-scale gradient in the Galactic synchrotron emission is dominating the CCF in the unfiltered images. The CCF for the filtered images is not significantly peaked at zero shift, i.e., the filtered synchrotron and 2MASS surface densities are not significantly correlated.

When cross-correlating all-sky images, such as done with the CMB, the significance of a given CC value is assessed by using simulated CMB signals (e.g., McEwen et al. 2007). In the initial experiments peformed here, we are using only a $34^\circ \times 34^\circ$ field, and can therefore use other fields from the Bonn survey as controls. Given the systematic striping in the Bonn survey, and the fact that diffuse Galactic emission is not a simple Gaussian field like the CMB, this initial study sampled the cross-correlation function using fields from the Bonn survey at distances (θ) ranging from 27° to 127° from our target field. We split the survey up into $34^\circ \times 34^\circ$ images with 600 pixels on a side and TAN projection (Greisen & Calabretta 2002; Calabretta & Greisen 2002), and excised all the fields with strong Galactic plane emission. Fields with artifacts from gridding the survey maps together were also removed, leaving 24 total images. Assuming that none of the 24 maps should be correlated with the surface density of galaxies in a different, well separated region of the sky, the distribution of these CC values (histograms are shown in Fig. 4.3) represents the noise in this procedure. The CCF($\theta = 0$) value for the target field is marked with a red line; in all cases the 2MASS-Bonn correlation for the target field is again not significant. Note that the scatter is dramatically lower in the filtered image's cross-correlation.

One can think about this procedure as constructing a sparsely sampled CCF(θ) over the whole sky. Figure 4.4 shows plots of the CCF as sampled by the 24 distant fields as a function of angular distance from the target field (which here is CCF($\theta = 0$)). These again show that the target CC value is not significantly above the values for the

well-separated control fields.

4.2.3 Detection Thresholds

In order to assess our sensitivity to diffuse synchrotron signals associated with large-scale structure, we next injected a simulated filamentary, LSS radio signal into the Bonn images before cross-correlation. As a simple model, we assumed the synchrotron LSS signal is linearly proportional to the number-density of galaxies. We added the signal into the target field radio image incrementally until the CC experiment yielded a 3σ result, the detection threshold, where σ is defined as the rms of the sparsely sampled CC function. We did this for both the filtered and unfiltered Bonn images and both redshifts. We quote the detection threshold in Table 4.1 as the number of mJy per 2MASS galaxy injected into the radio image, prior to convolution. The peak and typical filament values of the injected signal in mK are also listed in Table 4.1. In the case of the filtered Bonn image correlated with both redshifts, the signal needed to cause a 3σ detection is *below* the $3\times$rms sensitivity level of the Bonn survey.

We also looked briefly at the issue of isolating the CC contribution of the dense cluster-like concentrations in 2MASS from the contribution from more diffuse filamentary regions. To explore this, we repeated the signal injection experiment with the z=0.03-0.04 image and the filtered Bonn image, except that this time we only added in signal that was below $5\sigma_{rms}$ of the 2MASS image. In this case the detection threshold rises significantly, to peak and filament values of 19 mK and 11 mK, respectively. We note that these values are still well below the sensitivity of the Bonn survey for any given location.

4.3 Physical Expectations/Interpretations

How do these simulated radio signals compare to theoretical expectations for filamentary synchrotron emission? Resent cosmological simulations (Ryu et al 2008) demonstrated that strong turbulence driven by structure shocks associated with the WHIM can generate current epoch (volume averaged) filament magnetic fields of the order of 0.01 μG. However, the synchrotron emissivity scales as B^2, and under the assumption that the total number of relativistic particles will scale with local mass density, the mass weighted

rms of B is appropriate. This yields a considerably higher characteristic value of 0.2μG in filaments (Ryu, private communication, 2008). In order to convert this magnetic field estimate to a characteristic synchrotron brightness, we need to make some assumption about the cosmic ray density. We adopt the condition where the energy density in relativistic particles (protons and electrons, equally) is the same as the magnetic field energy density, (equipartition). This results in a synchrotron brightness at 1.4 GHz of 1 mK in filaments. This predicted value is much weaker than the $\leq$50mK background brightness temperature predicted by Keshet et al. (2004). We note that there is considerable uncertainty regarding the actual magnetic strength in filaments. Donnert et al. (2008), e.g., find only $\sim$0.005 μG.

	Unfilt .03-.04 (mK)	Unfilt .06-.07 (mK)	Filt .03-.04[a] (mK)	Filt .06-.07 (mK)
Peak	694	570	7(19)	49
Filament	100	80	1(11)	7
mJy/Gal[b]	205	135	2	12
Filament B_{eq} (μG)	0.74	0.70	0.20	0.35

Table 4.1: CROSS-CORRELATION DETECTION THRESHOLDS: a: Bracketed values are thresholds when adding filaments only (see text). b: The flux required per galaxy to reach the detection threshold.

Table 4.1 lists the equipartition magnetic fields corresponding to our detection thresholds. Our lowest thresholds approach those expected in the Ryu et al. (2008) simulations. With more sensitive future 1.4 GHz surveys such as GALFACTS, we will be able to robustly test those expectations, although it is not yet clear whether we can reach 0.005 μG (Donnert et al. 2008).

To put our CC brightness limits in context, we note that even bright radio halos such as in the Coma cluster (with $\sim$20$'$ FWHM, e.g., Kim et al. 1989) are very difficult to detect individually. The Coma halo in the Bonn survey is a barely detected 150 mK bump on the $\sim$3.3 K CMB + Galactic local background, mostly due to the fact that the brightness is diluted by the 36$'$ beam. Typical halos have brightnesses of $\approx$700 mK, brighter than the *intrinsic* 350-400 mK brightness of the Coma cluster halo. As discussed in Rudnick & Lemmerman (2009), visual searches for halos are biased towards

higher brightnesses at higher redshifts.

The fact that the detection thresholds (Table 4.1) are below the predicted values of Ryu et al. (2007) and Keshet et al. (2004) do not rule out these models. Important effects such as the filling factor of the synchrotron emission and the linear nature of the LSS formation shocks are not captured by our simple model. However, analysis of LSS formation simulations that include synchrotron emission can be used in the future to design the optimum CC procedure for detecting this emission, and would guide the way toward the correct interpretation of future cross-correlation results. The ultimate goal is to provide limits on magnetic field strengths and pressure of the relativistic plasma in filaments, and therefore test origin theories for cosmic magnetism and probe the missing baryons in the WHIM.

4.4 Summary

We have explored for the first time the method of cross-correlation of diffuse radio emission and tracers of LSS in order to detect the synchrotron radiation associated with the diffuse baryons in the WHIM. Filtering out the large-scale Galactic emission is critical for reducing the CC noise. We demonstrated that, if the filamentary radio signal is traced perfectly by the distribution of galaxies, emission significantly below the sensitivity of the Bonn survey can be statistically detected. Our detection thresholds are already at a level expected in some models, and dramatic improvements using new surveys will be possible in the future.

Further refinements to the CC technique, including subtraction of point sources which also trace the LSS, will also improve its use as a detection tool for the diffuse baryons in filaments. The assumption of perfect correspondence between the distribution of galaxies and IGM radio emission is clearly an oversimplification, and further experimentation with numerical simulations are needed.

Partial support for this work at the University of Minnesota comes from the U.S. National Science Foundation grant AST 0607674. We acknowledge the use of NASA's SkyView facility located at NASA Goddard Space Flight Center.

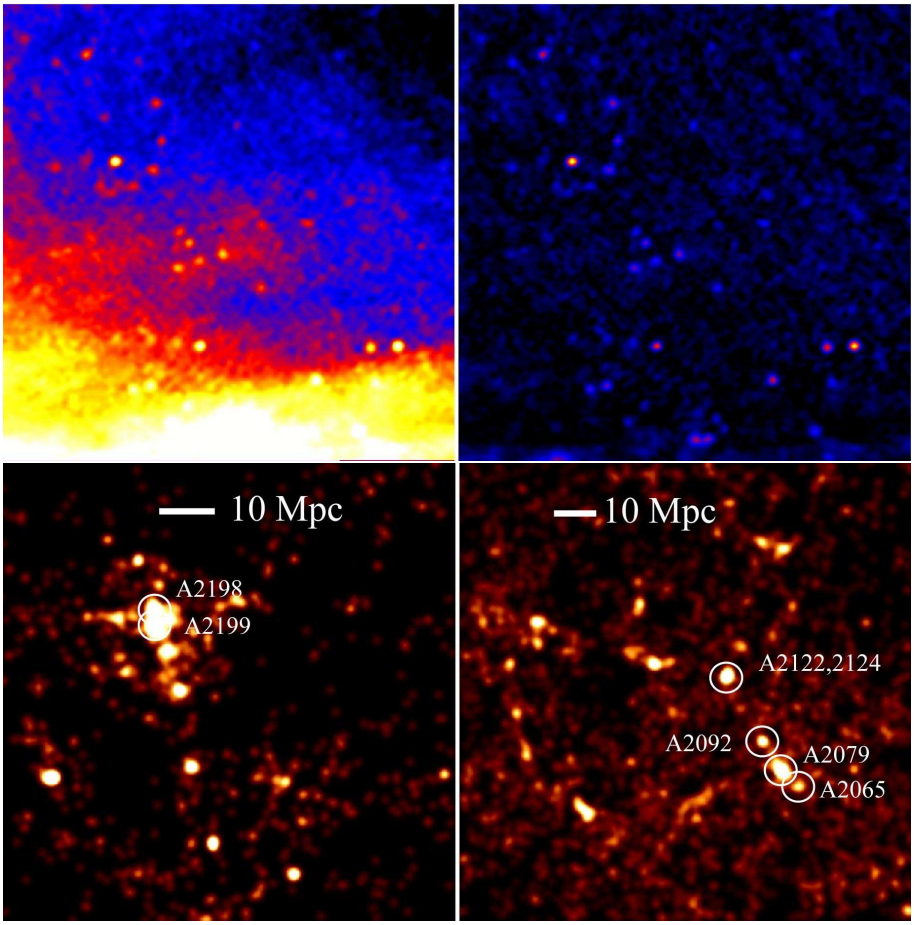

Figure 4.1: Center coordinates for each image are 16h00m00s +35d00m00s. Top-Left: Original $34^\circ \times 34^\circ$ 1.4 GHz, intensity Bonn image; Top-Right: Same field with Galactic gradients removed. The brighter point sources are 400-600 mK above the 3-3.5 K background in the unfiltered image. Bottom-Left: The distribution of galaxies from 2MASS with $0.03 < z < 0.04$, convolved to $36'$. Peak/mean=64; Bottom-Right: Same for $0.06 < z < 0.07$. Peak/mean=30.

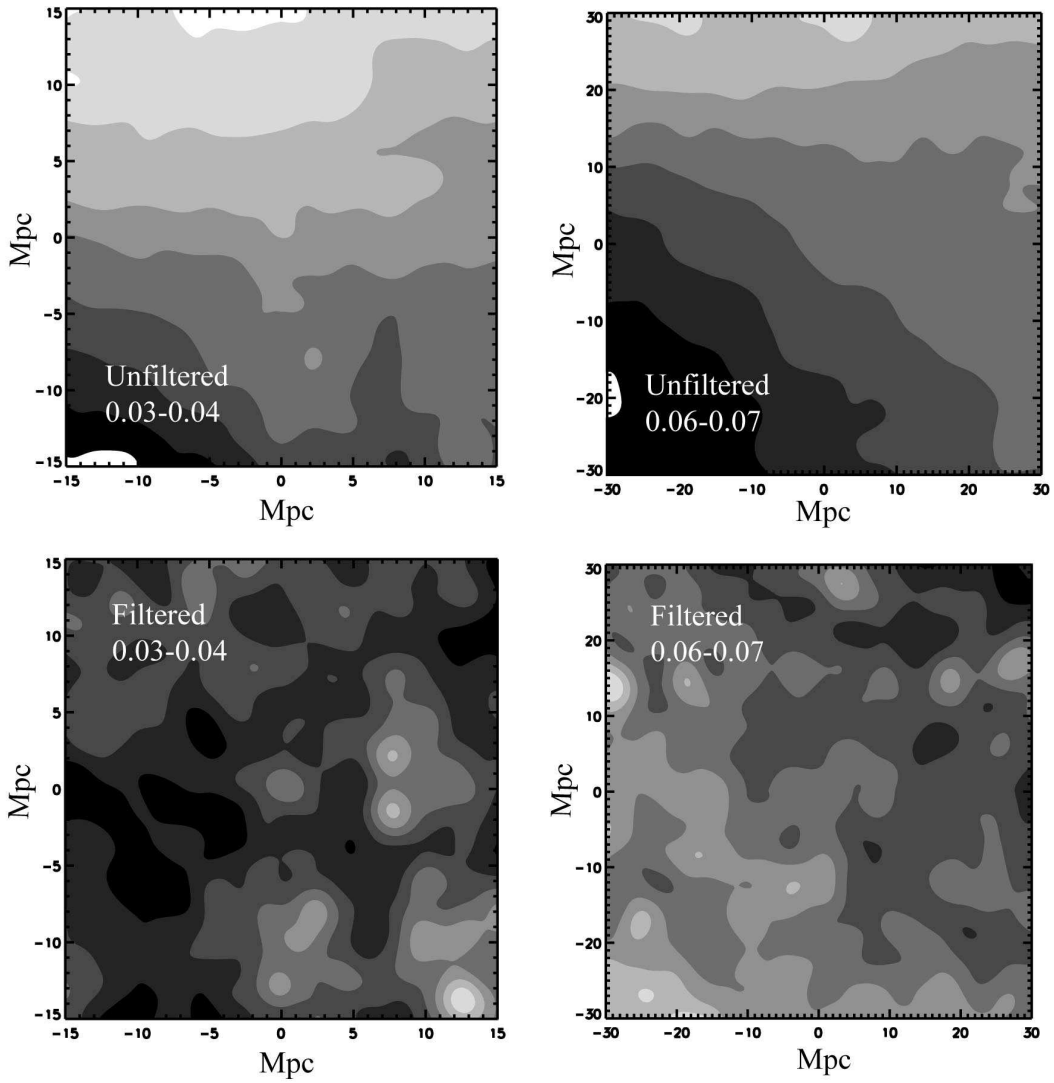

Figure 4.2: CCF for the unfiltered and filtered 1.4 GHz total intensity Bonn images and the $0.03 < z < 0.04$/ $0.06 < z < 0.07$ 2MASS surface density of galaxies. The angular scale for each image is 11.3° on a side (total shift of 201 pixels), which is ∼19 independent beams across. The CCFs are normalized and values range from -0.2 (black) to 0.2 (white) for the unfiltered CCFs and -0.1 (black) to 0.1 (white) for the filtered.

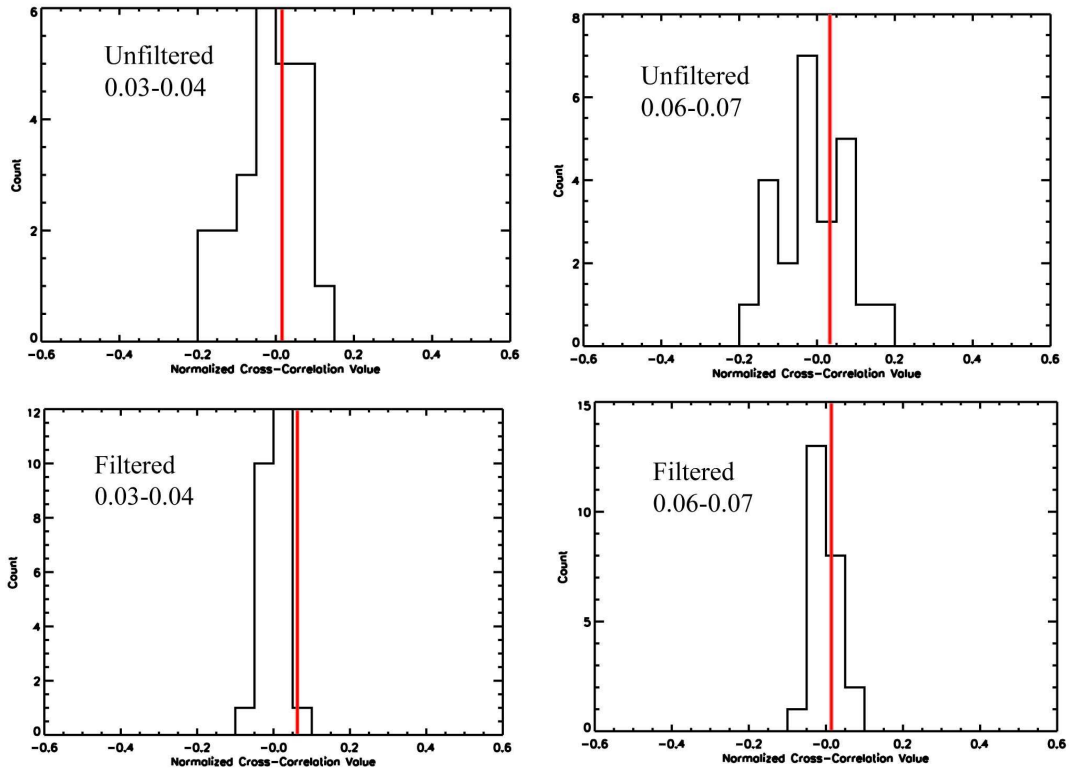

Figure 4.3: Distribution of cross-correlation values for the Bonn images with the 2MASS galaxy distribution images. Red lines indicate the CC value of the target field centered on 16H35D.

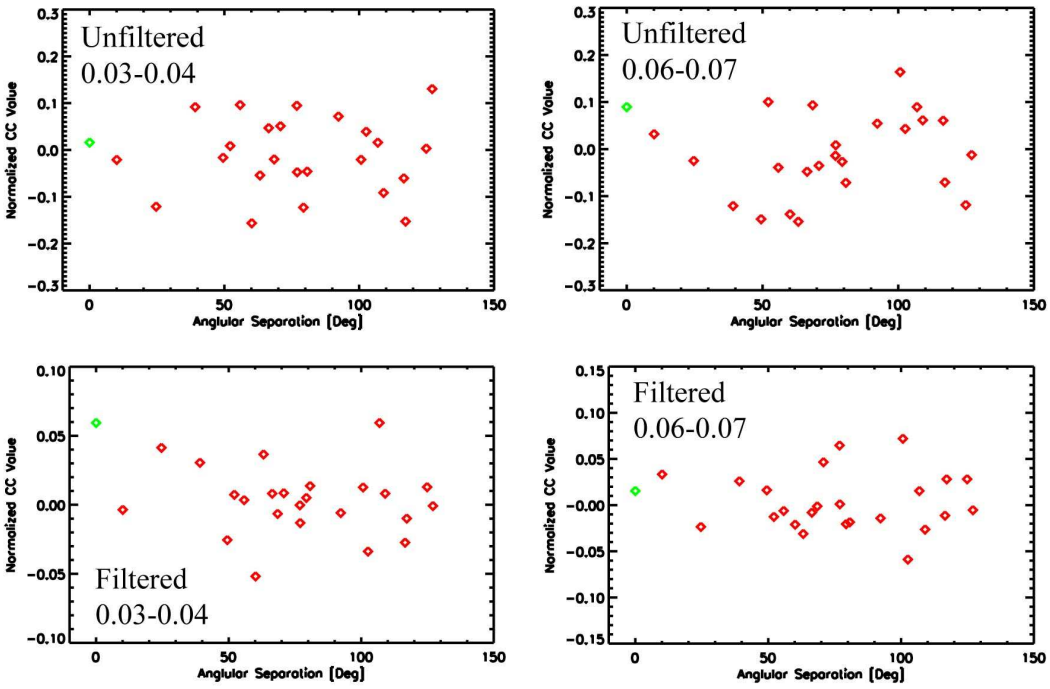

Figure 4.4: Sparsely sampled CC functions. Red diamonds are the 2MASS images correlated with the 24 Bonn fields. The Green diamond is the target fields CC value, and the dashed line is the 3σ value of the distribution.

Chapter 5

Diffuse Radio Emission in/around the Coma Cluster: Beyond the Simple Accretion Scenario

5.1 Introduction

Observations of diffuse radio emission in clusters of galaxies currently provide our only window into the relativistic particle population that potentially makes up a non-trivial fraction of the energy density in the Intra-Cluster Medium (ICM) (e.g., Skillmann et al. 2008). Large-scale features such as Giant Radio Halos (GRHs) and peripheral relics have been found in more than 50 clusters to date. Though the origin of the relativistic electrons is still unknown, all of these systems appear to have recently undergone at least some minor mergers/accretion.

There are three broad potential sources for the cosmic-ray electrons (CRe) in the ICM; extended radio galaxies (AGN models), electrons directly accelerated by accretion/merger shocks and/or cluster turbulence (primary models), and electrons created from relativistic proton-proton collisions from cosmic-ray protons (CRp) that have accumulated in the cluster's potential well (secondary models). There are variations in all three models based on the details of where and how the CRe (AGN & primary) and

CRp (secondary) are accelerated, though none of the models explain the rapidly accruing observational data. Recent efforts to construct a "unified model" for GRHs and radio relics (Pfrommer, Enßlin & Springel , 2008) using both primary and secondary models represent the next step in complexity, and will be tested by the next generation of low-frequency radio and gamma-ray telescopes.

The Coma cluster is a classic example of a merging/accreting system that hosts both a GRH (Coma C, Willson 1970) and peripheral radio relic (1253+275), and has been used as a test-bed for CR acceleration models (e.g., Donnert et al. 2009). The dynamical state of Coma has been well established through optical velocity analysis (Fitchett & Webster 1987; Mellier et al. 1988; Merritt & Trimbley 1994; Colless & Dunn 1996; and Adami et al. 2005).

Coma has been extensively observed in the radio. Kim et al. (1989) and Venturi et al. (1990) mapped the region with the WSRT at 326 MHz, finding a diffuse "bridge" of emission connecting the halo to the relic. Deiss et al. (1997) also detected the bridge at 1.4 GHz using the Effelsberg 100-m-telescope, and found the radio halo to have a diameter of $\sim 80'$. Using the 300 m Arecibo telescope combined with DRAO data at 408 MHz Kronberg et al. (2007) detected a $\sim 135'$ radio "cloud" surrounding both the classical halo and relic source. This cloud corresponds to $\sim$4 Mpc if it is associated with the Coma cluster, and would therefore extend into the Warm-Hot Intergalactic Medium (WHIM). The Coma cluster is also one of the few GRHs to have resolved spectral-index mapping (Giovannini et al. 2003), which shows a spectral steepening at larger cluster radii.

Coma has also been the subject of intense X-ray observations. In addition to surveys (e.g. the ROSAT All Sky Survey), mosaic $XMM-Newton$ observations (Briel et al 2001; Neumann et al. 2003; Schuecker et al. 2004) have revealed the complex thermal substructure of the X-ray halo. Detections of non-thermal hard X-ray emission have been claimed, e.g., using $RXTE$ (Rephaeli & Gruber 2002) and $BeppoSAX$ (Fusco-Femiana et al. 1999,2004). Diffuse *thermal* hard X-ray emission has been imaged with $INTEGRAL$ (Renaud et al. 2006; Eckert et al. 2007; Lutovinov et al. 2008) and $Suzaku$ (Wik et al. 2009), revealing temperature increases in the Western region of the cluster.

We present Green Bank Telescope (GBT) 1.41 GHz and Westerbork Synthesis Radio Telescope (WSRT) 352 MHz observations of the Coma cluster in an attempt to investigate the various CR acceleration models, as well as confirm the dramatic 4 Mpc radio cloud seen by Kronberg et al. (2007). We present the observations and data reduction in §2, and our observational results in §3. In §4 we present a discussion of the implications of our results, and summarize our key points in §5.

In this paper, we assume $H_o = 70$, $\Omega_\Lambda = 0.7$, $\Omega_M = 0.3$.

5.2 Observations & Data Reduction

We observed a 6°x6° region around the Coma Cluster with the Green Bank Telescope (GBT) between October 2007 and January 2008. We observed with the GBT's Spectrometer with a 50 MHz bandpass centered on 1.41 GHz. The region was sampled with 150 evenly spaced stripes; 75 with constant RA and 75 with constant Dec. Each 6° stripe was covered by 5, 60 second raster scans. We performed these scans one after another in order to search for repeatability and edit out those times where the overall power levels were unstable, due to either receiver or atmospheric fluctuations. During each night of observations, we scanned across some combination of 3C295, 3C48, 3C138 and 3C286. The first two are unpolarized calibrators and the second two are polarized. There where some nights where, for a variety of reasons, we did not observe an unpolarized calibrator.

Due to radio interference and instabilities in the Spectrometer gains, ∼35% of the data was unusable. Fortunately most of the bad data was in the outer regions of the image. Fig. 5.1 shows a total intensity image which combines both the constant RA and constant Dec stripes at 12′ resolution. The brightest feature is the background compact radio source Coma A. In order to get a more accurate image of the diffuse emission, we subtracted out the point sources from the NVSS survey. For this purpose, we only used the constant Dec. stripes, which were more stable than the constant RA stripes. Fig. 5.1 also shows the total intensity map[1] after NVSS subtraction made with constant Dec scans only (14.25′×13′ beam). A linear baseline was taken out of each scan, and the resulting map rms is ∼6 mJy beam^{-1}, and is dominated by diffuse Galactic emission.

[1] Polarization data will be presented at a later time.

We describe the halo and relic emission in §3.

A four pointing mosaic of the Coma cluster was also observed for a total of ∼48 hours over four nights in P-band (352 MHz) with the Westerbork Synthesis Radio Telescope (WSRT) in November of 2008. The array was in the maxi-short configuration with a shortest baseline of 36 m. One primary flux and one polarized calibrator (as a pair) were observed at the beginning and end of each night. For the primary flux calibrators we observed 3C147 and 3C295, and for the polarized calibrators we observed DA240 and 3C345. We used the WSRT wide band correlator to cover a frequency range from 310-390 MHz with eight 10 MHz wide bands, each with 128 channels and full Stokes parameters. IFs 3, 4, and 8 were not used due to interference and calibration problems. After removing the end channels in each band and editing for strong RFI, 400 channels remained in the final analysis, for a total bandwidth of 31 MHz.

The calibration and reduction of the WSRT data were performed using the NRAO's Astronomical Image Processing System (AIPS). The total intensity in each of the 4 bands was calibrated independently using standard procedures and the fluxes in the VLA calibrator manual for 3C147 and 3C295. We did several iterations of amplitude and phase self-calibration on each data set. Fig. 5.2 shows the total intensity image which is a combination of the 4 IF images with an average frequency of 352 MHz.

5.3 Results

5.3.1 Extended Relic

The relic emission shown in Fig. 5.1 is much larger and more diffuse than has been previously seen. Giovannini et al. (1991) measured a total extent for the relic of $25'$ using the WSRT and VLA. The diffuse relic as seen by the GBT extends through Coma A into the NW, with a total extent of $67'$, or 2 Mpc at the redshift of the Coma cluster. The single dish radio maps of Andernach et al. (1984) and Deiss et al. (1997) show hints of this faint extended emission NW of Coma A, though they did not associate it with 1253+275. The 408 MHz image of Kronberg et al. (2007) also shows emission extending this far to the NW of the known relic, but the halo and relic are not cleanly separated at those frequencies. The total flux density of the extended radio relic is highly uncertain due to the patchy galactic emission evident in the GBT images, and ranges between

200-500 mJy at 1.41 GHz. Giovannini et al. (2001) measured only 160 mJy at 1.4 GHz with the VLA, though they have a significant amount of missing flux. They find a best fit power-law to the data at other frequencies that predicts $\geq$200 mJy at 1.4 GHz. The relic, as seen in our 352 MHz image, is $\sim 28'$ long and has a flux density of 1700 mJy, comparable to the 326 MHz value of 1400 mJ given by Giovannini et al. (1991).

5.3.2 Halo Profile

In order to see the diffuse emission more clearly, we imaged all the point sources by using only UV data $> 700\ \lambda$, then subtracted clean components out of the original UV data with the AIPS task UVSUB. To further reduce point-source contamination, we applied the multi-scale spatial filter of Rudnick (2002) with a filter size of $375'' \times 375''$. Fig. 5.2 shows the result. The halo shows a sharp "front" along the Western edge, which is visible even in the non-point source subtracted image. Fig. 5.3 is a plot of azimuthally averaged surface-brightness over an 90° wedge that shows a factor of 5-7 increase in brightness at the front.

5.3.3 Other Diffuse Emission

We confirm the "bridge" of emission (Kim et al. 1989; Venturi et al. 1990) connecting the halo and relic in both the GBT and WSRT images. We also confirm much of the $\sim 135'$ "radio cloud" emission seen by Kronberg et al. (2007), who reported a 408 MHz flux density of 0.8-3 Jy for the cloud, which extended as far as 2.1° West of the peak halo brightness. In our GBT image, the halo has a diameter of roughly $84'$, and we do see low level emission between the halo and relic. However, we see more contrast between the extended relic and the halo at 1.41 GHz, indicating that the radio cloud has a steeper spectral index which makes the signal relatively weaker at higher frequencies.

5.4 Discussion

5.4.1 Relic

Given the apparent doubling in the known linear size of the radio relic in our GBT observations, let us revisit the current model of the relic as an accretion shock onto the

Coma cluster. We will first examine the relic's relation to optical and X-ray tracers of large-scale structure in the region, then explore the relevant science issues that arise.

The Coma cluster is one of the best studied clusters at all wavelengths, and several attempts have been made to reconstruct the dynamics of mass accretion onto the cluster (e.g., Adami et al. 2005). The average Coma radial velocity is 6925 km/s, and there is a well known infalling group from the West associated with NGC 4839 (7362 km/s). Fig. 5.4 shows a plot of SDSS spectroscopic galaxy velocities in a 2° high band through the Coma cluster and along an angle of 0.5 radians South of West, which includes the infall cluster and the relic region. Also shown is a two component Gaussian fit to the velocity distribution. The narrow, infall component, has a peak of 27 galaxies, a center of 7450 km/s, and an rms dispersion of 300 km/s. The broader residual has a peak of 30 galaxies, a center of 7000 km/s, and an rms dispersion of 935 km/s. Fig. 5.4 also shows a grayscale image of the smoothed galaxy surface-density (from SDSS spectroscopic data) for the range $6600 < v < 8200$. This infalling velocity range shows a dramatic drop-off or "wall" in the surface density of galaxies at the inner edge of the extended radio relic. Remarkably, the transverse extent of the wall is also comparable to the relic, ∼2 Mpc. Fig. 5.5 shows a 1-D slice across the Coma halo and relic in radio (1.4 GHz) and X-ray[2] brightnesses, and the same slice except 1.0° wide through the optical surface density of SDSS galaxies in three velocity cuts. The X-ray emission does not extend past the relic, and there is also a sharp drop in the number of galaxies with $6600 < v < 8200$ just as the relic radio emission increases. Several infalling groups of galaxies have been identified near this region (e.g., Adami et al. 2005), but this is the first identification of a more extended infall region into the Coma cluster.

The correspondence between the wall of galaxies and the inner edge of the radio relic suggests a causal link between the two. This however poses a problem for the association between the radio relic and the NAT radio source NGC 4789, which is a possible source of seed relativistic electrons (Enßlin et al. 1998). Given its radial velocity of 8365 km/s and the morphology of the bent jet, NGC 4789 is apparently on the back side of the cluster (moving away), while the wall of galaxies, if associated with the NGC 4839, must be in front of the cluster (moving in). If the relic is indeed associated with the infalling wall of galaxies, then it would explain why the models of Enßlin et al. (1998)

[2] The X-ray data was taken from an archival ROSAT PSPC image

underestimated its fractional polarization; we are viewing the relic almost edge on. A detailed model of the optical infall is needed in order to resolve these issues, and is beyond the scope of this work.

The increase in the relic's size, luminosity etc., poses no fundamental theoretical problems, nor does it make 1253+275 an extreme relic observationally (see, e.g., Brown & Rudnick 2009 for a compilation of observed relics and their radio luminosities L_{Radio}). In fact, 1253+275 is on the lower radio luminosity envelope of L_{Radio} vs. L_X correlation, as seen in Fig. 15 of Brown & Rudnick (2009), which has an order of magnitude scatter in L_{Radio} values.

However, why would there be a coherent *planar* shock front over 2 Mpc in extent? Large shock-fronts of this size have been seen for outwardly propagating shocks (Röttgering et al. 1997; Johnston-Hollitt et al. 2002; Bonafede et al. 2009), but those are spherical while 1253+275 with the newly discovered extension is straight (with a radius of curvature >30 Mpc). In addition, the curious wall of infalling galaxies adjacent to the relic's inner edge is a puzzling feature. Further investigation, especially with numerical simulations, is needed in order to understand these issues.

5.4.2 Halo

The sharp synchrotron front seen in Figure 5.2 is not typical of classical GRHs. It is located on only one side of the cluster, and shows a discrete drop-off in brightness (Fig. 5.3) and is relatively flat (the center for the radius of curvature is not the cluster center, but 13h01m20s+27d57m). We will first compare the front to published and archival X-ray information, then examine possible origins for the synchrotron emission. Finally, we will examine the global radio vs. X-ray correlation of the radio halo in the context of GRH origin models.

Many deep X-ray observations have been taken of the Coma cluster with telescopes such as ROSAT, XMM, Chandra and Suzaku. X-ray soft (Bonamente et al. 2009) and hard excesses (e.g., Eckert et al. 2008) have been claimed in the Western infall region, which have been attributed to non-thermal IC emission. The non-thermal nature of the excess has been ruled-out/challenged by Wik et al. (2009) using Suzaku, though they confirm higher temperatures in the western region roughly corresponding to the synchrotron front. Neumann et al. (2003) found an excess above a beta-model also

on the western front, though closer to the cluster than the synchrotron front. Clearly this is a region of infall activity, though the exact kinematics is not clear (Adami et al. 2005). Fig. 5.6 shows the Neumann et al. (2003) XMM contours overlaid on our 352 MHz diffuse radio map. The outer edge of the X-ray excess roughly corresponds to the outer edge of the diffuse synchrotron. A deep XMM-Newton mosaic of the Coma cluster was taken (Schuecker et al. 2004; Wik et al. 2009) that allowed a spatially resolved temperature map to be made. Fig. 5.7 shows our 352 MHz diffuse contours over the XMM temperature map; there is an apparent temperature increase on the outer edge of the halo front. Higher signal/noise fits were taken of the boxed regions (Alexis Finoguenov, private communication) which found $16.3^{+3.5}_{-2.3}$ keV on the exterior and $6.8^{+0.7}_{-0.5}$ keV on the interior.

The sharp edge in the 352 MHz radio map of the halo has no straightforward explanation. At present the problem arises because the thermal gas is hotter *outside* of the synchrotron front, as shown in Fig. 5.7 from Wik et al. (2009). There are several possible origins for regions of increased temperature, all of which seem improbable.
1: The gas could be shock heated ICM or IGM. If the front were an accretion shock, the synchrotron should peak at the shock location, and the hot gas will be hottest post shock and fade away. On the contrary, we observe that the hot gas further from the cluster than the front, which is the apparent shock location in this scenario.
2: If the hot gas where stripped from a merging subcluster, one would also expect the X-ray surface brightness to also peak at that location, which it does not.
3: It could be a hot, low-density "bubble" due to an extended radio galaxy that was left behind during the accretion process. The pressure profile across the hot region could rule out 3, with a pressure jump disfavoring a relic bubble which should be in pressure balance with the thermal ICM. This will be explored in a future paper. At present, this discrete front of synchrotron emission remains a mystery.

5.4.3 Global Radio vs. X-ray Correlation

Models of GRH origins predict a pixel-to-pixel correlation between the radio and X-ray brightnesses within clusters. Typically one would look for a power-law correlation of the form

$$F_{Radio} = a\,(F_X)^b\,, \tag{5.1}$$

where F_{Radio} and F_X are the radio and X-ray flux densities (per pixel) and a and b are constants. Here we will focus on b, which parameterizes particle acceleration models.

Govoni et al. (2001) found a power law correlation with b=0.64±0.07, using 326 MHz WSRT data. We also show a correlation (Fig. 5.8) obtained using ROSAT PSPC data and our point-source subtracted 352 MHz image, with b=0.45±0.01. Fig. 5.8 also show the fit from Govoni et al. (2001) and the models predicted by Pfrommer et al. (2008, see below). Govoni et al. (2001) illustrate, for primary electron models, that b≈1 if one assumes that the cluster is: 1) iso-thermal; 2) the magnetic, thermal, and cosmic-ray electron (CRe) energy densities are proportional to each other, with the same proportionality constants throughout the cluster (the proportionality premise); and 3) the radio spectral index is α=1.

The F_{Radio} vs. F_X correlation found by Govoni et al. (2001) and the current work can be compared to the unified model of diffuse cluster radio emission presented by Pfrommer et al. (2008), who find b=1.3-1.7 for secondary electron emission, and roughly linear (b=1, though with a broad distribution) for primary electron emission at lower radio surface-brightness levels. The simulations of Pfrommer et al. (2008) assume proportionality when calculating synchrotron emissivity, which is likely why they get a roughly linear power-law for primary electron radio emission. Donnert et al. (2009) modeled the Coma cluster using a hadronic secondary model for the cosmic-ray populations and turbulence amplified magnetic fields seeded by galactic outflows. They found that the proportionality premise (except replace CRe with CRp for a secondary model) needed to be broken in order to fit the Govoni et al. (2001) data. In fact, the ratio of the CRp to thermal energy densities reached an unphysical >100% at a cluster radius of ∼1 Mpc. In addition, the steepening of the halo's spectral index (Giovannini et al. 1993) at larger cluster radii could not be explained with a secondary model. Clearly the current models do not provide sufficient degrees of freedom to reproduce the observed correlations, and further numerical and observational investigations are needed in order to uncover the complete physical model of GRHs.

5.5 Summary

We conducted observations of Coma cluster at 1.41 GHz with the GBT and 352 MHz with the WSRT. Our key findings are:

• We detect an extension to the radio relic source 1253+275, making it ∼2 Mpc in transverse extent.

• The extended relic lies just outside a previously unidentified ∼2 Mpc "wall" of infalling galaxies, of which the well known infalling group associated with NGC 4839 is a part. The physical relationship between this wall of galaxies and the radio relic is still unclear.

• There is a diffuse, low surface-brightness "front" of synchrotron emission on the Western edge of the 352 MHz radio halo. Its discrete edge suggests the presence of a shock or compression/confinement on the Western edge of the halo, though its actual origin is unclear, since the X-ray temperature jump is opposite of expectations.

• We confirm the existence of very low brightness emission between the halo and relic, although at a somewhat weaker level than reported by Kronberg et al. (2007) at 408 MHz.

• We find $F_R \propto F_X^{0.45\pm.001}$, in broad agreement with Govoni et al. (2001), and much flatter than primary and secondary models for the origin of the Coma cluster.

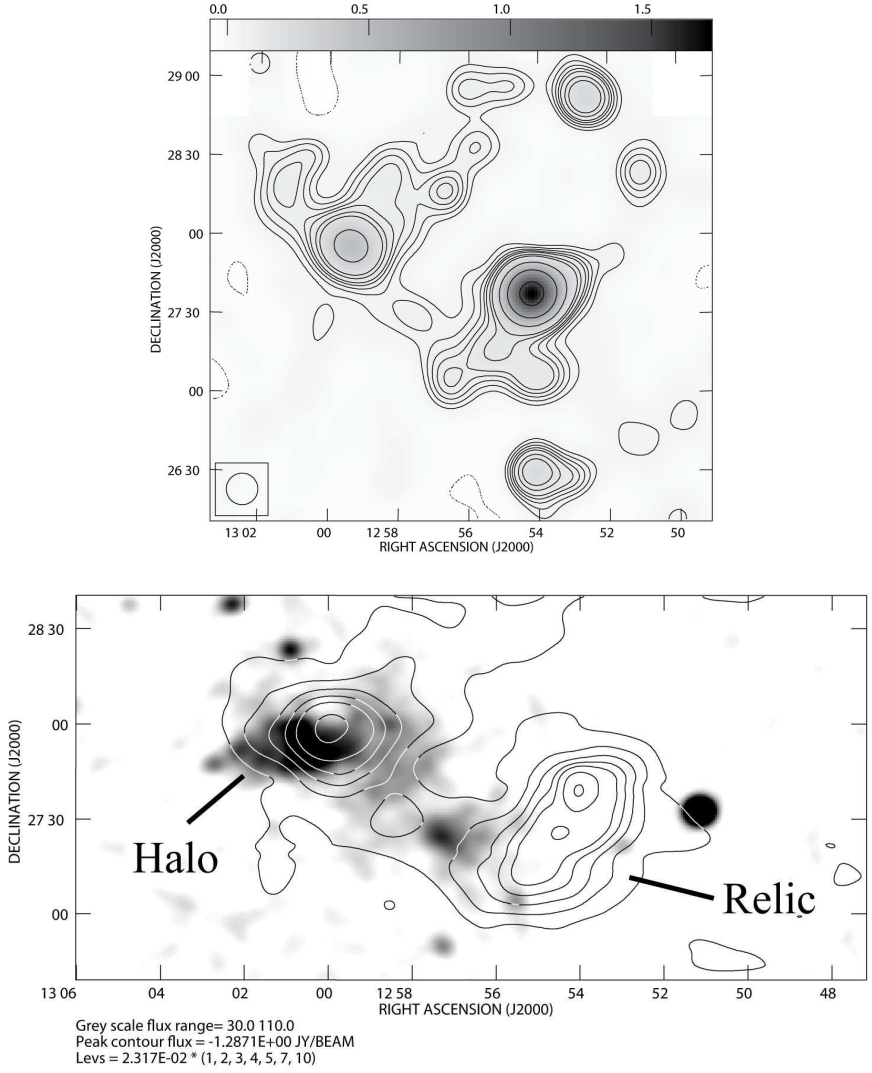

Figure 5.1: Top: GBT total intensity image of the Coma cluster; $12' \times 12'$ resolution; Bottom: GBT total intensity contours with only constant DEC scans and NVSS point sources subtracted out ($14.25' \times 13'$ beam). Grayscale is ROSAT X-ray residual image after a beta-model has been subtracted.

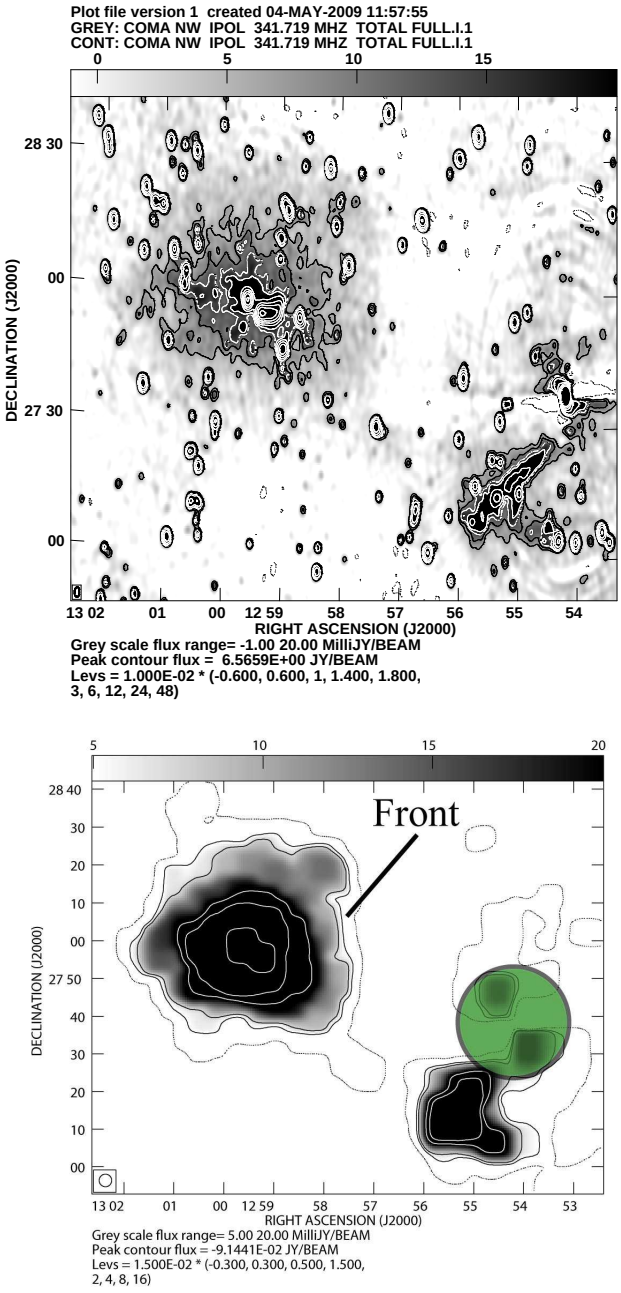

Figure 5.2: Top: WSRT total intensity image of the Coma Cluster. The image was made from a 4-pointing mosaic with a central frequency of 352 MHz (31 MHz bandwidth) and a resolution of $134' \times 68'$. Bottom: Same as above, but with point sources (UV data >700 λ) removed. The green circle indicates a region where the background radio source Coma A has left residual artifacts, and should be ignored.

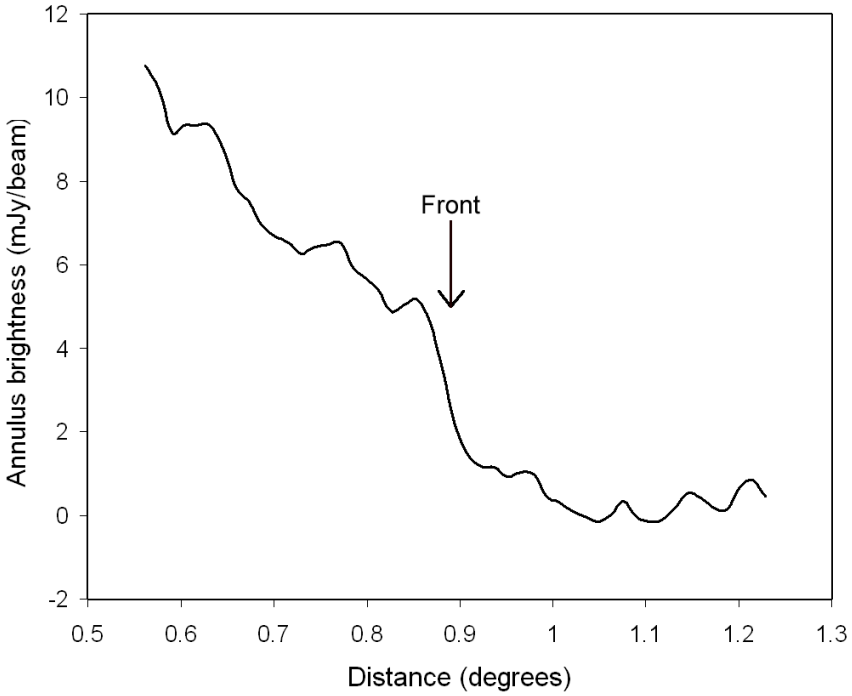

Figure 5.3: Annular average of the point-source subtracted WSRT image showing the new "front" of synchrotron emission. The average was over a 90° wedge centered on 13h01m20s+27d57m.

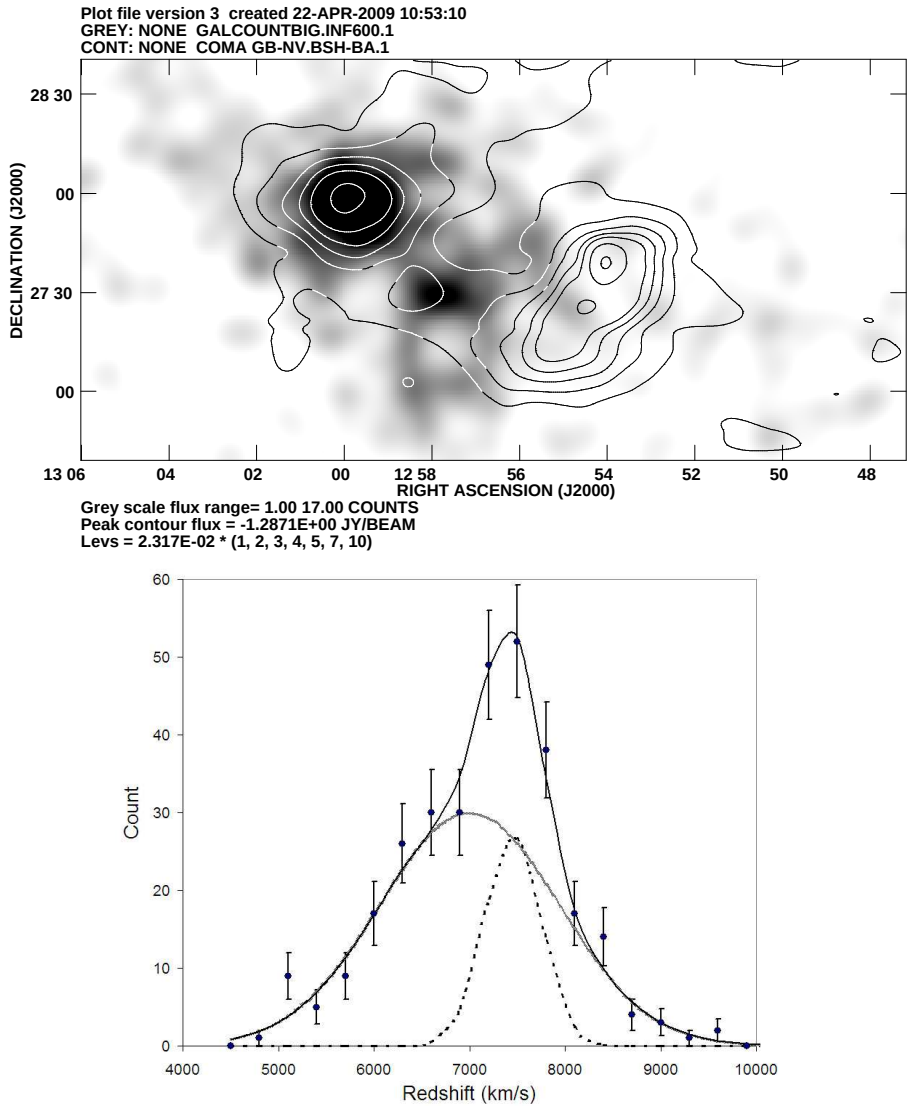

Figure 5.4: Top: Plot of velocities in a 2deg high band through the Coma cluster and from 0.5 to 1.5 degrees from the Coma center, at an angle of 0.5 radians, which includes the infall cluster and the broader wall. shown is two component Gaussian fit to the velocity distribution. Infall: peak 27; center 7450 km/s; FWHM 700 km/s Residual: peak 30; center 7000 km/s; FWHM 2200 km/s; Bottom: Smoothed surface-density of optical galaxies from the SDSS spectroscopic database with $6600 < v < 8200$ (grayscale) with GBT contours from Fig 1. Note the "wall" of galaxies that ends on the inside edge of the radio relic.

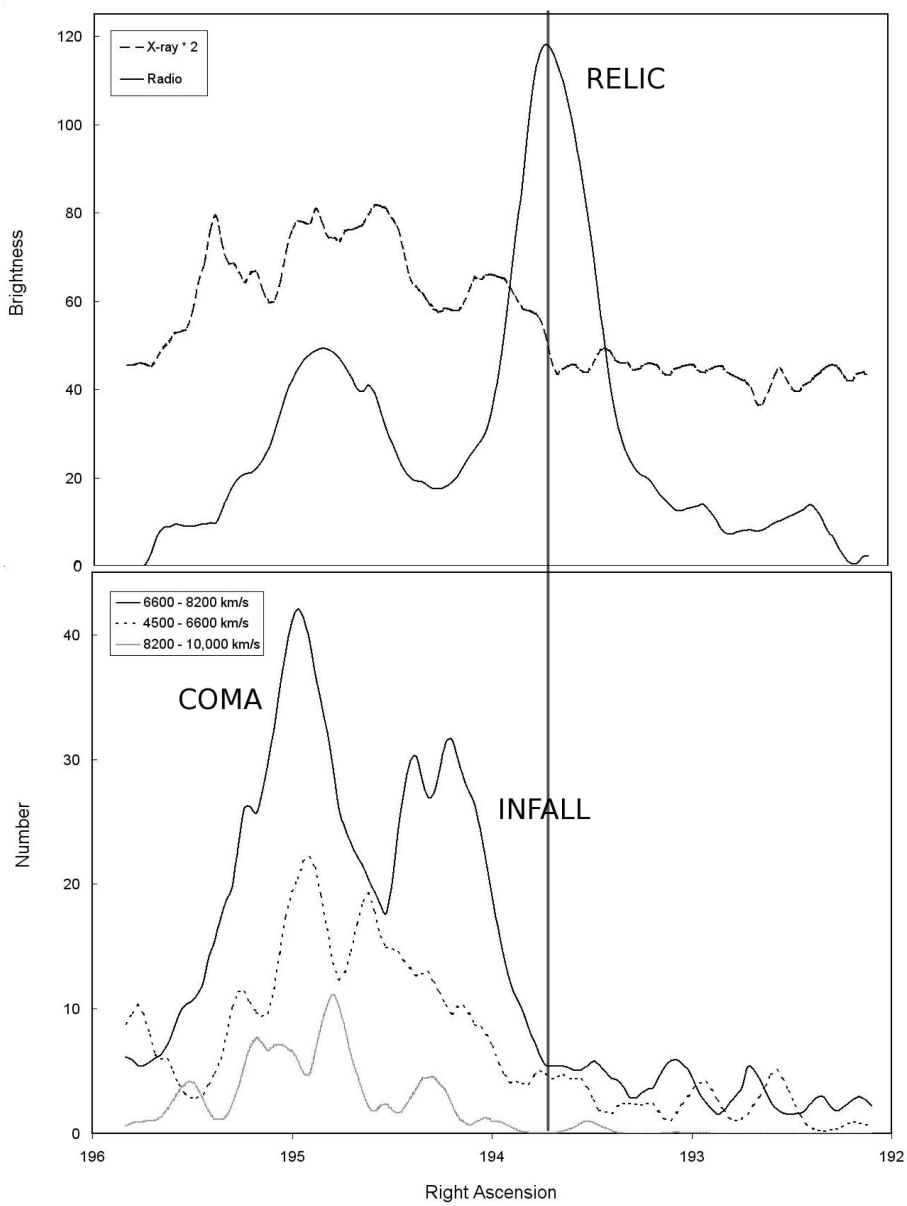

Figure 5.5: Top: 1-D slice across the Coma halo and relic in radio and X-ray brightness; Bottom: Same slice except 1.0° wide through the optical surface density of SDSS galaxies in three velocity cuts. Note the drop in number of galaxies with $6600 < v < 8200$ as the relic radio emission increases.

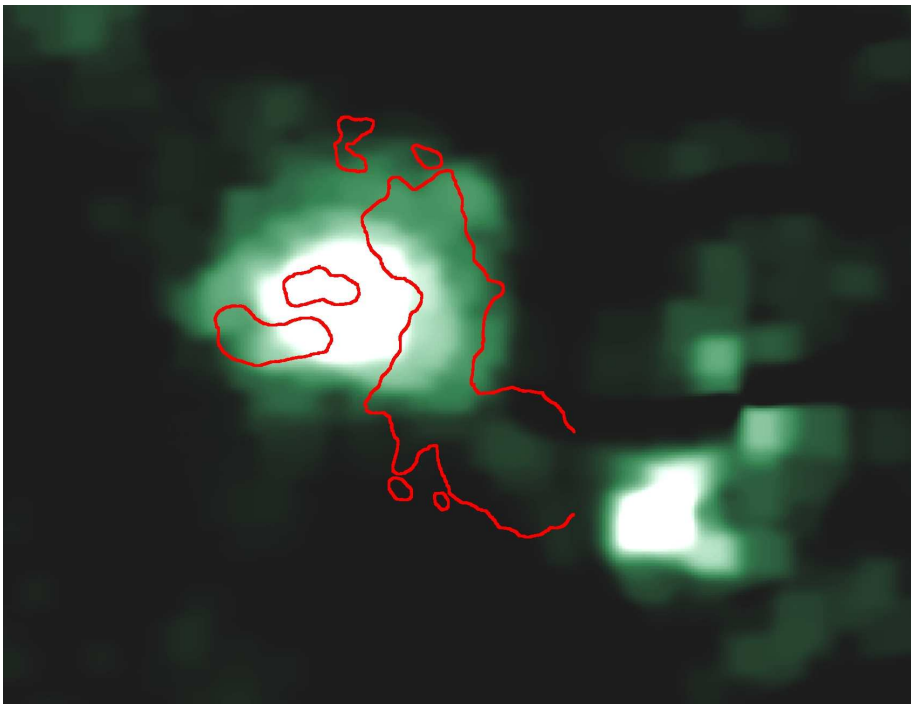

Figure 5.6: Grayscale is the point-source filtered "open" map (Fig. 2) with X-ray contours from Neumann et al. (2003). The contours are residual X-rays after a relaxed cluster beta-model has been subtracted out, and indicate regions of active infall.

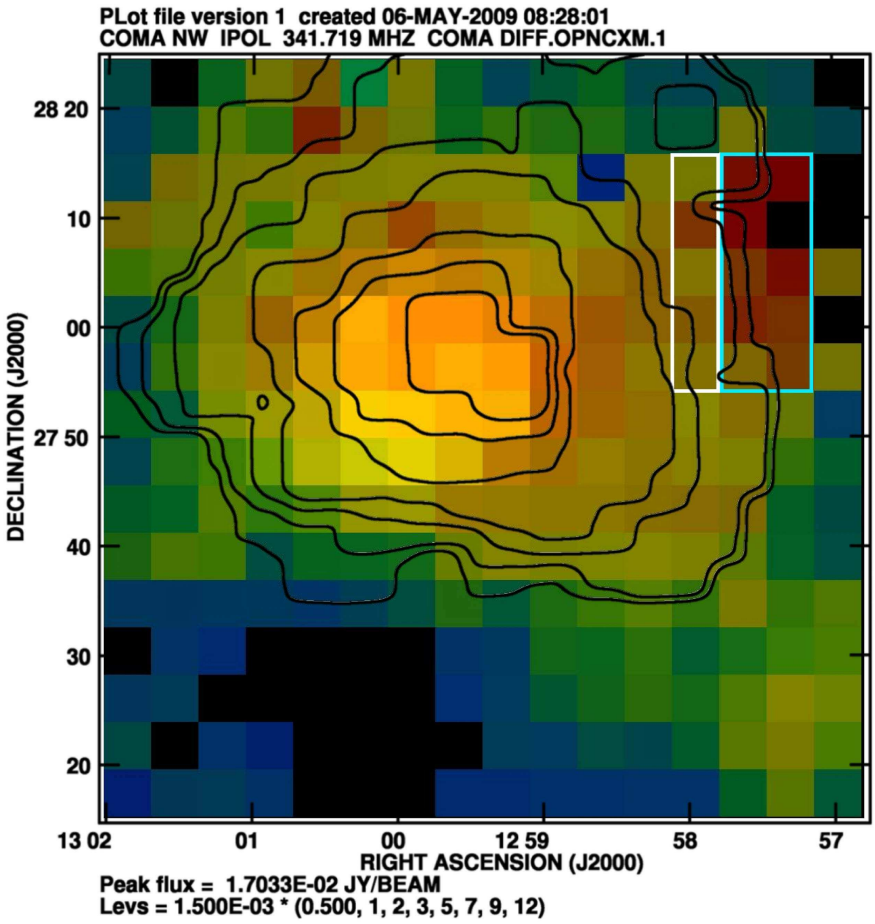

Figure 5.7: Thermal X-ray temperature map (Wik et al. 2009) with diffuse radio contours overlaid. The color scale goes from purple/blue 1.5 keV to red/white 12 keV. Higher signal/noise fits were taken of the boxed regions (Alexis Finoguenov, private communication) which found $16.3^{+3.5}_{-2.3}$ keV on the right and $6.8^{+0.7}_{-0.5}$ keV on the left.

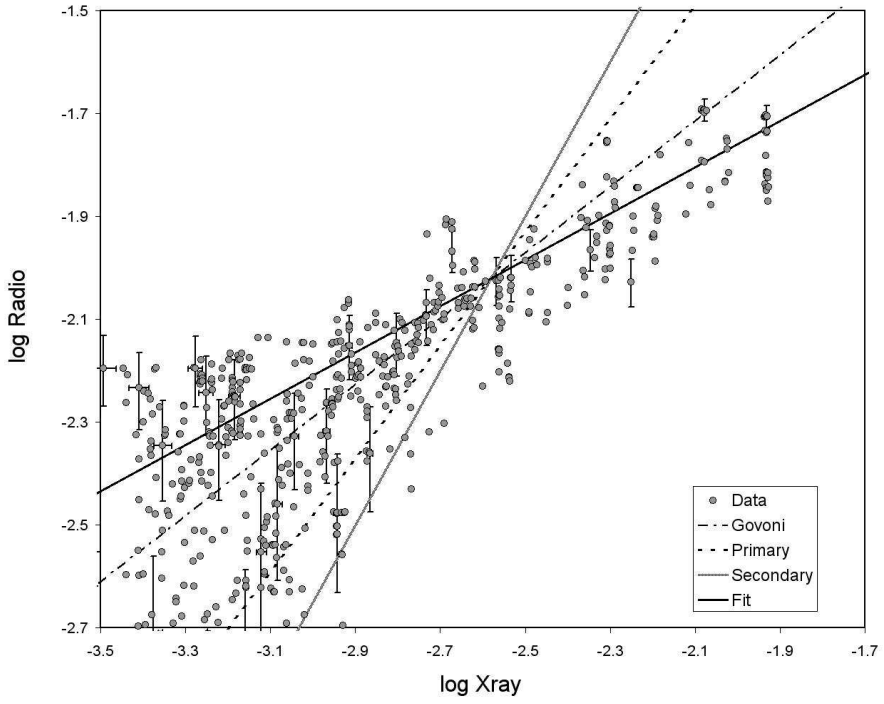

Figure 5.8: Data points are a pixel-to-pixel correlation between the diffuse radio surface-brightness at 352 MHz and the X-ray surface brightness from ROSAT. Also shown is the measured power-law correlation found by Govoni et al. 2001, as well as predicted correlations for primary and secondary models.

Chapter 6

Conclusion and Future Work

Despite the efforts outlined in this dissertation, very little is known observationally about the existence or properties of ionized gas and magnetic fields outside of rich X-ray emitting clusters of galaxies. The physical state of the filamentary IGM can have a significant effect of large-scale structure formation, and roughly half of the ordinary matter in the universe remains undetected in these regions. Therefore, the issue of detecting and characterizing the low-density filamentary regions of the cosmic web will continue to be on the forefront of cosmology in the coming decade.

Synchrotron radio emission has proven to be a reliable probe of magnetic fields and relativistic particle in cosmological large-scale structure. Chapters 2 & 5 showed the utility of synchrotron emission in highlighting interesting and dynamic systems, even when the thermal plasma was too diffuse to be detected. In chapters 3 & 4, I developed and tested new techniques for pushing below the total intensity confusion limit. Polarized radio emission was shown to reveal complex structures in the NVSS survey spanning hundreds of degrees (chapter 3), though it remained invisible in total intensity, and in chapter 4 I explored the promise of using cross-correlation to reveal filamentary synchrotron emission that is fainter than the noise level and the radio survey.

6.1 Key Messages

The key findings presented in this dissertation are:

• The large-scale diffuse radio emissions found thus far associated with luminous X-ray

cluster of galaxies are clearly the brighter end of the much more extended synchrotron "cosmic-web".

• Polarized emission can reveal coherent synchrotron emitting regions on scales larger than the shortest-baseline limit of interferometric measurements. This was demonstrated with the NVSS survey, where *hundreds* of new features were found, including a new Galactic loop.

• Confusion from our own Galaxy limits our ability to cleanly identify this cosmic-web over a wide range of spatial scales.

• Cross-correlation is a powerful tool for identifying this filamentary emission, and we have attempted this method for the first time and demonstrated its utility on simulated filament emission.

• We have also demonstrated the variety and complexity of phenomena that can be traced with synchrotron emission (even in the well studied Coma cluster), as well as the inadequacy of current models to explain these features.

6.2 Future Work

6.2.1 Low Frequency Polarized Foregrounds

Upcoming low-frequency radio arrays (LOFAR, MWA, LWA, etc.) have the potential to directly image the large-scale structure related synchrotron emission. However, as my work has shown in several cases, diffuse-polarized Galactic emission will present a significant source of confusion when trying to identify true extra-Galactic filamentary emission.

In preparation for the complex foreground separation that will likely need to be performed at $\nu < 150$ MHz, I will characterize the Galactic polarized emission seen at the WSRT with RM-Synthesis (Fig. 1). Using 10 pointings at $\sim$350 MHz, which sample a wide range in Galactic latitudes, I will compute for the first time the high Galactic latitude angular power-spectrum (APS) of the diffuse polarized foreground as a function of Faraday depth. Bernardi et al. (2009) have recently computed the APS at 150 GHz in a limited region of the Galactic plane. Given our resolution of $\sim 2'$ and the primary beam at 350 MHz, we will be able to sample the APS (C_l) from $l = 90 - 5400$ (Seljak 1997). With these data, we will be the first to probe the APS with such resolution and

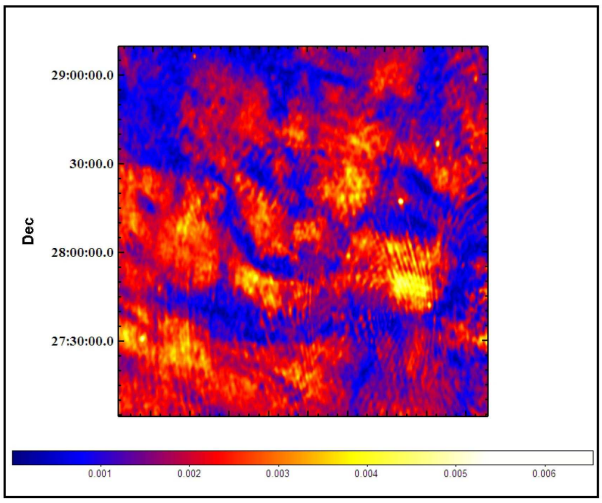

Figure 6.1: Image of the Galactic polarized foreground emission at a Faraday depth of zero in the region of the Coma cluster. The color bar is in units of Jy beam^{-1}, where the beam is $70' \times 70'$.

Galactic latitude range as a function of Faraday depth. Previous studies have included, e.g., Giardino et al. (2001,2002), Carretti et al. (2005), La Porta et al. (2006,2008), and La Porta & Burigana (2006). I will also explore techniques to model and subtract the diffuse emission, and set limits on the residual extra-Galactic signal.

6.2.2 Detecting the WHIM with the SZE

When the Cosmic Microwave Background (CMB) passes through hot gas like that found in clusters of galaxies, it gets scattered to a higher frequency/energy causing a cool spot (at frequencies <150 GHz) in the CMB called the Sunyaev-Zeldovich effect (SZE). The WHIM, which is 10^5-10^7 K, should also produce the SZE, though with a much lower amplitude than the hot cluster gas. Hallman et al. 2008 predict that the WHIM and other unbound gas contributes up to 12% of the integrated SZE effect, and can affect measured cosmological parameters.

With the GBT I will also explore the use of the new 90 GHz Mustang instrument to detect the Sunyaev-Zeldovich effect of the thermal WHIM on the CMB. Mustang is a 64 pixel bolometer array being commissioned on the GBT with $10''$ resolution and σ_{rms}

= 0.4 - 0.8 mJy/beam (or 100 - 200 μK with 0.26 K/Jy for a $3' \times 3'$ map in one hour). I will target well defined optical filaments that intersect large clusters/super-clusters of galaxies, where the majority of the WHIM is thought to reside. The expected SZE signal at $\nu = 90$ GHz for filaments of this type is $\sim$0.1-100 μK. These observations would be complementary to absorption studies as it would detect the higher temperature WHIM.

6.2.3 ALFALFA & GALFACTS

I am the lead scientist on the ALFALFA science project "Probing the WHIM with ALFALFA". ALFALFA is a deep Arecibo HI survey of the entire available sky (Giovanelli et al. 2005) using the new 1.4 GHz, 7 beam ALFA receiver. We will produce systematics corrected and point source subtracted (using NVSS) *continuum* maps of the entire survey area, producing the most sensitive, highest resolution ($3.8'$), 1.4 GHz single-dish map to date of a large fraction of the sky. Since the survey is currently confusion limited, we do not yet know the final sensitivity, though preliminary results have allowed us to reduce the confusion by at least a factor of a few (Fig. 2).

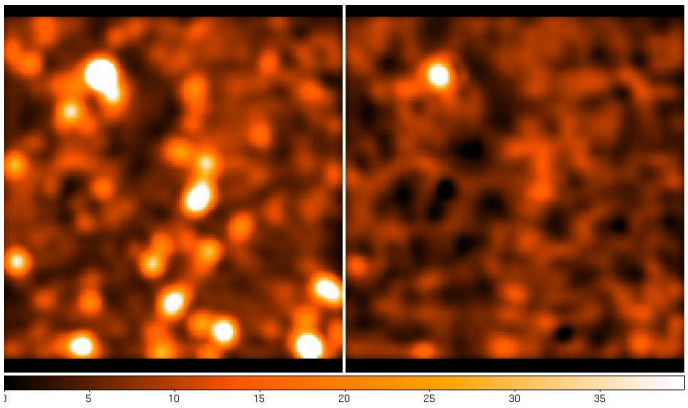

Figure 6.2: Left: continuum image from gridbf 2316+15c smoothed to $6'$; Right: The same image with NVSS point sources partially subtracted out. There are many alignment and beam issues that still need to be addressed, and the systematic striping has not been taken out.

I am also searching for filamentary emission as part of the GALFACTS consortium. The GALFACTS survey, a large 1.4 GHz survey starting this fall (also using the ALFA

receiver at Arecibo), will be superior to ALFALFA in continuum sensitivity. With the added benefit of full polarization, GALFACTS will be a key finding survey for LSS plasma, especially the flatter spectrum regions close to the shock fronts, and provide an ideal data set for cross-correlation studies and deep GBT and EVLA follow-up observations.

6.2.4 ASKAP Telescope: POSSUM & EMU

The Australian Square Kilometer Array Pathfinder (ASKAP) is an upcoming 36 antenna phased-array interferometer that will make wide FOV, deep observations around 1.4 GHz. ASKAP is meant to test some of the technology that is critical for making the SKA a reality in the coming decades.

POSSUM and EMU are two proposed continuum surveys with ASKAP, with POSSUM focusing on polarization and EMU on total intensity. These two surveys will reach μJy/beam sensitivity levels, which is sufficient to test models of cosmic magnetic field origins (Donnert et al. 2008; Ryu et al. 2009). I intend to utilize the diffuse polarized maps of POSSUM to detect LSS formation shocks, though it will likely only sample the tip of the luminosity function for these objects. With EMU, I'?ll focus on all-sky cross-correlation studies to statistically detect very faint filamentary synchrotron emission. All of this will help develop techniques that, with the coming SKA, will revolutionize our understanding of the WHIM and its relativistic/magnetic constituents.

References

Abell, G. O., Corwin, H. G., Jr., & Olowin, R. P. 1989, ApJS, 70, 1

Adami, C., Biviano, A., Durret, F., & Mazure, A. 2005, A&A, 443, 17

Adelman-McCarthy, J. K., & et al. 2007, VizieR Online Data Catalog, 2276, 0

Anderson, M. C., Keohane, J. W. & Rudnick, L., 1995, ApJ 441, 300

Artyukh, V. S., Ogannisyan, M A. & Tyul'bashev, C. A., 1994, AstrL 20, 211

Bagchi, J., Enßlin, T. A., Miniati, F., Stalin, C. S., Singh, M., Raychaudhury, S., & Humeshkar, N. B. 2002, New Astronomy, 7, 249

Battaglia, N., Pfrommer, C., Sievers, J. L., Bond, J. R., & Enßlin, T. A. 2009, MNRAS, 155

Becker, R. H., White, R. L., & Helfand, D. J. 1995, ApJ, 450, 559

Bell, A. R. 1978, MNRAS, 182, 147

Blandford, R., & Eichler, D. 1987, PhysRep, 154, 1

Blanton, E. L., Gregg, M. D., Helfand, D. J., Becker, R. H., & White, R. L. 2003, AJ, 125, 1635

Bonafede, A., Giovannini, G., Feretti, L., Govoni, F., & Murgia, M. 2009, A&A, 494, 429

Bonamente, M., Lieu, R., & Bulbul, E. 2009, arXiv:0903.3067

Brown, S., & Rudnick, L. 2009, AJ, 137, 3158

Brunetti, G., Venturi, T., Dallacasa, D., Cassano, R., Dolag, K., Giacintucci, S., & Setti, G. 2007, ApJL, 670, L5

Brunetti, G., Blasi, P., Cassano, R., & Gabici, S. 2009, American Institute of Physics Conference Series, 1112, 129

Brentjens, M. A., & de Bruyn, A. G. 2005, A&A, 441, 1217

Brentjens, M.A. 2007, PhD Thesis

Burn, B. J. 1966, MNRAS, 133, 67

Battye, R. A., Browne, I. W. A. & Jackson, N. 2008, MNRAS 385, 274

Bennett, C.L., et al., 1992, ApJ, 396, L7

Berkhuijsen, E. M., 1971, A&A 14, 359

Böhringer, H. et al., 2004, A&A 425, 367

Brentjens, M. A. & de Bruyn, A. G., 2005, A&A 441, 1217

Burbidge, G. & Burbidge, E. M., 1961, PASP 73, 191

Cen, R., & Ostriker, J. P. 1999, ApJ, 514, 1

Cen, R., & Ostriker, J. P. 2006, ApJ, 650, 560

Cao, L., Chu, Y.-Q., & Fang, L.-Z. 2006, MNRAS, 369, 645

Condon, J. J., Cotton, W. D., Greisen, E. W., Yin, Q. F., Perley, R. A., Taylor, G. B., & Broderick, J. J. 1998, AJ, 115, 1693

Castelletti, G., Dubner, G., Brogan, C. & Kassim, N. E., 2007, A&A 471, 537

Cioffi, D. F., & Jones, T. W. 1980, AJ, 85, 368

Clarke, T. E., & Ensslin, T. A. 2006, AJ, 131, 2900

Condon, J. J., Cotton, W. D., Greisen, E. W., Yin, Q. F., Perley, R. A., Taylor, G. B., & Broderick, J. J. 1998, AJ, 115, 1693

Csabai, I., et al. 2003, AJ, 125, 580

Condon, J., Broderick, J. & Seielstad, G., 1991, AJ 102, 2041

Condon, J. J., & Broderick, J. J., 1985, AJ 90, 2540

Condon, J. J., Cotton, W. D., Greisen, E. W., Yin, Q. F., Perley, R. A., Taylor, G. B., & Broderick, J. J., 1998, AJ 115, 1693

Davé, R., et al. 2001, ApJ, 552, 473

Donnert, J., Dolag, K., Lesch, H., Muumlller, E. 2009, MNRAS, 392, 1008

Davis, D., Bird, C., Mushotzky, R. & Odewahn, S.,1995, ApJ 440, 48

Einasto, M., Einasto, J., Tago, E., Müller, V. & Andernach, H. 2001, AJ 122, 2222

Ensslin, T. A., Biermann, P. L., Klein, U. & Kohle, S., 1998, A&A 332, 395

de Bruyn, A. G., & Brentjens, M. A. 2005, A&A, 441, 931

Delain, K. M., & Rudnick, L. 2006, Astronomische Nachrichten, 327, 561

De Young, D. S. 1984, PhysRep, 111, 373

Drury, L. 1983, Space Science Reviews, 36, 57

Eckert, D., Produit, N., Neronov, A., & et al. 2008, International Cosmic Ray Conference, 3, 869

Enßlin, T. A., & Gopal-Krishna 2001, A&A, 366, 26

Feretti, L. 2003, ArXiv Astrophysics e-prints, arXiv:astro-ph/0301576

Feretti, L. 2006, ArXiv Astrophysics e-prints, arXiv:astro-ph/0612185

Fanaroff, B. L. & Riley, J. M 1974, MNRAS 167, 31P

Feretti, L., & Giovannini, G. 1998, Untangling Coma Berenices: A New Vision of an Old Cluster, 123

Feretti, L., Orrù, E., Brunetti, G., Giovannini, G., Kassim, N., & Setti, G. 2004, A&A, 423, 111

Feretti, L. & Newmann, D. M., 2006, A&A 450, 21

Finkbeiner, D. 2003, ApJS 146, 407

Gal, R. R., de Carvalho, R. R., Lopes, P. A. A., Djorgovski, S. G., Brunner, R. J., Mahabal, A., & Odewahn, S. C. 2003, AJ, 125, 2064

Giovannini, G., Feretti, L., Venturi, T., Kim, K.-T., & Kronberg, P. P. 1993, ApJ, 406, 399

Giovannini, G., & Feretti, L. 2004, Journal of Korean Astronomical Society, 37, 323

Govoni, F., Enßlin, T. A., Feretti, L., & Giovannini, G. 2001, A&A, 369, 441

Giovannini, G., Kim, K. T., Kronberg, P. P., & Venturi, T. 1990, Galactic and Intergalactic Magnetic Fields, 140, 492

Giovannini, G., & Feretti, L. 2000, New Astronomy, 5, 335

Giovannini, G., Tordi, M., & Feretti, L. 1999, New Astronomy, 4, 141

Gomez, P. L., Pinkney, J., Burns, J. O., Wang, Q., Owen, F. N., & Voges, W. 1997, ApJ, 474, 580

Govoni, F., Feretti, L., Giovannini, G., Böhringer, H., Reiprich, T. H., & Murgia, M. 2001, A&A, 376, 803

Govoni, F., Murgia, M., Feretti, L., Giovannini, G., Dallacasa, D., & Taylor, G. B. 2005, A&A, 430, L5

Gaensler, B. M., Dickey, J. M., McClure-Griffiths, N. M., Green, A.J., Wieringa, M. H. & Hanyes, R. F., 2001, ApJ 549, 959

Gaensler, B. M., Dickey, J. M., McClure-Griffiths, N. M., Bizunok, N. S. & Green, A. J. 2002, in "Astrophysical Polarized Backgrounds," ed. S. Cecchini, S. Cortiglioni, R. Sault & C. Sbarra, AIP Conference Proceedings v. 609, 20

Gelfand, J. D., Lazio, T. J. W. & Gaensler, B. M., 2004, in "X-Ray and Radio Connections", www.aoc.nrao.edu/events/xradio

Giovannini, G., Feretti, L. & Stanghellini, C., 1991, A&A 252, 528

Gold, B., et al., 2008, arXiv0803.0715G

Hansen, F. K., Branchini, E., Mazzotta, P., Cabella, P., & Dolag, K. 2005, MNRAS, 361, 753

Hernández-Monteagudo, C., Genova-Santos, R., & Atrio-Barandela, F. 2004, ApJL, 613, L89

Hartley, W. G., Gazzola, L., Pearce, F. R., Kay, S. T., & Thomas, P. A. 2008, MNRAS, 386, 2015

Hoeft, M., Brüggen, M., & Yepes, G. 2004, MNRAS, 347, 389

Haffner, L. M., Reynolds, R. J., Tufte, S. L., Madsen, G. J., Jaehnig, K. P. & Percival, J. W., 2003, ApJS 149, 405

Hanisch, R. J., Strom, R. G., & Jaffe, W. J. 1985, A&A 153, 9

Haslam, C. G. T, Salter, C. J., Stoffel, H. & Wilson, W. E., 1999, A&AS 138, 31

Hobbs, G., et al., 2004, MNRAS 352, 1439

Huchra, J. et al., 2005, in Large Scale Structure and the Zone of Avoidance, eds. A. Fairall & P. Woudt, ASP Conf. Proc 329, 135

Jaffe, W. J. & Rudnick, L., 1979, ApJ 233, 453

Jones, T. J., Rudnick, L., DeLaney, T. & Bowden, J., 2003, ApJ 587, 227

Kang, H., Ryu, D., Cen R. & Song, R., 2005, ApJ 620, 21

Katgert, P. et al., 1996, A&A 310, 8

Kempner, J. C., & Sarazin, C. L. 2001, ApJ, 548, 639

Keshet, U., Waxman, E., & Loeb, A. 2004, ApJ, 617, 281

Kim, K.-T., Kronberg, P. P., Giovannini, G., & Venturi, T. 1989, Nature, 341, 720

Kronberg, P. P., Burbidge, E. M., Smith, H. E., & Strom, R. G. 1977, ApJ, 218, 8

Kronberg, P. P., Kothes, R., Salter, C. J., & Perillat, P. 2007, ApJ, 659, 267

Keating, B. G., Timbie, P. T., Polnarev, A., & Steinberger, J. 1998, ApJ, 495, 580

Kempner, J., Blanton, E., Clarke, T., Enß lin, T., Johnston-Hollitt, M. & Rudnick, L. 2004, in Proceedings of The Riddle of Cooling Flows in Galaxies and Clusters of Galaxies, eds. T. Reiprich, J. Kempner, N. Soker, http://www.astro.virginia.edu/coolflow

Keshet, U., Waxman, E., & Loeb, A. 2004, ApJ, 617, 281

Klein, U. & Wielebinski, R. 1979, A&A 72, 229

Kormossa, S. & Böhringer, H., 1999, A&A 344, 755

Kundu, M. R. 1970, ApJ 162, 17

Ledlow, M. J., Voges, W., Owen, F. N., & Burns, J. O. 2003, AJ, 126, 2740

Loken, C., Roettiger, K., Burns, J. O., & Norman, M. 1995, ApJ, 445, 80

Lutovinov, A. A., Vikhlinin, A., Churazov, E. M., Revnivtsev, M. G., & Sunyaev, R. A. 2008, ApJ, 687, 968

Machalski, J., Jamrozy, M., & Zola, S. 2001, A&A, 371, 445

Markevitch, M., Govoni, F., Brunetti, G., & Jerius, D. 2005, ApJ, 627, 733

Merchán, M. E., & Zandivarez, A. 2005, ApJ, 630, 759

Micono, M., Zurlo, N., Massaglia, S., Ferrari, A., & Melrose, D. B. 1999, A&A, 349, 323

Miller, C. J., et al. 2005, AJ, 130, 968

McCarthy, P. J. 1988, Ph.D. Thesis, University of California, Berkeley

Marvel, K., Shukla, H. & Rhee, G. 1999, ApJS 120, 147

Million, E. T., & Allen, S. W. 2008, arXiv:0811.0834

Miller, N. A., Ledlow, M. J., Owen, F. N. & Hill, J. M., 2002, AJ 123, 3018

Milne, D. K., & Dickel, J. R., 1975, AuJPh 28, 209

Miniati, F., Jones, T. W. J., Kang, H. & Ryu, D., 2001, ApJ 562, 233

Miniati, F., 2004, JKAS 37, 465

Moss, C. & Dickens, R. J. 1977, MNRAS 178, 701

Nielbock, M., Chini, R., Jütte, M. & Manthey, E., 2001, A&A 377, 273

Owen, F. N., & Rudnick, L., 1976, ApJ 205, 1

Oxley P. et al., 2004, Proc. SPIE Int. Soc. Opt. Eng., 5543, 320

Page, L., et al. 2007, ApJS, 170, 335

Parma, P., Murgia, M., de Ruiter, H. R., Fanti, R., Mack, K.-H., & Govoni, F. 2007, A&A, 470, 875

Pinkney, J. 1993, BAAS, 25, 1437

Pinkney, J., Burns, J. O., Ledlow, M. J., Gómez, P. L., & Hill, J. M. 2000, AJ, 120, 2269

Pfrommer, C., Springel, V., Enßlin, T. A., & Jubelgas, M. 2006, MNRAS, 367, 113

Pfrommer, C., Enßlin, T. A., & Springel, V. 2008, MNRAS, 385, 1211

Popesso, P., Böhringer, H., Brinkmann, J., Voges, W., & York, D. G. 2004, A&A, 423, 449

Pellegrini, E. W. , Baldwin, J. A., Brogan, C. L., Hanson, M. M., Abel, N. P., Ferland, G.J., Nemala, H. B., Shaw, G. & Troland, T. H., 2007, ApJ 658, 1119.

Pfrommer, C., Springel, V. Ensslin, T. A. & Jebelgas, M., 2006,, MNRAS 367, 113

Pinneault, S., Landecker, T. L., Swerdlyk, C. M. & Reich, W., 1997, A&A 324, 1152

Rauch, M., et al. 1997, ApJ, 489, 7

Rudnick, L. 2002, PASP, 114, 427

Rudnick, L., & Lemmerman, J. 2009, arXiv:0903.0335

Ryu, D., Kang, H., Cho, J., & Das, S. 2008, Science, 320, 909

Reich, W. 2006, ArXiv Astrophysics e-prints, arXiv:astro-ph/0603465

Roettiger, K., Burns, J. O., & Loken, C. 1996, ApJ, 473, 651

Rudnick, L., Delain, K. & Lemmerman, J., 2006, AN 327, 549

Rudnick, L., & Lemmerman, J., 2008, submitted to ApJ

Ryu, D., Kang, H., Hallman, E., & Jones, T. W. 2003, ApJ, 593, 599

Reich, P. & Reich, W. , 1986, A&AS 63, 205

Reich, W. 1982, A&AS, 48, 219

Reich, P., & Reich, W. 1986, A&AS, 63, 205

Rudnick, L. Jones, T. W., Fiedler, R. L., Aller, H. D., Aller, M. F., Hodge, P. E., Owen, F. N., Bignell, R. C. & Puschell, J. J., 1985, ApJS 57, 693

Rudnick, L., 2002, PASP 114, 427

Rudnick, L., 2004, JKAS 37, 329

Sadler, E. M., et al. 2007, MNRAS, 381, 211

Sarazin, C. L. 1999, ApJ, 520, 529

Schaye, J. 2001, ApJL, 562, L95

Schuecker, P., Finoguenov, A., Miniati, F., Böhringer, H., & Briel, U. G. 2004, A&A, 426, 387

Skillman, S. W., O'Shea, B. W., Hallman, E. J., Burns, J. O., & Norman, M. L. 2008, ApJ, 689, 1063

Skrutskie, M. F., et al. 2006, AJ, 131, 1163

Schmidt, S. J., Connolly, A. J., & Hopkins, A. M. 2006, ApJ, 649, 63

Slee, O. B., Roy, A. L., Murgia, M., Andernach, H., & Ehle, M. 2001, AJ, 122, 1172

Stoughton, C., et al. 2002, AJ, 123, 485

Schnitzeler, D. H. F., Katgert, P. & de Bruyn, A. G.,2007, A&A 47, L21

Simmons, J. F. L. & Stewart. B. G. 1985, AA 142, 100

Spoelstra, T. A. Th. 1972, A&A 21, 61

Stil, J. M et al. 2006, AJ 132, 1158

Stil, J. M & Taylor, A. R., 2007, ApJ 663, L 21

Stull, M. A., Price, K, M., Daddario, L. R., Wernecke, S. J., Graf, W. & Grebenkemper, C. J. 1975, AJ 80, 559

Sun X. H., et al. 2007, A&A, 469, 1003S

Takei, Y., et al. 2008, ApJ, 680, 1049

Taylor, A. R. et al., 2003, AJ 125, 3145 (Canadian Galactic Plane Survey)

Tegmark, M. , Eisenstein, D., Hu, W., de Oliveira-Coasta, A. 2000, ApJ 530, 133

http://www.xray.mpe.mpg.de/cgi-bin/rosat/rosat-survey

Vazza, F., Brunetti, G., & Gheller, C. 2009, MNRAS, 459

Venturi, T., Giacintucci, S., Dallacasa, D., Cassano, R., Brunetti, G., Bardelli, S., & Setti, G. 2008, A&A, 484, 327

Venturi, T., et al. 2009, arXiv:0903.2934

Wardle, J. F. C., 1971, ApL 8, 183

Wardle, J. F. C. & Kronberg, P. P, 1974, ApJ 194, 249

Wieringa, M. H., de Bruyn, A. G., Jansen, D., Brouw, W. N. & Katgert, P., 1993, A&A 268, 215

West, J. L., English, Y., Normandeau, M. & Landecker, T. L., 2007, ApJ 656, 914

Wik, D. R., Sarazin, C. L., Finoguenov, A., Matsushita, K., Nakazawa, K., & Clarke, T. E. 2009, arXiv:0902.3658

Wilson, T. L., Hanson, M. M. & Muders, D., 2003, ApJ 590, 895

Wolleben, M. & Reich, W., 2004, a&A 427, 537

Wolleben, M., Landecker, T. L., Reich, W. & Wielebinski, R., 2006, A&A, 448, 411.

Wolleben, M., 2007, ApJ 664, 349

York, D. G., et al. 2000, AJ, 120, 1579